



HAL
open science

Metal-sulfide materials for ethane conversion in presence of CO₂

Vera Bikbaeva

► **To cite this version:**

Vera Bikbaeva. Metal-sulfide materials for ethane conversion in presence of CO₂. Organic chemistry. Normandie Université, 2022. English. NNT : 2022NORMC250 . tel-04348743

HAL Id: tel-04348743

<https://theses.hal.science/tel-04348743>

Submitted on 17 Dec 2023

HAL is a multi-disciplinary open access archive for the deposit and dissemination of scientific research documents, whether they are published or not. The documents may come from teaching and research institutions in France or abroad, or from public or private research centers.

L'archive ouverte pluridisciplinaire **HAL**, est destinée au dépôt et à la diffusion de documents scientifiques de niveau recherche, publiés ou non, émanant des établissements d'enseignement et de recherche français ou étrangers, des laboratoires publics ou privés.



Normandie Université

THÈSE

Pour obtenir le diplôme de doctorat

Spécialité CHIMIE

Préparée au sein de l'Université de Caen Normandie

Metal-sulfide materials for ethane conversion in presence of CO₂

Présentée et soutenue par
VERA BIKBAEVA

Thèse soutenue le 16/12/2022
devant le jury composé de

MME CATHERINE BATIOU-DUPEYRAT	Directeur de recherche, UNIVERSITE POITIERS	Rapporteur du jury
M. BENOIT LOUIS	Directeur de recherche au CNRS, UNIVERSITE STRASBOURG	Rapporteur du jury
M. NIKOLAY NESTERENKO	Ingénieur HDR, Sulzer	Membre du jury
MME TZONKA MINEVA	Directeur de recherche, ENSCM Montpellier	Président du jury
M. VALENTIN VALTCHEV	Directeur de recherche au CNRS, ENSICAEN	Directeur de thèse

Thèse dirigée par VALENTIN VALTCHEV (Laboratoire catalyse et spectrochimie (Caen))



UNIVERSITÉ
CAEN
NORMANDIE



Content

Chapter 1. Introduction	5
1. General introduction	6
2. Scopes of the thesis	7
Chapter 2. Literature review	9
1. Introduction.....	10
1.1. Decarbonization challenges and ethane processing	10
1.2. The thermodynamic aspect of the interactions C ₂ H ₆ - CO ₂ interactions	10
1.3. State-of-the-art steam cracking of ethane, ethane oxidative dehydrogenation, and dry ethane reforming.....	13
1.4. Metal carbides and metal sulfides application for CH ₄ , C ₂ H ₆ , and CO ₂ conversion	16
1.5. Properties and interphases transformations of MoO ₂ , MoO ₃ , MoS ₂ , and Mo ₂ C.....	19
1.5.1. Oxidic phases: MoO ₂ and MoO ₃	20
1.5.2. Sulfidic MoS ₂ phase.....	21
1.5.3. Carbide phases.....	22
1.5.4. Mo oxycarbides	24
1.5.5. Phases transformation.....	25
1.5.5.1. Phase transformation during sulfidic catalyst precursors formation	25
1.5.5.2. Potential <i>in situ</i> catalyst phases transformation under test conditions	25
2. Catalyst support	29
2.1. Embryonic zeolite and its properties.....	29
2.2. Application of embryonic zeolites as catalyst carriers	31
3. Crystalline thiogallates for ODH-CO ₂	31
References.....	35
Chapter 3. Materials and methods	45
Part 1. Materials	46
1. Embryonic zeolites	46
1.2 Preparation of EZ carriers	46
1.3 Metal loading and sulfidation.....	46
1.3.1 Wetness impregnation (WI).....	46
1.3.2 Hydrothermal treatment (HT)	47
1.3.4 Sulfurizing	47
2. Thiogallates synthesis.....	48
3. Characterization	48
3.1. Physicochemical characterization	48
3.1.1. X-Ray Diffraction	48
3.1.2. Raman spectroscopy.....	50

3.1.3. Fourier transformed infrared spectroscopy	51
3.1.4. N ₂ adsorption-desorption	52
3.1.5. Scanning Electron Microscopy	53
3.1.6. Energy Dispersive X-ray Spectroscopy	53
3.1.7. Thermogravimetry	54
3.1.8 Ultraviolet-visible spectroscopy	55
3.1.9 Solid-state nuclear magnetic resonance.....	56
3.1.10 Inductively coupled plasma atomic emission spectroscopy.....	57
3.2 Catalytic test	57
3.2.1 Oxidative ethane dehydrogenation and dry reforming of ethane (DRE)	57
3.2.2 Techno-economical analysis	59
3.2.3 Reverse water gas shift reaction	60
Conclusions.....	60
References.....	62
Chapter 4. A Low Carbon Route to Ethylene: Ethane Oxidative Dehydrogenation with CO₂ on Embryonic Zeolite Supported Mo-Carbide Catalyst.....	65
1. Introduction.....	66
2. Results and discussion.....	70
2.1. Characterization of the catalysts	70
2.2. Catalytic performances.....	73
2.2.1. Impact of Mo-precursor:MoO _x vs MoS ₂	75
2.2.2. Impact of the catalyst carrier.....	77
2.2.3. Performance of Al-free EZ _{Si} -5%(Mo ₂ C) _S in ODH-CO ₂ of ethane	79
2.3. Techno-economical analysis of the ODH-CO ₂ process based on an EZ _{Si} -5%(Mo ₂ C) _S catalyst	80
Conclusions.....	86
References.....	87
Chapter 5. Optimization of the Mo₂C-based catalytic systems for co-processing of ethane with CO₂	93
1. Introduction.....	94
2. Results and discussion.....	96
2.2 Optimization of monometallic Mo ₂ C-based catalysts.....	96
2.2.1. Mo-species on the monometallic catalyst.....	96
2.2.2. Characterization by X-Ray diffraction of Mo-carbide phases produced from different precursors	100
2.2.3. Optimization of the activity of Mo ₂ C-based samples in co-processing of CO ₂ and ethane by different pretreatment	101
2.2.4. Conclusion for the monometallic Mo ₂ C-based catalyst characterization and tuning104	

2.3 Cobalt-doped molybdenum catalysts.....	104
2.3.1. Characterization of the catalysts	104
2.3.2. Role of the cobalt doping.....	106
2.3.3. WHSV impact on catalyst performance.....	108
2.3.4. Impact of reaction temperature	112
2.3.5. Impact of cobalt content on the catalyst.....	114
2.3.6. Impact of the heating rate on the catalyst performances and tests reproducibility	115
2.3.7. Oxidic vs. sulfidic bimetallic precursors.....	116
3. Study of the spent catalysts	118
3.1. XRD study.....	118
3.1.1. Sulfide-derived catalysts.....	118
3.1.2. Oxide-derived catalysts.....	121
3.2. Raman characterization	122
3.3. Thermogravimetric characterization	122
4. Conclusions.....	125
References.....	128
Chapter 6. Ethane Oxidative Dehydrogenation with CO₂ on thiogallates	131
1. Introduction.....	132
2. Results and discussion.....	134
2.1. Synthesis and characterization of the catalysts	134
2.2. Synthesis optimization.....	138
2.3. Catalytic performances.....	140
2.3.1. KGaS ₂ thermal stability.....	140
2.3.2. Performance in ODH-CO ₂ of ethane	143
3. Conclusions.....	147
References.....	149
Chapter 7. Conclusions and prospects	153
1. Conclusions.....	154
2. Prospects	155
Scientific production	157
Acknowledgments.....	158

Chapter 1. Introduction

1. General introduction

With new environmental and industrial standards, the processing of light alkanes into valuable chemicals is undergoing major changes. This research is focused on alternatives to ethane steam cracking. The process efficiency is around 95%, nevertheless, it now possesses principal challenges for modernization and major approaches modification.

Minimizing the number of principal heavy products for the ethylene or propylene-directed scheme is one of the tasks. In industry, the cracking process is considered in total with subsequent product separation and fractionation. Decreasing the number of produced fractions is a major requirement in the quest for alternative processes. Reducing the associated greenhouse gas emissions is dictated by environmental requirements, leading to a preference advanced CO₂-neutral or negative scheme. Furthermore, cracking is one of the most endothermic industrial processes. Therefore, significant temperature reduction for alternative technologies would be an advantage. These considerations led to the revision of the potential of oxidative ethane dehydrogenation (ODH) for ethylene production.

Choosing between O₂ and CO₂ as an oxidant for ODH, application of the last one tends to the appearance of a smaller number of the side products. However, oxidative ethane dehydrogenation with CO₂ (ODH-CO₂) requires a higher temperature than the O₂-based scheme. The last disadvantage is overcovered by CO₂ utilization.

The main goal of this Ph.D. thesis was to design the ODH-CO₂ catalyst with high hydrogenation function and improved stability to CO₂ oxidation and coke deactivation. For this purpose, sulfide-based materials were selected. They demonstrated high hydrogenation potential, coke formation prevention, tunable acidity, and high selectivity to the key products in close processes. The first principal task was to evaluate the prospects of sulfide materials for operation in the temperature range of 700 °C and above. Two fundamentally different types of catalysts were chosen: supported MoS₂ on embryonic zeolite and ternary alkali thiogallates. The focus was on the catalysts' stability, intensification of the CO₂ conversion, and tuning ethylene selectivity.

The experiment was designed for application under harsh conditions and a non-optimal input flow ratio. This approach makes it possible to determine the coke-resistant of the catalysts.

Furthermore, in pursuit of the goal of the potential application of the impure ethane fraction with or the ability to change the ratio of $\text{CO}_2/\text{C}_2\text{H}_6$ input flows, saving the ODH- CO_2 mechanism.

The second catalyst, KGaS_2 thiogallate, was used for the first time in this reaction. Previously, the possibilities of using KGaS_2 in high-temperature catalytic processes were completely unexplored. This part of the study includes not only catalysts's evaluation but also the development of synthetic methodology, which leads to relatively small KGaS_2 crystallites.

Scopes of the thesis

This study applied two principally novel approaches to prepare catalysts for oxidative ethane dehydrogenation (ODH) for ethylene production. The thesis is divided into the following sections:

Chapter 2 presents a literature overview of the process and the selected catalysts with a critical analysis of their properties.

In **Chapter 3**, the synthesis protocols and main characterization techniques are presented. For materials supported on embryonic zeolite, the main accent is put on the characterization taking into account the difficulties related to their amorphous nature. Several possible verified approaches for active phase preparation are discussed in detail. The sol-gel synthesis protocol used for the synthesis of KGaS_2 is also presented.

Chapter 4 illustrates the catalytic potential of the sulfide-derived materials. This chapter presents the catalytic results and provides details on the activity of molybdenum sulfide-derived samples. This chapter has been approved for publication in Applied Catalysis B: Environmental (doi.org/10.1016/j.apcatb.2022.122011).

Chapter 5 reports on the performance of $\text{MoS}_2\text{-CoS}_x$ catalysts. This study provides valuable information on the sulfide to carbide conversion under the ethane treatment. The Co additive's effect that completely changed the mechanism of the reaction and the product composition is discussed. The conditions for conducting a controlled transition between ODH- CO_2 and dry reforming of ethane (DRE) are presented.

Chapter 6 deals with the catalytic performance of the thiogallate catalyst. The sol-gel synthesis approach employed to synthesis the thiogallates is also presented. This chapter has been approved for publication in *Inorganic Chemistry Frontiers* (doi:10.1039/D2QI01630C).

The thesis also includes a summary of the results (**Chapter 7**), the most important findings and the perspectives.

Chapter 2. Literature review

1. Introduction

1.1. Decarbonization challenges and ethane processing

In 2022 the price for 1 ton of emitted CO₂ is 82-91 euros. If a couple of years ago the mark of 100 euros was predicted by 2030, then the forecast may change significantly this year. The companies are also more likely to rethink their development strategy and integrate new carbon neutral or negative technologies or some CO₂ chemical utilization processes to avoid novel expenses.

Thus, it leads us to a new concept of evaluating the prospects of processes and used methods. Ethylene production from ethane by steam cracking with strong CO₂ emissions has become an old-generation technology. Ethane dehydrogenation in CO₂ presence could be one of the best options for modern large-scale industrial facilities since the ethylene selectivity could be comparable with a commercialized process or higher. However, the obtained C₂H₄ should be involved in the next transformation, as the transportation of C₂H₄ as final products is expensive and risky and requires special technology. ODH-CO₂ is a good alternative for existing steam crackers. In the absence of an ethylene market, a variant with the production of synthesis gas components can be offered. Synthesis gas could be produced via ethane dry reforming (DRE) under similar ODH-CO₂ conditions.

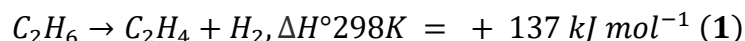
Selective tuning opportunities between ODH-CO₂ and DRE are a novel trend for ethane processing with CO₂. It is also important that both processes can be carried out under similar conditions. Regulation will be carried out either by replacing the catalyst or by some other parameters such as contact time and temperature.

1.2. The thermodynamic aspect of the interactions C₂H₆ - CO₂ interactions

Ethane and CO₂ interactions at high temperatures could be performed in various ways. This subsection is devoted to possible transformations in the selected system.

Ethane direct dehydrogenation (DDE) is the endothermic process (**reaction 1** [1]). Thermal decomposition becomes economically attractive at high temperatures, i.e., over 800 °C. However, the non-catalytic process shows low energy efficiency. This reaction is accompanied by deeper

cracking products formation. The ethane decomposition by cracking pathway is easily detected by the presence of C3+ fractions and aromatics.



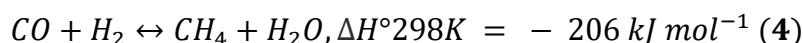
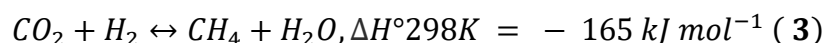
Presented in the system CO₂ could interact with produced by DDE H₂. It resolves to synthesis gas formation is a reverse water-gas shift reaction (RWGS, **reaction 2**):



The combination of parallel DDE and RWGS describes a two-step ODH-CO₂ mechanism. RWGS is an endothermic process that is favored at high temperatures. The activation temperature is a function of the CO₂:H₂ ratio. Thus, by rising CO₂ concentration, the consumption of H₂ is forced, or excess of H₂ (CO₂:H₂=1:3 or 1:4) leads to CO₂ consumption. For the mixture CO₂:H₂=1:1 or 1:2, noticeable CO₂ conversion starts at about 450-500 °C. The formation of CH₄ is one of the most typical co-process. Methane presence in the system leads to a change in the thermodynamic's equilibrium. **Fig. 1** represents the modeled equilibrium mole fraction in the temperature range of 200-800 °C [3].

Compared to some methanation or reforming reactions for RWGS, the short contact time is preferable. The CH₄/CO ratio could be changed, at 700°C+ carbon monoxide become the major product. It is demonstrated in **Fig.1**, that the equilibrium methane (blue) curve decreased with the temperature rising. With increasing H₂ in the mixture, the equilibrium temperature for H₂-CO is shifted to the right, but still less than 650 °C. The use of a catalyst could prevent methanation overall.

For CO₂-H₂-CO-H₂O mix, several additional transformation routes are possible. CO₂ and formed CO could interact with H₂ via exothermic methanation (**reactions 3-4**):



A positive moment is that CO₂ methanation (Sabatier reaction) is generally applied to other conditions: 300-400 °C and pressure of about 3MPa. CO methanation is also preferable at temperatures not higher than 400 °C. Thus, the probability of these side processes is significantly reduced.

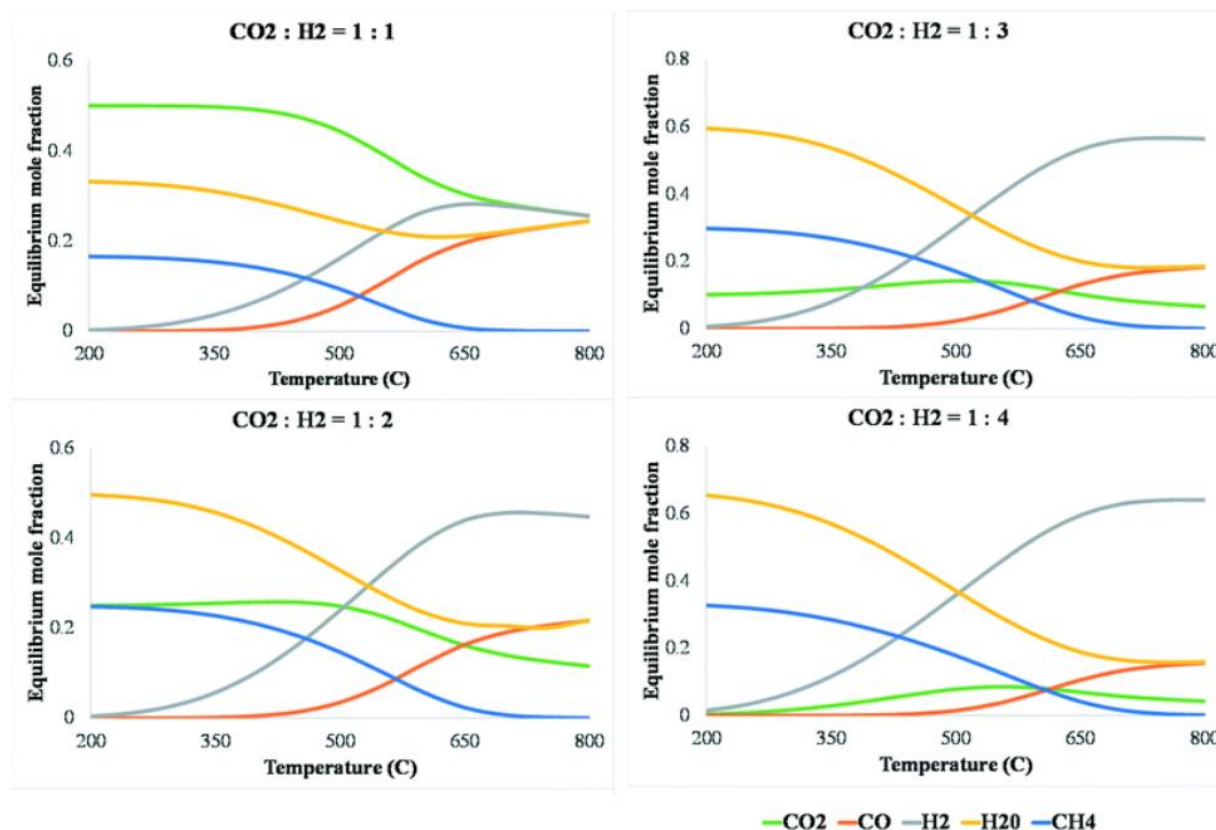
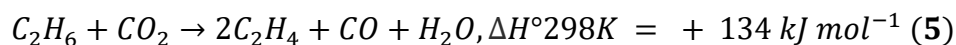


Fig. 1- Temperature influence on the thermodynamic equilibrium of the RWGS reaction (1 bar). Aspen Plus simulations were performed using an RGibbs reactor and the Peng–Robinson property method. Reproduced from [3].

If back to the main process of this thesis (ODH-CO₂) performed in one step, at 298 K this reaction is endothermic (**reaction 5** [1]):



Possible products for this system are CO, H₂, C₂H₄, and water (**Fig.2**). At the temperature of around 550 °C (823K), oxidative ethane dehydrogenation with CO₂ ($C_2H_6 + CO_2 \rightarrow 2C_2H_4 + CO + H_2O$) and ethane dry reforming ($C_2H_6 + 2CO_2 \rightarrow 4CO + 3H_2$) occurs simultaneously. The ratio DRE/ODH-CO₂ grows with temperature.

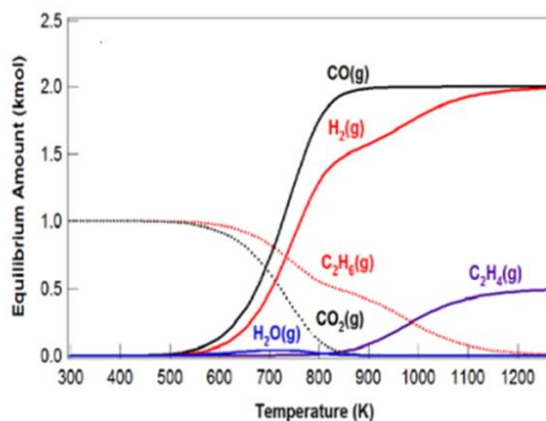


Fig.2- Thermodynamic equilibrium for $\text{CO}_2 + \text{C}_2\text{H}_6$ reaction (1 atm, 373 – 1273 K and inlet feed ratios of $\text{CO}_2 : \text{C}_2\text{H}_6 = 1$). Reproduced from [1].

Ethane dry reforming (DRE) (**reaction 6** [4]) is similar to well-studied dry methane reforming (DRM). DRE is more thermodynamically favorable than DRM, it reaches $\Delta G < 0$ at the 100 K lower[1].



1.3. State-of-the-art steam cracking of ethane, ethane oxidative dehydrogenation, and dry ethane reforming

Oxidative ethane dehydrogenation gained popularity as the alternative to steam cracking of ethane. Steam crackers (SC) with ethane feed possess the highest possible ethylene yield. According to the published data it reaches 80% [5]. It is well-matured technology, but the new ecological requirements for production, it is becoming more and more difficult for it to maintain its position and increase profits. Cracking to produce ethylene and other fractions is effective on a large scale. One of the main conditions is the direct processing of the resulting ethylene.

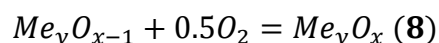
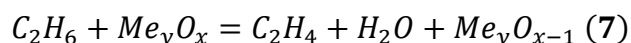
Commercial cracking is performed in fired tubular reactors with 0.1-0.5 s flow contact time. The temperature depends on the feed source and consists of 750-880 °C. Under these conditions, the formation of heavy fractions will always happen as it is a thermal process. Also, about 300 million tons of CO_2 each year is obtained as a co-product of SC [6].

'Greenness' crackers could be achieved in various ways. One of the wide-advertised solutions was the application of electric E-furnaces by BASF. This year the construction of large-

scale (6 megawatts) electrically heated steam cracker furnaces was launched [7]. Thus, the CO₂ emissions from heating could be significantly limited.

Another way to decrease CO₂ pollution from heating is applying the other process at a lower temperature. For instance, the semi-industrial facilities of oxidative ethane dehydrogenation (ODH) are based on Linde/Clariant partnership-EDHOX™[8] and chemical looping CL-ODH [9]. In contrast to the cracking, for EDHOX™ process is carried out at 400 °C. As the catalyst was used MoVTenb oxidic complex [10]. The oxygen was applied as an oxidant. The feedstock could be separated into ethylene and acetic acid derivatives plus CO₂. Carbon dioxide emissions are lower than steam crackers [11]. The produced CO₂ has a high purity and could be involved in the downstream processing.

Oxygen is readily taken from the oxidic catalysts. A chemical looping partial oxidation (CLPO) exists for methane reforming [12]. This approach improves energy efficiency. CL-ODH is supported by a robust redox catalyst and could be adopted for ethane conversion to ethylene (**reactions 7 and 8**).



For CL with ethane MoO₃/Fe₂O₃ [13], and manganese silicate [14] catalytic systems could be applied. The better safety of CL is reached by the use of oxygen from the crystal lattice of catalysts. Additionally, it decreases the process costs as there is no need for gaseous O₂ for the ethylene synthesis step [15]. The used oxidic catalyst is renewed under air or oxygen flow for recovery. The temperature range is similar to steam cracking: 500-850 °C. For instance, ethane conversion on Mg-Mn-O-Na system can reach more than 90% [16], while on Mo-Fe-O one it is only 8% [17]. However, with the rise of conversion, ethylene selectivity dramatically decreased.

One of the most promising alternatives could be an oxidative process using CO₂ instead of oxygen. In this way, carbon dioxide is converted to monoxide. Produced CO could be applied for the following processing of the synthesis gas. In this way, the ejections during the heating of the furnaces can be balanced. With an increase in CO₂ conversion, the process may reach CO₂-negativity.

Ethane oxidative dehydrogenation in the presence of CO₂ (ODH-CO₂) is operated on a higher number of catalysts: oxides, Pt, Pd, or carbides. CO₂ is a mild oxidant in contrast to O₂, and thus the high ethylene selectivity could be reached at high ethane conversion without the formation of any oxygenates.

Ethylene and CO are attractive for process economic products. A standard challenge for ODH-CO₂ is decreasing to extra-low level C₃+ hydrocarbons and aromatics, controlling a coke formation, and preventing the catalyst oxidation.

Possible coke formation can be considered as a source of additional CO via the Boudouard reaction (**reaction 9**).



The temperature range for ODH-CO₂ is close to the CL-ODH process, i.e., 500-800 °C. The process temperature depends on the nature of the active phase. Iron-based catalytic systems operate at a lower temperature, at 575 °C on Fe/NiMgZr ethane conversion is 9% and the CO₂ conversion 13% [18]. At 550-650 °C Cr-based already could partially convert ethane: 5-21% on CrO_x/ZrO₂ [19]. The application of more acidic zeolite support for the active oxidic phase could decrease the operation temperature [20] and improve ethane conversion at the same temperature in contrast with the all-silica (silicalite-1) support [20].

Selectivity for ethane to ethylene can exceed 95-99% [21,22]. However, achieving ethylene selectivity of about 90% with rising ethane conversion could be a challenge. It is also worth noting that it is often possible to influence predominantly only ethane or CO₂. Rarely, the ODH-CO₂ investigation is performed at 700 °C+; one example is presented in reference [23]. Catalytic tests were carried out on CsRu/CeO₂. The authors achieved very positive results in light olefins selectivity 86.7% at 750 °C at around 70% conversion of ethane. However, in this work, the issue of the CO₂ conversion stability during the 93-day test was not disclosed. The mentioned CO₂ conversion was 7 times lower (8-10%). Rahmani et al. presented the investigation of the Cr/ZSM-5-CeO₂ catalyst in ODH-CO₂ at 700°C [24]. Ethylene selectivity was 87% at 70.4% ethane conversion. CO₂ conversion was not reported by the authors.

The ethane steam cracking pathway was mentioned in following references. Guo et al. on Co-based catalytic systems performed both ODH-CO₂ and DRE [25]. Catalysts activity was tuned

via the cobalt state in the catalyst. Over ion-exchanged (Co-IE) samples, ethylene selectivity reached 94-97%; thus, the preferable pathway was ODH. Over impregnated samples (Co-IM), ethane and CO₂ interacted via DRE. The ethane conversion on Co-IM was 3 times higher than on Co-IE (88-75%). Pd and Pt-based bimetallic catalysts could be operated for both processes [26]. For promoting C-H fission for ODH pathway 1%PtIn₃/CeO₂ was applied. It was performed ethane conversion with stable ethylene selectivity of around 90%. 1%PdCo_{0.3}, 1%PdCo₁, and 1%PdCo₃ were preferable for C-C bond scission and DRE pathway. CO selectivity reached about 90%. Ni_xFe_y/CeO₂ systems could promote ODH-CO₂ and DRE [27]. On Ni₁Fe₃/CeO₂ ethylene selectivity was about 70%, and on Ni₃Fe₁/CeO₂ CO selectivity hit 97% at 600 °C.

1.4. Metal carbides and metal sulfides application for CH₄, C₂H₆, and CO₂ conversion

Mo carbide materials have already been reported as catalysts for ethane and carbon dioxide processing. Mo sulfide materials still have not been reported for ethane processing, however, known for CO₂ conversion. Methane processing is wider represented on Mo₂C-based catalysts than ethane processing, for example via dry reforming [28]. MoS₂ was already investigated for methane processing [29]. The identified features can be applied to ethane oxidative conversion tuning over carbides.

Carbides

Since Boudart [30] and Sinffelt [31] had announced for molybdenum and tungsten carbides that they show a noble metal-like activity in isomerization and hydrogenolysis reaction, a lot of research was focused on the use of carbide catalysts. Particularly, the metal carbide phase became widely-used for dry methane reforming (DRM) catalyst design [32,33]. Both CO₂ and CH₄ are highly stable molecules. Their conjoint valorization is an endothermic process, for instance, $\Delta H_{298} = +248 \text{ kJ}\cdot\text{mol}^{-1}$ [34]. Application of Mo₂C for DRM is presented in [35,36], WC in [37].

Mo carbide catalysts demonstrated promising coke or sulfur poisoning resistance. However, after several decades of intense research, the catalysts' stability remained a stumbling block. At temperatures 700 °C+, Mo₂C via interaction with CO₂, oxidizes to MoO₂ due to its high oxophilicity during reforming. Partially, it could be minimized by application-supported carbides or by doping. Decreasing catalyst oxidation could be mitigated by a process performed under

pressure (2-10 bar). The alternative solution to the described problem is resulted in a new process, operated at lower temperature DRE.

Dry methane reforming on Mo₂C catalysts could be performed as a thermal or plasma process: non-thermal plasma reforming over Mo₂C-Ni/Al₂O₃ [38], thermal DRE on α- and β-Mo₂C [28].

The discussion of dry ethane reforming usually proceeds in the context of catalyst design for ethane oxidative dehydrogenation. Very few works reported a more detailed study of reforming over Mo₂C-based catalytic systems. However, these catalysts have become more and more popular in the last few years for ODH-CO₂. The energy profile for ODH-CO₂ on Mo₂C was simulated and published by Porosoff et al. [39]. The formation of CH₃CH₂* is more energy preferable than CH₃CH₂O*; thus, the ethylene formation is more expectable than some oxygenates. Additionally, these calculations were confirmed by catalytic tests.

Despite the quantum chemical confirmation of a higher probability of the reaction proceeding according to the mechanism of oxidative ethane reduction in CO₂ presence, in practice, it is noted some variations of combination reforming and oxidative dehydrogenation.

Ethylene selectivity tailoring is reached by a combination of running conditions and the catalytic system composition. The first article that confirmed the combination of ODH-CO₂ and DRE appeared in 1999, the Solymosi and Nemeth studied Mo₂C/SiO₂ and bulk Mo₂C catalysts for ethane dehydrogenation [40]. Thus, carbide applicability has been extended to ethane processing. In the temperature range, 577-650 °C, the ODH-CO₂ route prevalence, with temperature growth, the proportion of reforming has increased. At 600 °C, ethane conversion over bulk phase reached 3%, for SiO₂-supported at the same 3%. However, ethylene selectivity improved by 20-30%. The selectivity of methane in the product mixture remained moderate at about 20%. In higher dilution conditions and 690 °C, ethane conversion was 55%. Ethylene selectivity decreased to 73%. As already discussed, selectivity values were represented for forming the products from ethane. Based on the calculations on all C-contained products, the C₂H₄/CO ratio dramatically dropped from 0.9 to 0.3 with temperature growth in the 530-690 °C interval. These results suggest that the DRE is preferable.

Studies on bulk Mo_2C and $\gamma\text{-Al}_2\text{O}_3$ and CeO_2 at $600\text{ }^\circ\text{C}$ [39] demonstrated how the nature of support could change the $\text{C}_2\text{H}_4/\text{CO}$ product ratio. At $600\text{ }^\circ\text{C}$, $\text{CO}_2/\text{C}_2\text{H}_6=1/1$ CO_2 conversion reached 1% on non-supported Mo_2C and 1.8 on $\text{Mo}_2\text{C}/\gamma\text{-Al}_2\text{O}_3$. The ratio of ethylene to CO selectivity was 1.1/1-1.5/1. The total methane and C_3+ selectivity was less than 2%. Over $\text{Mo}_2\text{C}/\text{CeO}_2$ CO_2 and C_2H_6 conversion is extremely low, less than 0.5%. The main reaction product was a CO with 88% selectivity. The $\text{C}_2\text{H}_4/\text{CO}$ ratio was 0.11. In turn, this indicates that the combination of Mo_2C and CeO_2 is not suitable for the ODH route. Authors in addition have investigated the catalyst's oxidation stability and the deactivation mechanism. Under ethane and CO_2 flows carbide catalyst oxidized to MoO_2 . It was detected by in-situ XANES deactivation simulation.

Another study of the ODH and DRE carried out on a carbide catalyst was reported [41]. After O- or Fe-modification of $\beta\text{-Mo}_2\text{C}$, ethane oxidative CO_2 -assisted dehydrogenation becomes more favorable than the DRE route. Quite unexpectedly, on a pure carbide catalyst C-C scission (DRE) was dominated. As DFT-calculated energy profiles indicate the ODH- CO_2 (C-H scission) should be the preferable route [39].

Important results of other process suppression over supported Mo_2C are discussed in [42]. In this research, for the samples on Al_2O_3 and ZrO_2 , ethane dehydrogenation (DDE) activity was raised after a specific time on the stream. For $\text{Mo}_2\text{C}/\text{Ga}_2\text{O}_3$, DRE reaction was preferable during all tested periods. The application of $\text{Mo}_2\text{C}/\text{SiO}_2$ prevented the fast catalyst deactivation. For conversion of the stoichiometric $\text{CO}_2/\text{C}_2\text{H}_6$ mixture, the favorable route is ODH- CO_2 , DR, or DRE contributions are insignificant under studied conditions.

The use of Mo_2C supported on silicalite or zeolite makes it possible to improve ethane conversion while maintaining high selectivity to ethylene. Regulation of the contribution of DRE, DR, and ODH- CO_2 as a co-process is usually done through active phase composition modification or tuning WHSV, $\text{CO}_2/\text{C}_2\text{H}_6$ ratio, and temperature.

Sulfides

Metal sulfides are successfully applied as catalysts for CO_2 hydrogenation under pressure. DFT calculations confirm a Mo_6S_8 cluster activity for MeOH synthesis from CO_2 [43]. If MoS_2 could

promote C-O scission and formation $*H_xCO$ intermediates following conversion to CH_4 , Mo_6S_8 clusters are more appropriate for CO formation and its hydrogenation to methanol via $*HCO$ intermediate. Practically, MoS_2/C [44] demonstrated selective methanol formation (67-96%) with 27% CO_2 conversion at 160 °C, 3MPa. The fundamental investigation of the mechanism for MoS_2 in CO_2 hydrogenation to CH_3OH resulted in the creation of a durable catalyst able to run a 3000 h catalytic test without deactivation at 5-6 MPa in the temperature range 25-280 °C [45]. At the same time, the main product from carbon dioxide will not be methanol at lower pressure and higher temperature. MoS_2 could be an interesting catalyst for CO_2 conversion to methane [46]. At 300-500 °C and 1 MPa over MoS_2/G , methane selectivity was about 95-100%.

MoS_2 and WS_2 were studied in dry methane reforming at 600 °C. In contrast to the model, Ni/SiO_2 catalyst CH_4 conversion on sulfides was lower and observed at the level of 7-8%, but it differed in noticeable stability [29]. Mo oxide-based samples were utilized for dry methane reforming performed in the presence of 50 ppm of H_2S vapors. It can be assumed that under the employed test conditions, *in situ* sulfurizing occurred. H_2S additives led to a reduction of the coke formation [47]. However, the use of sulfides as reforming catalysts has not been studied deeply and has been reflected in several publications.

For ethane conversion, sulfides' application is announced for non-oxidative dehydrogenation. The bifunctional ZSM-5-ZnS catalyst, in contrast to the Zn-containing ZSM-5 catalyst, performed a stable ethane conversion. Sulfur addition allows improvement of the durability and coke resistance [48]. , To the best of my knowledge, there is not a publication reporting the use of MoS_2 or other sulfides in oxidative ethane dehydrogenation.

1.5. Properties and interphases transformations of MoO_2 , MoO_3 , MoS_2 , and Mo_2C

The analysis of DRM, DRE, ODH- CO_2 reactions indicates a possibility of catalysts' active phase composition transformation under high temperature or high pressure. This may lead to deactivation or the formation of a new active phase. More information is needed to anticipate the catalysts' behavior, but the understanding of MoS_2 , MoO_3 , and Mo_2C possible transformations under $C_2H_6-CO_2$ flow, is a challenge. The MoS_2 conversion to Mo_2C under CH_4 flow at 750-850 °C

is already reported [49,50]. This change leads to a significant deterioration in conversion or selectivity.

In the first part of the following section, a brief description of each phase and its possible application is provided. In the second part, the interfacial transitions are considered in more detail.

1.5.1. Oxidic phases: MoO_2 and MoO_3

MoO₂

MoO_2 is a dark brown-violet metal dioxide. It is crystals with monoclinic symmetry and $P2_1/c$ space group [51] (**Fig.4**). Molybdenum dioxide could be applied as the catalyst for light hydrocarbons isomerization [52], and for partial gasoline oxidation [52]. It is also a catalyst for CO_2 gasification of carbon [54] at 500-550 °C. However, there is not information if MoO_2 undergoes structural changes upon the catalytic reaction.

In some research, MoO_2 physical changes were related to catalyst deactivation [32,55]. For instance, the reverse transformation to carbide was presented by A. Kurlov et al. [32]. As the catalyst molybdenum dioxide could be applied for aviation fuel oxidation [56], and benzyl alcohol oxidation to benzaldehyde [57].

MoO₃

MoO_3 is a yellow-green metal trioxide. The $\alpha\text{-MoO}_3$ is the most stable modification, it exhibits an orthorhombic structure with the $Pbnm$ space group (**Fig.3**). This oxide is n-type semiconductor [58]. For the many supported materials, its formation by impregnation or hydrothermal methods may be accompanied by the formation of polymolybdates and monomolybdate species. The type of formed species is a function of pH and some other synthesis parameters. Over SiO_2 and Al_2O_3 support the MoO_3 phase may contain $[\text{Mo}_7\text{O}_{24}]^{6-}$ and isolated $[\text{MoO}_4]^{2-}$ [59].

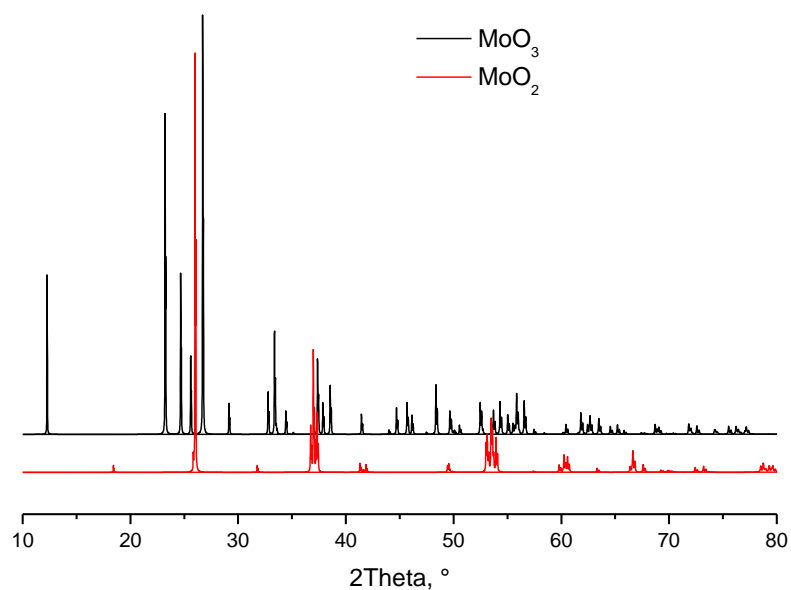


Fig.3- Molybdenum oxides: for MoO_3 simulation the cif of orthorhombic crystal with $Pnma$ space group [60] and for MoO_2 simulation the cif of monoclinic crystal with $P2_1/c$ space group [51] are used, respectively.

MoO_3 supported on Al_2O_3 , TiO_2 , ZrO_2 , and SiO_2 are known catalysts for ODH [61]. Cu-modified MoO_3/FAU in RWGS is presented in [62]. It demonstrated excellent CO selectivity (>99%).

1.5.2. Sulfidic MoS_2 phase

MoS_2 is a well-known transition metal dichalcogenide. It is wide-used for hydrodesulfurization catalyst design and in the optoelectronics industry. It has three phases: 2H- MoS_2 , 3R, and 1T- MoS_2 , with different properties and stability (**Fig. 4**). As the transition metal dichalcogenide, it demonstrated a layered graphite-like structure. The 2H and 3R phases are semiconductors, and 1T phase has paramagnetic and metallic properties.

The 2H is known as a stable phase with hexagonal crystal symmetry. The 2H- MoS_2 crystallized in $P6_3/mmc$ space group [64] (**Fig.5**). The 2H- MoS_2 in contrast 1T- MoS_2 at could exist high temperature (300 °C+) [65]. Thus, it is more attractive for catalytic application.

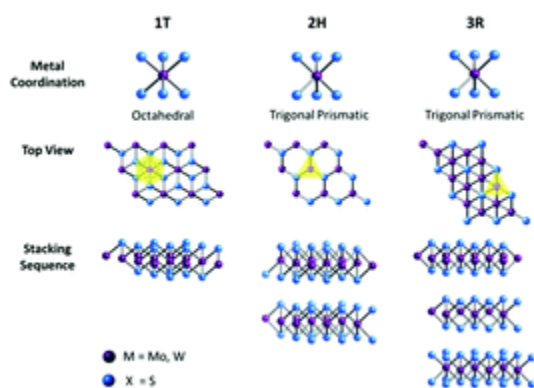


Fig.4- Various MoS₂ phases. Reproduced from [63]

MoS₂ had formed by slabs, each of them has S-edge or M- edge (metallic) states. The number of stacked slabs is an important parameter for material properties control. As 2D crystalline Mo disulfide could exist as nanosheets or nanoribbons, these structures are more stable by thermodynamic calculations. Also, it is presented as 1D as nanowires and nanotubes, as OD as quantum dots.

1.5.3. Carbide phases

Mo₂C is a transition metal carbide with dark gray coloration. In industry, it could be produced from metallic Mo and MoO₃ with carbon black at high temperatures (1300 °C+). It has two stable modifications: α-Mo₂C (orthorhombic, Pbcn, Fe₂N-zeta-like [66]) and β-Mo₂C (hexagonal, P63/mmc, vanadium nitride-like [67]).

The comparisons of the α-Mo₂C and β-Mo₂C are given in **Table 1**, **Table 2**, and **Fig.5**:

Table 1. Crystallographic characteristics of Mo₂C phases

Name	Phase	Crystal system	Space group	Reference, ICSD coll. code
α-Mo ₂ C	α-Mo ₂ C	orthorhombic	Pbcn	1326 [66]
h-β-Mo ₂ C	β-Mo ₂ C	hexagonal	P63/mmc	43669 [68]

Table 2. Raman characteristics of Mo₂C phases (532 nm laser)

Phase	Peaks, cm ⁻¹	Reference
α-Mo ₂ C	143,170,182,213,235,652	[69]
β-Mo ₂ C	670, 840, 990	[70]

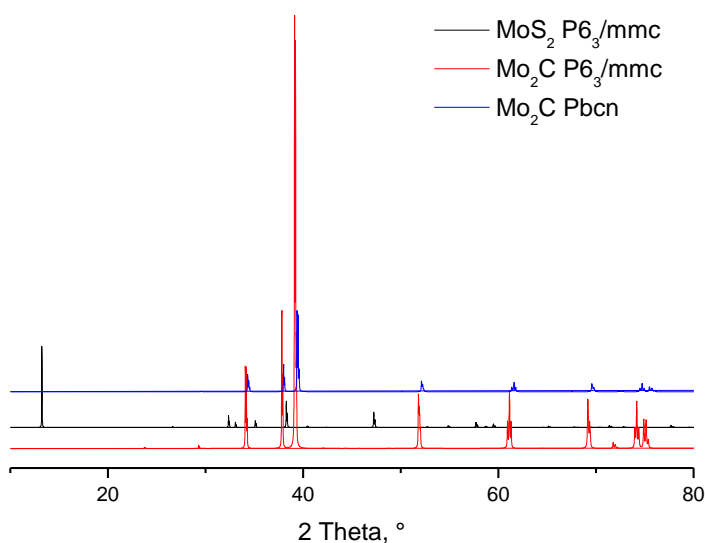


Fig.5- XRD patterns MoS_2 and Mo_2C were simulated by employing the cis of MoS_2 with $P6_3/mmc$ space group [71], the orthorhombic $\alpha\text{-Mo}_2\text{C}$ crystal with $Pbcn$ space group [66], and the hexagonal $\beta\text{-Mo}_2\text{C}$ P with $6_3/mmc$ space group [68].

The $\beta\text{-Mo}_2\text{C}$ has activity in RWGS, ethane dry reforming (DRE) and ODH-CO_2 . Oxygen modification of carbide could promote C-H bond scission. For not modified $\beta\text{-Mo}_2\text{C}$ an interaction of ethane with carbon dioxide could result in both ODH-CO_2 and dry reforming.

Copper Mo_2C is known as the catalyst for CO_2 hydrogenation to MeOH [72]. Also, $\text{Cu}/\beta\text{-Mo}_2\text{C}$ catalysts are active in RWGS at 300-600 °C and demonstrate high stability [73]. Another study of RWGS by Ma et al. reported a promising Mo_2C sub-nanometer size (around 0.5 nm) catalyst with a CO selectivity till 99.6% [74]. Dixit et al. presented oxygen covered $\beta\text{-Mo}_2\text{C}$ as a promising and low-cost catalyst for RWGS [75]. The authors have studied how surface oxygen changes the energy of CO_2 conversion to CO. Based on the earliest studies, the presence of oxygen leads to the formation of an oxygenated carbide surface.

For ODH-CO_2 some catalytic properties of molybdenum carbide catalyst were by M. Porosoff et al. [18], S. Yao et al. [41], W. Marquart et al. [42]. A more detailed description of the use of carbide catalysts is presented in **section 1.4**.

The dry ethane reforming is a co-reaction taking place with ODH-CO_2 over a Mo_2C catalyst. Yao et al. reported the catalyst modification with Fe and O with the goal to decrease its dry

reforming ability [41]. With increasing CO₂ pressure, Mo carbide and Fe-doped Molybdenum carbide started to oxidize. It was illustrated by XPS, where the peaks distribution showed the formation of Mo(II) and Mo(IV).

The β -Mo₂C is a highly oxophilic solid which explains its oxidation to MoO₂. It could be oxidized under CO₂-rich and O₂-rich flow. It is mentioned as one of the basic problems for dry methane reforming and water gas shift catalyst design.

1.5.4. Mo oxycarbides

Oxycarbides could appear during the catalytic interaction of CO₂ with Mo₂C, mostly at high temperatures (700 °C+) and pressure of 1-40 bar. Their composition is determined by the general formula (Mo₂C)_xO_y. The X-ray diffraction pattern was simulated by S. R. J. Likith [76] (**Fig. 6**). Oxycarbides' formation could also be determined by *in situ* XANES or XPS.

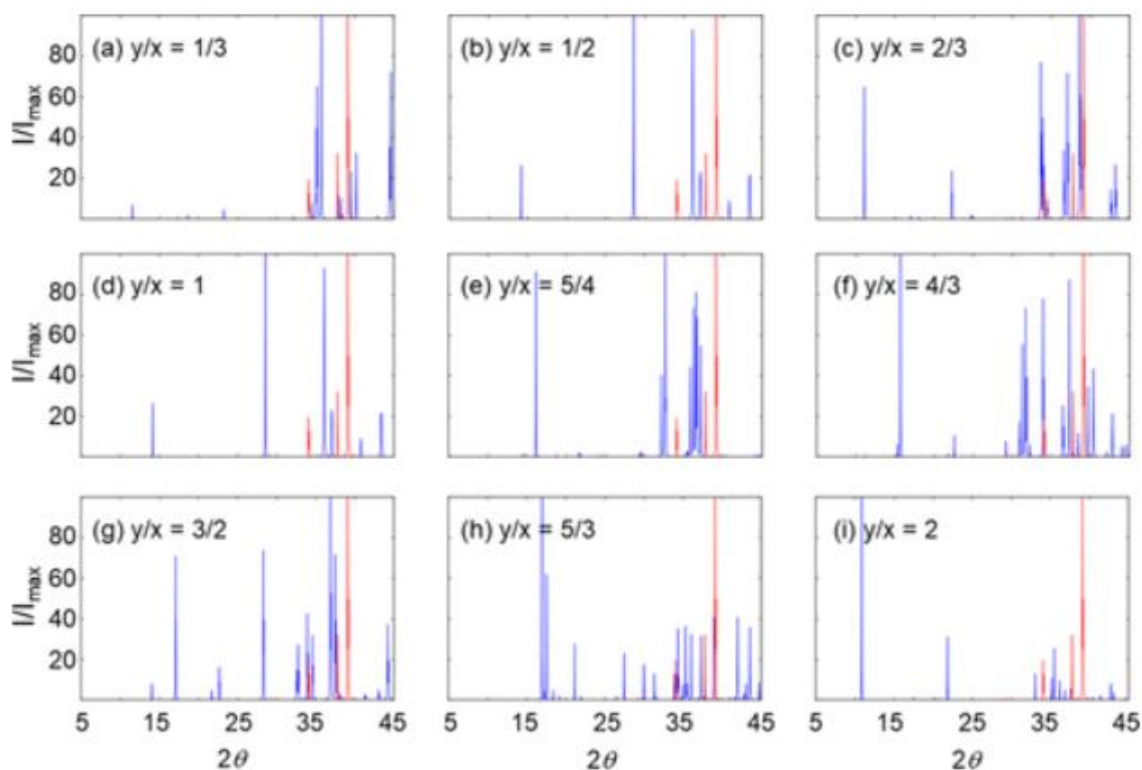
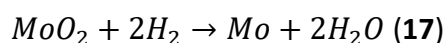
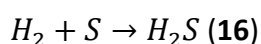
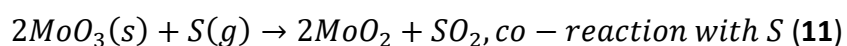
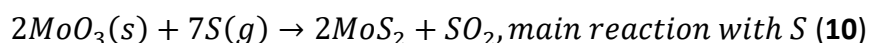


Fig.6- Simulation of the XRD patterns for the oxycarbides (Mo₂C)_xO_y for $y/x \leq 2$. The parent Mo₂C XRD pattern is indicated in red for each predicted pattern. Reproduced from [76].

1.5.5. Phases transformation

1.5.5.1. Phase transformation during sulfidic catalyst precursors formation

Sulfurizing of the oxidic phase can be done with different S-contained agents. The MoO₃ precursors with various morphology convert to disulfide under H₂S/H₂ flow in a wide temperature range: 350-800 °C. Elemental sulfur could also be used in this reaction. For instance, at 800 °C S is evaporated in a special furnace and interacts with MoO₃ films [77]. During sulfurizing reaction MoO₂, MoOS₂ and SO₂ are produced as co-products (**reactions 10-12**, [78]). In the case of H₂S sulfurizing agent (**reactions 13-18**, [79]), it is possible the presence oxysulfide and dioxide before complete MoO₃ conversion. The H₂ presence allows preventing the formation of S via its conversion to H₂S (**reaction 16**).



1.5.5.2. Potential *in situ* catalyst phases transformation under test conditions

Conversion of oxides to carbide

Various forms of Mo₂C could be obtained by MoO₃ carburization. For instance, with urea as a carbon precursor, it is possible to obtain α-Mo₂C from α-MoO₃ [80]. Under CH₄/N₂ carburizing mixture at 1110 °C the molybdenum trioxide transformation is ultrafast and leads to the β-form [81]. Molybdenum carbide in the β-form appeared under CH₄/N₂ flow from MoO₃ nanosheets. The carbides convert to oxycarbides during the DRM catalytic tests [82]. In the case of CH₄/H₂ carburization mixture, in addition to Mo₂C formation, the MoO₃ could be reduced to MoO₂ [83].

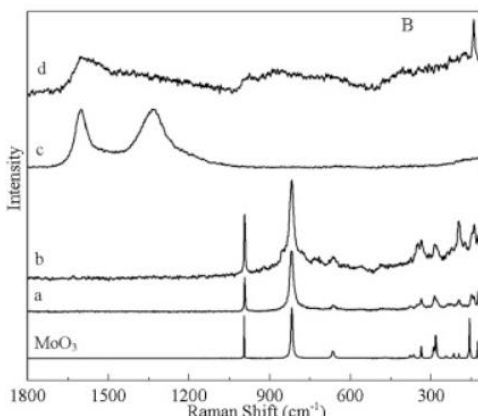


Fig.8- Raman spectra of molybdenum carbides carburized from MoO₃ under various gas streams: (a) 20% CH₄/80% H₂, (b) 10% C₂H₆/90% H₂, (c) 5% C₄H₁₀/95% H₂, and (d) 20% CO/80% H₂ at 700 °C (heating rate 1 °C/min, 10 h under the stream). Reproduced from [86].

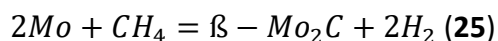
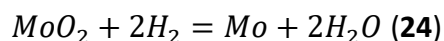
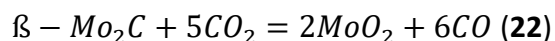
It was reported how the composition or the alkane/H₂ ratio influences the final product [86]. In case of high alkane/hydrogen ratio the XRD patterns had lower resolution and the Raman spectra compose two well-formed characteristic bands of graphitic carbon instead of Mo-C vibration bands. The intensity of the last ones could be too low to be detected.

MoO₃ could interact with CO and reduce to MoO₂ (**reaction 20**, [87]). However, in excess of CO under the same conditions (≈1000 °C), the formation of Mo₂C could take place (**reaction 21**).



Conversion of carbide to oxides

The major part of published studies described the conversion of the carbide phase to oxide due to the dry methane reforming process. Possible interconversions between Mo₂C and MoO₂ were described by P. Liang et al. [28] (**reactions 22-25**):



Conversion of MoS₂ to Mo₂C

The Mo₂C synthesis from MoS₂ is an alternative to the oxide carburization route. Under the CH₄/H₂ flow at a high temperature of about 800 °C, disulfide interacts with methane and forms a carbide [50]. The lowest temperature for this transformation mentioned in the literature is 750 °C [49]. MoS₂ carburization is a rapid process, in 25 min, sulfidic nanosheets vertically were aligned by Mo₂C nanosheets under CH₄/H₂/Ar flow. For pure sulfide, chemical conversion to Mo₂C Raman was successfully applied for phase detection [50].

The carbide growth mechanism on MoS₂ was described in reference [50]. The authors proved that Mo₂C formation would occur only on multilayered MoS₂. Thus, the multilayered nature of the sulfide precursor can be indirectly confirmed.

Conversion of MoS₂ to MoO₂

Molybdenum disulfide could be converted to dioxide. MoS₂ oxidized to MoO₂ under O₂ flow and then to MoO₃.

At 10 bar and 500 °C during the CO₂ methanation, MoS₂ was deactivated by partial conversion to MoO₂ [46]. Thus, it could be served as additional proof of MoS₂ resistance under mild oxidant as CO₂. For disulfide interaction with carbon dioxide, only a high temperature is not enough. Transformation of MoS₂ occurs without the formation of a C-containing phase. Raman and XPS confirmed the oxidation. By Raman spectroscopy, some changes in 1000-300 cm⁻¹ were observed, sulfide is exposed to CO₂, and associated peaks to disulfide at 380-630 decreased, but a novel peak at 810 cm⁻¹ has appeared. By XPS, it was noticed some changes in the Mo 3d peak and the distribution of the O 1s peak could be explained by the formation of some oxidized Mo(VI) components in low amounts. Summarizing these factors, the authors concluded MoS₂ oxidation by CO₂ to MoO₂.

Thermal stability for the designed catalyst is a necessary but not sufficient condition. When operating in the temperature range of 700 °C+, the chemical conversion of MoO₃, Mo₂C, MoS₂ should be investigated. When designing materials with certain properties, possible transitions between phases must be taken into account.

2. Catalyst support

The application of bulky oxide, sulfide, or carbide phases as heterogeneous catalysts implies several limitations. It usually requires the use of catalyst support with specific chemistry and surface and textural properties. The support is important since it is preventing the active phase agglomeration and adds a shape-sieve effect. Also, the support could contribute to the catalytic activity due to the presence of active sites.

Oxide supports as CeO_2 , ZrO_2 represent particular interest for oxidative processes since they exhibit red-ox properties [19]. These materials could potentially lower temperature for successful ethane conversion.

Choosing the support for a high-temperature process with potential heavy aromatics or coke formation is a challenge. On the other hand, highly acidic supports could improve catalyst activity for the dehydrogenation step [88] but leads to faster deactivation. For active phases supported on microporous materials, access to the internal and external active sites could be blocked by bulky products or coke deposition. Thus, the mesoporous carriers are preferable for this type of catalyst. However, Al-containing mesoporous supports were found inappropriate for Mo catalysts. Framework Al could interact with Mo resulting in the formation $\text{Al}_2(\text{MoO}_4)_3$ [89]. Hence, we consider the possibility to use zeolitic-type support for our molybdenum sulfide catalysts. More precisely, we consider the possibility to use all silica or alumina-silica embryonic zeolites as carriers [89].

2.1. Embryonic zeolite and its properties

Embryonic zeolites (EZ) were designed to overcome the mass transfer limitation of bulky molecules in zeolite materials. The embryonic zeolites were developed as a material with a super microporous system (1-2 nm) and ultra-small size (3-5 nm). Such characteristics improve the accessibility of the active sites. Prior to the development of EZ, only in Ge-silicate zeolites the pore size was larger than 1nm, however, they exhibit extremely low hydrothermal stability and thus cannot be used in the envisaged application. In contrast, the EZ, thanks to their high pore accessibility, moderate acid sites, and very high specific surface represent a valuable alternative as catalyst's support [90,91].

The EZ are X-ray amorphous (**Fig.9**), which makes their structural characterization difficult since it is based namely on physisorption methods.

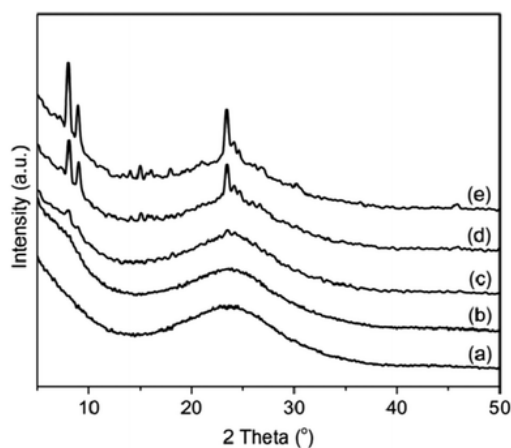


Fig. 9- XRD patterns of embryonic zeolite and nanosized zeolite ZSM-5: (a) RT-100, (b) HT-100-12, (c) HT-100-18, (d) HT-100-24, and (e) HT-100-29. Reproduced from [90].

As prepared EZs have I type sorption isotherm (**Fig.10**) with higher uptake of microporous volumes compared to ZSM-5. After ion exchange, it is changed to a micro-mesoporous structure.

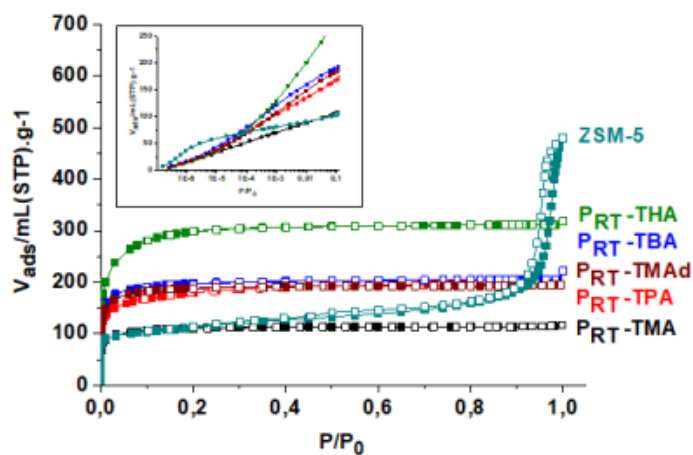


Fig. 10- N₂ adsorption/desorption isotherms of embryonic zeolites (P_{RT}) synthesized with various structural directing agents (SDA): TMA, TPA, TMAd, TBA, THA. Reproduced from [92].

The infrared (IR) spectroscopy was used to confirm the formation of a double-membered ring for EZ with MFI structure (**Fig.11**) by bands at 560 and 1200 cm^{-1} . Also, the bands at 560 and 460 cm^{-1} are used for zeolite crystallinity characterization [92].

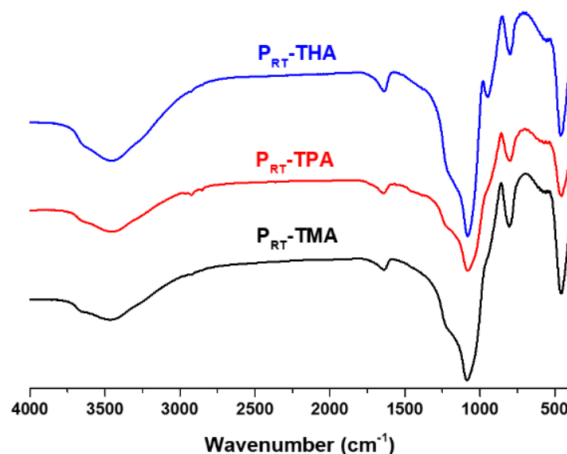


Fig.11- FTIR spectra of various embryonic zeolites: P_{RT}-THA, P_{RT}-TPA, P_{RT}-TMA. Reproduced from [92].

2.2. Application of embryonic zeolites as catalyst carriers

There are no publications on the metal-modified EZs. Thus, the preparation of metal-modified embryonic zeolites is a pioneering work, with all related difficulties preparation and characterization difficulties. Moreover, it was necessary to stabilize the metal species, since migration and aggregation at very high temperatures are assumed.

3. Crystalline thiogallates for ODH-CO₂

Another task for this research was the synthesis of high-temperature stable sulfides with potential catalytic properties for ODH-CO₂. One of the initial requirements was a 3D, zeolite-like, supercluster-based structure. Such compounds are presented in the following works: Zn_{0.81}Ge_{3.19}S₈, Cd_{0.68}Sn_{3.32}Se₈ [93], [In₁₀S₁₂Se₈]¹⁰⁻ [94],[Cu₅In₃₀S₅₃]¹¹⁻ [95]. However, all known 3D porous zeolite-like, monometallic, or bimetallic sulfides have not demonstrated thermal resistance at a temperature higher than 600 °C.

Therefore, we turn our attention to bulk crystalline materials with the necessary thermal stability. Alkali ternary thiogallates with the general formula AGaS₂ (A=Na [96], Cs [97], Ag [98–

100]) are high-temperature resistant sulfides. One of the most known and important thiogallate is AgGaS_2 which has been used as a benchmark for second harmonic generation (SHG), i.e., it has an industrial application. A crystal of $5 \times 5 \times 1$ mm size costs 1770 euros in 2022 [101].

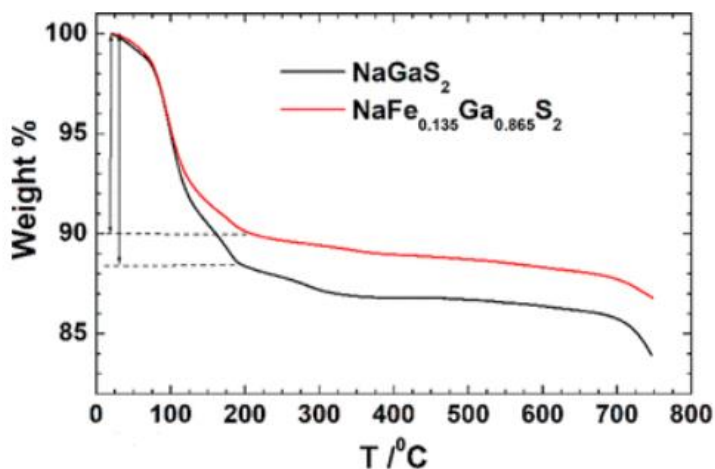


Fig.12-TGA curves of NaGaS_2 and $\text{NaFe}_{0.135}\text{Ga}_{0.865}\text{S}_2$. Reproduced from [102]. (Weight loss at 40-200 °C is attributed to the adsorbed water.)

The LiGaS_2 potentially could also be used instead of AgGaS_2 . Cation replacement improves two-photon absorption, rising thermal conductivity, and phase-matching [103].

The ion exchange ability of thiogallates is reported only for NaGaS_2 . For this compound, sodium cations could be exchanged with Co^{2+} , Ni^{2+} , Pb^{2+} , Cd^{2+} [96]. NaGaS_2 is potential optical material for high-power laser frequency conversion [104]. because the interest in this thiogallate is due to the similar on-linear optical coefficient with AgGaS_2 . At the same time, it shows a more promising performance than infrared non-linear optical materials.

The $\text{KGaS}_2:\text{Eu}^{2+}$, may be applied as a P-host for phosphor-converted white light-emitting diodes [105]. At the moment, the component is not widely used.

As these thiogallates are more interesting as optic materials, a major part of the synthesis is presented as a high-temperature ampule synthesis for the preparation of single crystals. Nanoparticles synthesis was mentioned only for AgGaS_2 . The nanosized orthorhombic silver thiogallate was tested in a standard photocatalytic characteristic Rhodamine B degradation. The degradation efficiency was equal 86-93 % in 90 min.

The bulk AgGaS_2 also demonstrated high photocatalytic activity and temperature resistance at $850\text{ }^\circ\text{C}$ [106]. The H_2 was produced from H_2S produced by hydrolysis of $\text{Na}_2\text{S}-\text{Na}_2\text{SO}_3$ solution under visible light in a closed system.

NaGaS_2 , KGaS_2 , RbGaS_2 , or low-temperature CsGaS_2 are crystallized as the TlGaS_2 . Their structures are illustrated in **Fig. 13**. This structure is built-up of Ga_4S_{10} adamantane-like units. These units are connected through the S-atoms and form layers with the general formula $[\text{GaS}_2]^\infty$. The alkali cations are located between layers and balance the framework charge [102].

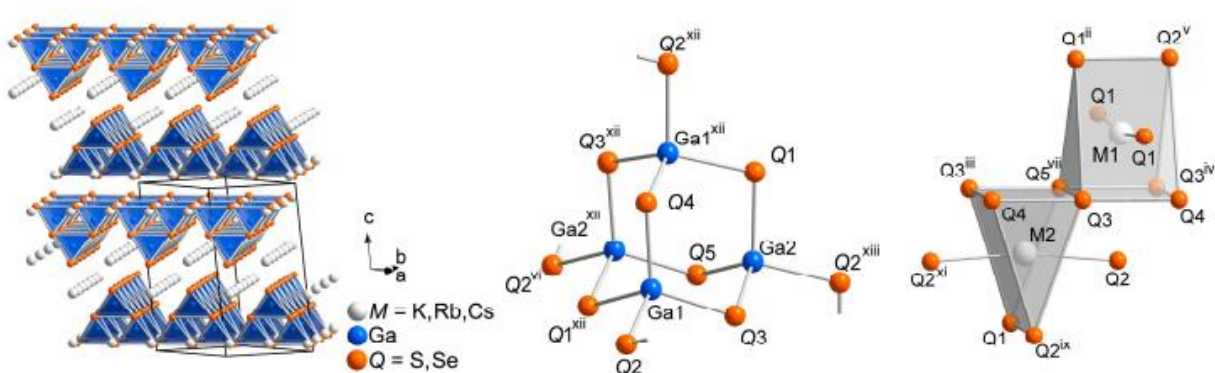


Fig.13- Structure of the crystal structures of the MGaQ_2 (a-c), where $M=\text{K, Rb, Cs}$ and $Q=\text{S, Se}$: a) the stacking of the anionic layers in the TlGaSe_2 -like structure type; b) building blocks supertetrahedral Ga_4Q_{10} ($Q=\text{S,Se}$); c) coordination polyhedra. Reproduced from [107].

In the early 80ies a thiogallate with Aa space group was reported [108]. Later for the series of AGaS_2 ($A=\text{alkali metal: Na, K, Rb, Cs}$), it was corrected and resolved as monoclinic with a space group C2/C [105], while the LiGaS_2 exhibits $\text{Pna}2_1$ space group (**Fig. 14**). The ternary thiogallates presented not only AGaS_2 ($A=\text{alkali metal: Na, K, Rb, Cs}$), also recently some new frameworks: A_5GaS_4 ($A=\text{Li and Na}$) were announced. These new thiogallates crystallized in $\text{P2}_1/\text{m}$ and Pbca , respectively (**Fig. 13**) [109].

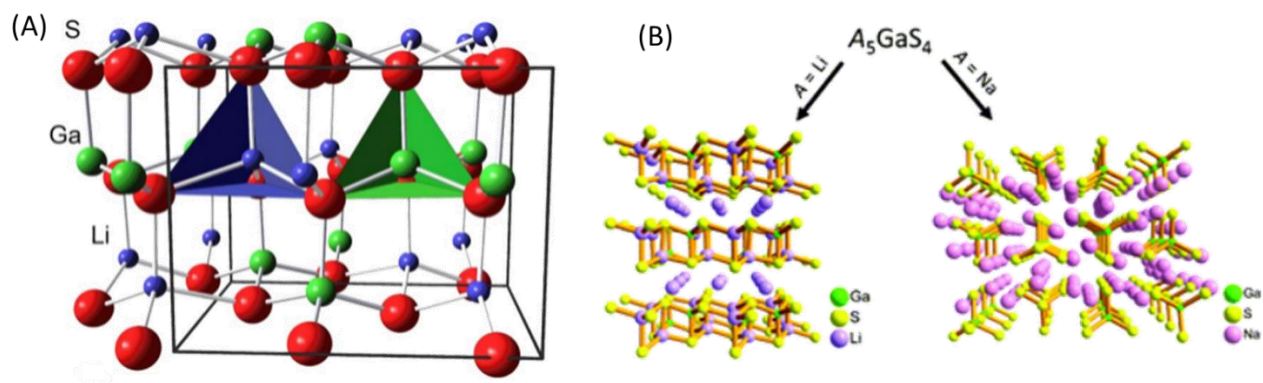


Fig. 14- A: Structure of LiGaS_2 (space group $\text{Pna}21$): left tetrahedron Li-S_4 and right tetrahedron Ga-S_4 . Color code: blue-Li, green-Ga, and red-S. Reproduced from [110]; B: Structure of A_5GaS_4 ($\text{A}=\text{Na}, \text{Li}$): Li_5GaS_4 - $\text{P}2_1/\text{m}$ space group (left), Na_5GaS_4 - Pbca (right). Reproduced from [109].

References

- [1] M. Myint, B. Yan, J. Wan, S. Zhao, J.G. Chen, Reforming and oxidative dehydrogenation of ethane with CO₂ as a soft oxidant over bimetallic catalysts, *J. Catal.* 343 (2016) 168–177. <https://doi.org/10.1016/j.jcat.2016.02.004>.
- [2] Y.A. Daza, J.N. Kuhn, CO₂ conversion by reverse water gas shift catalysis: comparison of catalysts, mechanisms and their consequences for CO₂ conversion to liquid fuels, *RSC Adv.* 6 (2016) 49675–49691. <https://doi.org/10.1039/C6RA05414E>.
- [3] M. González-Castaño, B. Dorneanu, H. Arellano-García, The reverse water gas shift reaction: a process systems engineering perspective, *React. Chem. Eng.* (2021) 954–976. <https://doi.org/doi.org/10.1039/D0RE00478B>.
- [4] B. Yan, X. Yang, S. Yao, J. Wan, M. Myint, E. Gomez, Z. Xie, S. Kattel, W. Xu, J.G. Chen, Dry Reforming of Ethane and Butane with CO₂ over PtNi/CeO₂ Bimetallic Catalysts, *ACS Catal.* 6 (2016) 7283–7292. <https://doi.org/10.1021/acscatal.6b02176>.
- [5] R.E. Brooks, Modeling the North American Market for Natural Gas Liquids, in: Anchorage, 2013.
- [6] I. Amghizar, J.N. Dedeayne, D.J. Brown, G.B. Marin, K.M. Van Geem, Sustainable innovations in steam cracking: CO₂ neutral olefin production, *React. Chem. Eng.* 5 (2020) 239–257. <https://doi.org/10.1039/C9RE00398C>.
- [7] BASF, SABIC and Linde join forces to realize the world's first electrically heated steam cracker furnace, (n.d.). <https://www.basf.com/global/en/who-we-are/sustainability/whats-new/sustainability-news/2021/basf-sabic-and-linde-join-forces-to-realize-wolds-first-electrically-heated-steam-cracker-furnace.html> (accessed March 9, 2022).
- [8] C.L. Basel, Clariant unveils groundbreaking catalysts developed jointly with Linde Engineering for novel ethylene production technology, Clariant Ltd. (n.d.). <https://www.clariant.com/en/Corporate/News/2021/10/Clariant-unveils-groundbreaking-catalysts-developed-jointly-with-Linde-Engineering-for-novel-ethylen> (accessed May 6, 2022).
- [9] L.M. Neal, V.P. Haribal, F. Li, Intensified Ethylene Production via Chemical Looping through an Exergetically Efficient Redox Scheme, *IScience.* 19 (2019) 894–904. <https://doi.org/10.1016/j.isci.2019.08.039>.
- [10] D. Melzer, P. Xu, D. Hartmann, Y. Zhu, N.D. Browning, M. Sanchez-Sanchez, J.A. Lercher, Atomic-Scale Determination of Active Facets on the MoVTeNb Oxide M1 Phase and Their Intrinsic Catalytic Activity for Ethane Oxidative Dehydrogenation, *Angew. Chem.* 128 (2016) 9019–9023. <https://doi.org/10.1002/ange.201600463>.
- [11] EDHOX™ technology, Linde Eng. (n.d.). <https://www.linde-engineering.com/en/process-plants/petrochemical-plants/edhox-technology/index.html> (accessed June 6, 2022).
- [12] D. Li, R. Xu, X. Li, Z. Li, X. Zhu, K. Li, Chemical Looping Conversion of Gaseous and Liquid Fuels for Chemical Production: A Review, *Energy Fuels.* 34 (2020) 5381–5413. <https://doi.org/10.1021/acs.energyfuels.0c01006>.

- [13] P. Novotný, S. Yusuf, F. Li, H.H. Lamb, Oxidative dehydrogenation of ethane using MoO₃/Fe₂O₃ catalysts in a cyclic redox mode, *Catal. Today*. 317 (2018) 50–55. <https://doi.org/10.1016/j.cattod.2018.02.046>.
- [14] S. Yusuf, L. Neal, V. Haribal, M. Baldwin, H.H. Lamb, F. Li, Manganese silicate based redox catalysts for greener ethylene production via chemical looping – oxidative dehydrogenation of ethane, *Appl. Catal. B Environ.* 232 (2018) 77–85. <https://doi.org/10.1016/j.apcatb.2018.03.037>.
- [15] D. Fairuzov, I. Gerzeliev, A. Maximov, E. Naranov, Catalytic Dehydrogenation of Ethane: A Mini Review of Recent Advances and Perspective of Chemical Looping Technology, *Catalysts*. 11 (2021) 833. <https://doi.org/10.3390/catal11070833>.
- [16] S. Yusuf, L.M. Neal, F. Li, Effect of Promoters on Manganese-Containing Mixed Metal Oxides for Oxidative Dehydrogenation of Ethane via a Cyclic Redox Scheme, *ACS Catal.* 7 (2017) 5163–5173. <https://doi.org/10.1021/acscatal.7b02004>.
- [17] P. Novotný, S. Yusuf, F. Li, H.H. Lamb, Oxidative dehydrogenation of ethane using MoO₃/Fe₂O₃ catalysts in a cyclic redox mode, *Catal. Today*. 317 (2018) 50–55. <https://doi.org/10.1016/j.cattod.2018.02.046>.
- [18] S.A. Theofanidis, C. Loizidis, E. Heracleous, A.A. Lemonidou, CO₂-oxidative ethane dehydrogenation over highly efficient carbon-resistant Fe-catalysts, *J. Catal.* 388 (2020) 52–65. <https://doi.org/10.1016/j.jcat.2020.05.004>.
- [19] T.A. Bugrova, V.V. Dutov, V.A. Svetlichnyi, V. Cortés Corberán, G.V. Mamontov, Oxidative dehydrogenation of ethane with CO₂ over CrO_x catalysts supported on Al₂O₃, ZrO₂, CeO₂ and CexZr_{1-x}O₂, *Catal. Today*. 333 (2019) 71–80. <https://doi.org/10.1016/j.cattod.2018.04.047>.
- [20] P. Liu, L. Zhang, M. Li, N. Sun, W. Wei, Recent progress in Cr-based catalysts for oxidative dehydrogenation of light alkanes by employing CO₂ as a soft oxidant, *Clean Energy*. 5 (2021) 623–633. <https://doi.org/10.1093/ce/zkab036>.
- [21] T. Lei, C. Miao, W. Hua, Y. Yue, Z. Gao, Oxidative Dehydrogenation of Ethane with CO₂ over Au/CeO₂ Nanorod Catalysts, *Catal. Lett.* 148 (2018) 1634–1642. <https://doi.org/10.1007/s10562-018-2389-1>.
- [22] A. Talati, M. Haghighi, F. Rahmani, Oxidative dehydrogenation of ethane to ethylene by carbon dioxide over Cr/TiO₂–ZrO₂ nanocatalyst: Effect of active phase and support composition on catalytic properties and performance, *Adv. Powder Technol.* 27 (2016) 1195–1206. <https://doi.org/10.1016/j.apt.2016.04.003>.
- [23] X. Wang, Y. Wang, B. Robinson, Q. Wang, J. Hu, Ethane oxidative dehydrogenation by CO₂ over stable CsRu/CeO₂ catalyst, *J. Catal.* 413 (2022) 138–149. <https://doi.org/10.1016/j.jcat.2022.06.021>.
- [24] F. Rahmani, M. Haghighi, One-pot hydrothermal synthesis of ZSM-5–CeO₂ composite as a support for Cr-based nanocatalysts: influence of ceria loading and process conditions on CO₂-enhanced dehydrogenation of ethane, *RSC Adv.* 6 (2016) 89551–89563. <https://doi.org/10.1039/C6RA15787D>.
- [25] H. Guo, H. He, C. Miao, W. Hua, Y. Yue, Z. Gao, Ethane conversion in the presence of CO₂ over Co-based ZSM-5 zeolite: Co species controlling the reaction pathway, *Mol. Catal.* 519 (2022) 112155. <https://doi.org/10.1016/j.mcat.2022.112155>.

- [26] Z. Xie, X. Wang, X. Chen, P. Liu, J.G. Chen, General Descriptors for CO₂-Assisted Selective C–H/C–C Bond Scission in Ethane, *J. Am. Chem. Soc.* 144 (2022) 4186–4195. <https://doi.org/10.1021/jacs.1c13415>.
- [27] B. Yan, S. Yao, S. Kattel, Q. Wu, Z. Xie, E. Gomez, P. Liu, D. Su, J.G. Chen, Active sites for tandem reactions of CO₂ reduction and ethane dehydrogenation, *Proc. Natl. Acad. Sci.* 115 (2018) 8278–8283. <https://doi.org/10.1073/pnas.1806950115>.
- [28] P. Liang, H. Gao, Z. Yao, R. Jia, Y. Shi, Y. Sun, Q. Fan, H. Wang, Simple synthesis of ultrasmall β-Mo₂C and α-MoC_{1-x} nanoparticles and new insights into their catalytic mechanisms for dry reforming of methane, *Catal. Sci. Technol.* 7 (2017) 3312–3324. <https://doi.org/10.1039/C7CY00708F>.
- [29] T. Osaki, T. Horiuchi, K. Suzuki, T. Mori, Catalyst performance of MoS₂ and WS₂ for the CO₂-reforming of CH₄ Suppression of carbon deposition, *Appl. Catal. Gen.* 155 (1997) 229–238. [https://doi.org/10.1016/S0926-860X\(96\)00391-2](https://doi.org/10.1016/S0926-860X(96)00391-2).
- [30] R.B. Levy, M. Boudart, Platinum-Like Behavior of Tungsten Carbide in Surface Catalysis, *Science*. 181 (1973) 547–549. <https://doi.org/10.1126/science.181.4099.547>.
- [31] J.H. Sinfelt, D.J.C. Yates, Effect of Carbiding on the Hydrogenolysis Activity of Molybdenum, *Nat. Phys. Sci.* 229 (1971) 27–28. <https://doi.org/10.1038/physci229027b0>.
- [32] A. Kurlov, E.B. Deeva, P.M. Abdala, D. Lebedev, A. Tsoukalou, A. Comas-Vives, A. Fedorov, C.R. Müller, Exploiting two-dimensional morphology of molybdenum oxycarbide to enable efficient catalytic dry reforming of methane, *Nat. Commun.* 11 (2020) 4920. <https://doi.org/10.1038/s41467-020-18721-0>.
- [33] J. Huang, T. Huang, L. Liu, W. Huang, R. Ma, Mo₂C/SBA-15 Modified by Ni for the Dry Reforming of Methane, *Energy Sources Part Recovery Util. Environ. Eff.* 33 (2011) 2249–2256. <https://doi.org/10.1080/15567036.2010.543999>.
- [34] K. Ahmad, K. Polychronopoulou, M. Abi Jaoude, CH₄ valorisation reactions: A comparative thermodynamic analysis and their limitations, *Fuel*. 320 (2022) 123877. <https://doi.org/10.1016/j.fuel.2022.123877>.
- [35] S. Zhang, C. Shi, B. Chen, Y. Zhang, Y. Zhu, J. Qiu, C. Au, Catalytic role of β-Mo₂C in DRM catalysts that contain Ni and Mo, *Catal. Today*. 258 (2015) 676–683. <https://doi.org/10.1016/j.cattod.2015.01.014>.
- [36] Q. Tao, Z. Wang, B. Jayasundera, C. Guo, Y. Gan, L. Zhang, Z. Lu, H. Tan, C. Yan, Enhanced catalytic activity of Ni–Mo₂C/La₂O₃–ZrO₂ bifunctional catalyst for dry reforming of methane, *J. Mater. Sci.* 53 (2018) 14559–14572. <https://doi.org/10.1007/s10853-018-2642-4>.
- [37] Z. Yao, J. Jiang, Y. Zhao, F. Luan, J. Zhu, Y. Shi, H. Gao, H. Wang, Insights into the deactivation mechanism of metal carbide catalysts for dry reforming of methane via comparison of nickel-modified molybdenum and tungsten carbides, *RSC Adv.* 6 (2016) 19944–19951. <https://doi.org/10.1039/C5RA24815A>.
- [38] Y. Diao, X. Zhang, Y. Liu, B. Chen, G. Wu, C. Shi, Plasma-assisted dry reforming of methane over Mo₂C-Ni/Al₂O₃ catalysts: Effects of β-Mo₂C promoter, *Appl. Catal. B Environ.* 301 (2022) 120779. <https://doi.org/10.1016/j.apcatb.2021.120779>.
- [39] M.D. Porosoff, M.N.Z. Myint, S. Kattel, Z. Xie, E. Gomez, P. Liu, J.G. Chen, Identifying Different Types of Catalysts for CO₂ Reduction by Ethane through Dry Reforming and

- Oxidative Dehydrogenation, *Angew. Chem. Int. Ed.* 54 (2015) 15501–15505. <https://doi.org/10.1002/anie.201508128>.
- [40] F. Solymosi, R. Nemeth, The oxidative dehydrogenation of ethane with CO₂ over Mo₂C/SiO₂ catalyst, *Cat Lett.* 62 (1999) 197–200.
- [41] S. Yao, B. Yan, Z. Jiang, Z. Liu, Q. Wu, J.H. Lee, J.G. Chen, Combining CO₂ Reduction with Ethane Oxidative Dehydrogenation by Oxygen-Modification of Molybdenum Carbide, *ACS Catal.* 8 (2018) 5374–5381. <https://doi.org/10.1021/acscatal.8b00541>.
- [42] W. Marquart, M. Claeys, N. Fischer, Conversion of CO₂ and small alkanes to platform chemicals over Mo₂C-based catalysts, *Faraday Discuss.* 230 (2021) 68–86. <https://doi.org/10.1039/D0FD00138D>.
- [43] P. Liu, Y. Choi, Y. Yang, M.G. White, Methanol Synthesis from H₂ and CO₂ on a Mo₆S₈ Cluster: A Density Functional Study, *J. Phys. Chem. A.* 114 (2010) 3888–3895. <https://doi.org/10.1021/jp906780a>.
- [44] P. Cui, R. Sun, L. Xiao, W. Wu, Exploring the Effects of the Interaction of Carbon and MoS₂ Catalyst on CO₂ Hydrogenation to Methanol, *Int. J. Mol. Sci.* 23 (2022) 5220. <https://doi.org/10.3390/ijms23095220>.
- [45] J. Hu, L. Yu, J. Deng, Y. Wang, K. Cheng, C. Ma, Q. Zhang, W. Wen, S. Yu, Y. Pan, J. Yang, H. Ma, F. Qi, Y. Wang, Y. Zheng, M. Chen, R. Huang, S. Zhang, Z. Zhao, J. Mao, X. Meng, Q. Ji, G. Hou, X. Han, X. Bao, Y. Wang, D. Deng, Sulfur vacancy-rich MoS₂ as a catalyst for the hydrogenation of CO₂ to methanol, *Nat. Catal.* 4 (2021) 242–250. <https://doi.org/10.1038/s41929-021-00584-3>.
- [46] A. Primo, J. He, B. Jurca, B. Cojocar, C. Bucur, V.I. Parvulescu, H. Garcia, CO₂ methanation catalyzed by oriented MoS₂ nanoplatelets supported on few layers graphene, *Appl. Catal. B Environ.* 245 (2019) 351–359. <https://doi.org/10.1016/j.apcatb.2018.12.034>.
- [47] M. Gaillard, M. Virginie, A.Y. Khodakov, New molybdenum-based catalysts for dry reforming of methane in presence of sulfur: A promising way for biogas valorization, *Catal. Today.* 289 (2017) 143–150. <https://doi.org/10.1016/j.cattod.2016.10.005>.
- [48] F. Goodarzi, L.P. Hansen, S. Helveg, J. Mielby, T.T.M. Nguyen, F. Joensen, S. Kegnæs, The catalytic effects of sulfur in ethane dehydroaromatization, *Chem. Commun.* (2020). <https://doi.org/10.1039/D0CC00408A>.
- [49] Z. Zhao, F. Qin, S. Kasiraju, L. Xie, M.K. Alam, S. Chen, D. Wang, Z. Ren, Z. Wang, L.C. Grabow, J. Bao, Vertically Aligned MoS₂/Mo₂C hybrid Nanosheets Grown on Carbon Paper for Efficient Electrocatalytic Hydrogen Evolution | *ACS Catalysis*, (2017). <https://pubs-acsc.org/inc.bib.cnrs.fr/doi/abs/10.1021/acscatal.7b02885> (accessed August 31, 2021).
- [50] J. Jeon, Y. Park, S. Choi, J. Lee, S.S. Lim, B.H. Lee, Y.J. Song, J.H. Cho, Y.H. Jang, S. Lee, Epitaxial Synthesis of Molybdenum Carbide and Formation of a Mo₂C/MoS₂ Hybrid Structure *via* Chemical Conversion of Molybdenum Disulfide, *ACS Nano.* 12 (2018) 338–346. <https://doi.org/10.1021/acsnano.7b06417>.
- [51] T. Leisegang, A.A. Levin, J. Walter, D.C. Meyer, In situ X-ray analysis of MoO₃ reduction, *Cryst. Res. Technol.* 40 (2005) 95–105. <https://doi.org/10.1002/crat.200410312>.
- [52] A. Katrib, P. Leflaive, L. Hilaire, G. Maire, Molybdenum based catalysts. I. MoO₂ as the active species in the reforming of hydrocarbons, *Catal. Lett.* 38 (1996) 95–99. <https://doi.org/10.1007/BF00806906>.

- [53] O.G. Marin Flores, S. Ha, Activity and stability studies of MoO₂ catalyst for the partial oxidation of gasoline, *Appl. Catal. Gen.* 352 (2009) 124–132. <https://doi.org/10.1016/j.apcata.2008.09.036>.
- [54] F. Carrasco-Marín, J. Rivera-Utrilla, E. Utrera-Hidalgo, C. Moreno-Castilla, MoO₂ as catalyst in the CO₂ gasification of activated carbons and chars, *Fuel*. 70 (1991) 13–16. [https://doi.org/10.1016/0016-2361\(91\)90088-R](https://doi.org/10.1016/0016-2361(91)90088-R).
- [55] A. Brush, E.J. Evans, G.M. Mullen, K. Jarvis, C.B. Mullins, Tunable Syn-gas ratio via bireforming over coke-resistant Ni/Mo₂C catalyst, *Fuel Process. Technol.* 153 (2016) 111–120. <https://doi.org/10.1016/j.fuproc.2016.07.012>.
- [56] O. Marin-Flores, T. Turba, C. Ellefson, K. Wang, J. Breit, J. Ahn, M.G. Norton, S. Ha, Nanoparticle molybdenum dioxide: A highly active catalyst for partial oxidation of aviation fuels, *Appl. Catal. B Environ.* 98 (2010) 186–192. <https://doi.org/10.1016/j.apcatb.2010.05.028>.
- [57] F. Gaspar, C.D. Nunes, Selective Catalytic Oxidation of Benzyl Alcohol by MoO₂ Nanoparticles, *Catalysts*. 10 (2020) 265. <https://doi.org/10.3390/catal10020265>.
- [58] S. Bandaru, G. Saranya, N.J. English, C. Yam, M. Chen, Tweaking the Electronic and Optical Properties of α -MoO₃ by Sulphur and Selenium Doping – a Density Functional Theory Study, *Sci. Rep.* 8 (2018) 10144. <https://doi.org/10.1038/s41598-018-28522-7>.
- [59] H. Tian, C.A. Roberts, I.E. Wachs, Molecular Structural Determination of Molybdena in Different Environments: Aqueous Solutions, Bulk Mixed Oxides, and Supported MoO₃ Catalysts, *J. Phys. Chem. C*. 114 (2010) 14110–14120. <https://doi.org/10.1021/jp103269w>.
- [60] H. Negishi, S. Negishi, Y. Kuroiwa, N. Sato, S. Aoyagi, Anisotropic thermal expansion of layered MoO₃ crystals, *Phys. Rev. B*. 69 (2004) 064111. <https://doi.org/10.1103/PhysRevB.69.064111>.
- [61] G. Tsilomelekis, A. Christodoulakis, S. Boghosian, Support effects on structure and activity of molybdenum oxide catalysts for the oxidative dehydrogenation of ethane, *Catal. Today*. 127 (2007) 139–147. <https://doi.org/10.1016/j.cattod.2007.03.026>.
- [62] A. Okemoto, M.R. Harada, T. Ishizaka, N. Hiyoshi, K. Sato, Catalytic performance of MoO₃/FAU zeolite catalysts modified by Cu for reverse water gas shift reaction, *Appl. Catal. Gen.* 592 (2020) 117415. <https://doi.org/10.1016/j.apcata.2020.117415>.
- [63] R.J. Toh, Z. Sofer, J. Luxa, D. Sedmidubský, M. Pumera, 3R phase of MoS₂ and WS₂ outperforms the corresponding 2H phase for hydrogen evolution, *Chem. Commun.* 53 (2017) 3054–3057. <https://doi.org/10.1039/C6CC09952A>.
- [64] W. Zhao, J. Pan, Y. Fang, X. Che, D. Wang, K. Bu, F. Huang, Metastable MoS₂: Crystal Structure, Electronic Band Structure, Synthetic Approach and Intriguing Physical Properties, 2018. 24 (n.d.) 15942–15954. <https://doi.org/10.1002/chem.201801018>.
- [65] C.H. Sharma, A.P. Surendran, A. Varghese, M. Thalakulam, Stable and scalable 1T MoS₂ with low temperature-coefficient of resistance, *Sci. Rep.* 8 (2018) 12463. <https://doi.org/10.1038/s41598-018-30867-y>.
- [66] A.N. Christensen, H. Kvande, P.G. Wahlbeck, E. Näsäkkälä, A Neutron Diffraction Investigation on a Crystal of alpha-Mo₂C., *Acta Chem. Scand.* 31a (1977) 509–511. <https://doi.org/10.3891/acta.chem.scand.31a-0509>.

- [67] K. KuO, G. Hägg, A New Molybdenum Carbide, *Nature*. 170 (1952) 245–246. <https://doi.org/10.1038/170245a0>.
- [68] R.J. Fries, C.P. Kempter, 195. Dimolybdenum carbide, *Anal. Chem.* 32 (1960) 1898–1898. <https://doi.org/10.1021/ac50153a061>.
- [69] T. Li, W. Luo, H. Kitadai, X. Wang, X. Ling, Probing the Domain Architecture in 2D α -Mo₂C via Polarized Raman Spectroscopy, *Adv. Mater.* 31 (2019) 1807160. <https://doi.org/10.1002/adma.201807160>.
- [70] J. Guo, J. Wang, Z. Wu, W. Lei, J. Zhu, K. Xia, D. Wang, Controllable synthesis of molybdenum-based electrocatalysts for a hydrogen evolution reaction, *J. Mater. Chem. A*. 5 (2017) 4879–4885. <https://doi.org/10.1039/C6TA10758C>.
- [71] R.G. Dickinson, L. Pauling, THE CRYSTAL STRUCTURE OF MOLYBDENITE, 45 (1923) 1466–1471. <https://doi.org/10.1021/ja01659a020>.
- [72] A.B. Dongil, E. Blanco, J.J. Villora-Picó, A. Sepúlveda-Escribano, I. Rodríguez-Ramos, Effect of the Carbon Support and Conditions on the Carbothermal Synthesis of Cu-Molybdenum Carbide and Its Application on CO₂ Hydrogenation to Methanol, *Nanomaterials*. 12 (2022) 1048. <https://doi.org/10.3390/nano12071048>.
- [73] X. Zhang, X. Zhu, L. Lin, S. Yao, M. Zhang, X. Liu, X. Wang, Y.-W. Li, C. Shi, D. Ma, Highly Dispersed Copper over β -Mo₂C as an Efficient and Stable Catalyst for the Reverse Water Gas Shift (RWGS) Reaction, *ACS Catal.* 7 (2017) 912–918. <https://doi.org/10.1021/acscatal.6b02991>.
- [74] Y. Ma, Z. Guo, Q. Jiang, K.-H. Wu, H. Gong, Y. Liu, Molybdenum carbide clusters for thermal conversion of CO₂ to CO via reverse water-gas shift reaction, *J. Energy Chem.* 50 (2020) 37–43. <https://doi.org/10.1016/j.jechem.2020.03.012>.
- [75] M. Dixit, X. Peng, M.D. Porosoff, H.D. Willauer, G. Mpourmpakis, Elucidating the role of oxygen coverage in CO₂ reduction on Mo₂C, *Catal. Sci. Technol.* 7 (2017) 5521–5529. <https://doi.org/10.1039/C7CY01810J>.
- [76] S.R.J. Likith, C.A. Farberow, S. Manna, A. Abdulslam, V. Stevanović, D.A. Ruddy, J.A. Schaidle, D.J. Robichaud, C.V. Ciobanu, Thermodynamic Stability of Molybdenum Oxycarbides Formed from Orthorhombic Mo₂C in Oxygen-Rich Environments, *J. Phys. Chem. C*. 122 (2018) 1223–1233. <https://doi.org/10.1021/acs.jpcc.7b11110>.
- [77] S.E. Panasci, A. Koos, E. Schilirò, S. Di Franco, G. Greco, P. Fiorenza, F. Roccaforte, S. Agnello, M. Cannas, F.M. Gelardi, A. Sulyok, M. Nemeth, B. Pécz, F. Giannazzo, Multiscale Investigation of the Structural, Electrical and Photoluminescence Properties of MoS₂ Obtained by MoO₃ Sulfurization, *Nanomaterials*. 12 (2022) 182. <https://doi.org/10.3390/nano12020182>.
- [78] J.V. Pondick, J.M. Woods, J. Xing, Y. Zhou, J.J. Cha, Stepwise Sulfurization from MoO₃ to MoS₂ via Chemical Vapor Deposition, *ACS Appl. Nano Mater.* 1 (2018) 5655–5661. <https://doi.org/10.1021/acsanm.8b01266>.
- [79] A.M. de Jong, H.J. Borg, L.J. van IJendoorn, V.G.F.M. Soudant, V.H.J. de Beer, J.A.R. van Veen, J.W. Niemantsverdriet, Sulfidation mechanism by molybdenum catalysts supported on silica/silicon(100) model support studied by surface spectroscopy, 97 (1993) 6477–6483. <https://doi.org/10.1021/j100126a024>.
- [80] J. Theerthagiri, R.A. Senthil, M.H. Buraidah, J. Madhavan, A.K. Arof, Synthesis of α -Mo₂C by Carburization of α -MoO₃ Nanowires and Its Electrocatalytic Activity towards Tri-iodide

- Reduction for Dye-Sensitized Solar Cells, *J. Mater. Sci. Technol.* 32 (2016) 1339–1344. <https://doi.org/10.1016/j.jmst.2016.03.003>.
- [81] H. Sun, G. Li, J. Luo, M. Rao, Z. Peng, T. Jiang, Thermodynamics guided ultrafast and continuous preparation of Mo₂C nanocrystals for hydrogen evolution electrocatalysis, *Mater. Des.* 193 (2020) 108803. <https://doi.org/10.1016/j.matdes.2020.108803>.
- [82] A. Kurlov, X. Huang, E.B. Deeva, P.M. Abdala, A. Fedorov, C.R. Müller, Molybdenum carbide and oxycarbide from carbon-supported MoO₃ nanosheets: phase evolution and DRM catalytic activity assessed by TEM and *in situ* XANES/XRD methods, *Nanoscale*. 12 (2020) 13086–13094. <https://doi.org/10.1039/D0NR02908D>.
- [83] S. Cetinkaya, S. Eroglu, Thermodynamic analysis and synthesis of porous Mo₂C sponge by vapor-phase condensation and *in situ* carburization of MoO₃, *J. Alloys Compd.* 489 (2010) 36–41. <https://doi.org/10.1016/j.jallcom.2009.09.053>.
- [84] T. Xiao, A.P.E. York, K.S. Coleman, J.B. Claridge, J. Sloan, J. Chanrock, M.L.H. Green, Effect of carburising agent on the structure of molybdenum carbides, *J. Mater. Chem.* (2001) 3094–3098. <https://doi.org/doi-org.inc.bib.cnrs.fr/10.1039/B104011C>.
- [85] T. Xiao, A.P.E. York, V.C. Williams, H. Al-Megren, A. Hanif, X. Zhou, M.L.H. Green, Preparation of Molybdenum Carbides Using Butane and Their Catalytic Performance, *Chem. Mater.* 12 (2000) 3896–3905. <https://doi.org/10.1021/cm001157t>.
- [86] T. Mo, J. Xu, Y. Yang, Y. Li, Effect of carburization protocols on molybdenum carbide synthesis and study on its performance in CO hydrogenation, *Catal. Today*. 261 (2016) 101–115. <https://doi.org/10.1016/j.cattod.2015.07.014>.
- [87] L. Wang, Z.-L. Xue, A. Huang, F.-F. Wang, Mechanism and Kinetic Study of Reducing MoO₃ to MoO₂ with CO–15 vol % CO₂ Mixed Gases, *ACS Omega*. 4 (2019) 20036–20047. <https://doi.org/10.1021/acsomega.9b03171>.
- [88] M. Sun, J. Zhang, C. Cao, Q. Zhang, Y. Wang, H. Wan, Significant effect of acidity on catalytic behaviors of Cs-substituted polyoxometalates for oxidative dehydrogenation of propane, *Appl. Catal. Gen.* 349 (2008) 212–221. <https://doi.org/10.1016/j.apcata.2008.07.035>.
- [89] N. Kosinov, F.J.A.G. Coumans, G. Li, E. Uslamin, B. Mezari, A.S.G. Wijpkema, E.A. Pidko, E.J.M. Hensen, Stable Mo/HZSM-5 methane dehydroaromatization catalysts optimized for high-temperature calcination-regeneration, *J. Catal.* 346 (2017) 125–133. <https://doi.org/10.1016/j.jcat.2016.12.006>.
- [90] K.-G. Haw, J.-M. Goupil, J.-P. Gilson, N. Nesterenko, D. Minoux, J.-P. Dath, V. Valtchev, Embryonic ZSM-5 zeolites: zeolitic materials with superior catalytic activity in 1,3,5-triisopropylbenzene dealkylation, *New J. Chem.* 40 (2016) 4307–4313. <https://doi.org/10.1039/C5NJ03310A>.
- [91] A. Palčić, S.N. Jaén, D. Wu, M. Cai, C. Liu, E.A. Pidko, A.Y. Khodakov, V. Ordonsky, V. Valtchev, Embryonic zeolites for highly efficient synthesis of dimethyl ether from syngas, *Microporous Mesoporous Mater.* 322 (2021) 111138. <https://doi.org/10.1016/j.micromeso.2021.111138>.
- [92] M. Akouche, J.-P. Gilson, N. Nesterenko, S. Moldovan, D. Chateigner, H.E. Siblani, D. Minoux, J.-P. Dath, V. Valtchev, Synthesis of Embryonic Zeolites with Controlled Physicochemical Properties, *Chem. Mater.* 32 (2020) 2123–2132. <https://doi.org/10.1021/acs.chemmater.9b05258>.

- [93] Q. Lin, X. Bu, C. Mao, X. Zhao, K. Sasan, P. Feng, Mimicking High-Silica Zeolites: Highly Stable Germanium- and Tin-Rich Zeolite-Type Chalcogenides, *J. Am. Chem. Soc.* 137 (2015) 6184–6187. <https://doi.org/10.1021/jacs.5b03550>.
- [94] H. Pei, Li. Wang, An open framework chalcogenide supertetrahedral cluster as visible-light driven photocatalysts for selective degradation., *Cryst. Growth Des.* 19 (2019) 5716–5719. <https://doi.org/10.1021/acs.cgd.9b00685>.
- [95] H. Wang, H. Yang, W. Wang, C. Xue, Y. Zhang, M. Luo, D. Hu, J. Lin, D. Li, Tao. Wu, Assembly of supertetrahedral clusters into a Cu-In-S superlattice via an unprecedented vertex-edge connection mode., *CrystEngComm.* 19 (2017) 4709–4712. <https://doi.org/10.1039/C7CE00849J>.
- [96] V.V. Klepov, A.A. Berseneva, K.A. Pace, V. Kocovski, M. Sun, P. Qiu, H. Wang, F. Chen, T.M. Besmann, H. Loye, NaGaS₂: An Elusive Layered Compound with Dynamic Water Absorption and Wide-Ranging Ion-Exchange Properties, *Angew. Chem. Int. Ed.* 59 (2020) 10836–10841. <https://doi.org/10.1002/anie.202001203>.
- [97] D. Friedrich, M. Schlosser, R. Weihrich, A. Pfitzner, Polymorphism of CsGaS₂ – structural characterization of a new two-dimensional polymorph and study of the phase-transition kinetics, *Inorg. Chem. Front.* 4 (2017) 393–400. <https://doi.org/10.1039/C6QI00462H>.
- [98] J. Zhang, S. Zhu, B. Zhao, B. Chen, Z. He, A new method of synthesis on high-quality AgGaS₂ polycrystalline, *Curr. Appl. Phys.* 10 (2010) 544–547. <https://doi.org/10.1016/j.cap.2009.07.017>.
- [99] J. Hu, Q. Lu, K. Tang, Y. Qian, J. Hu, Q. Lu, K. Tang, Y. Qian, G. Zhou, X. Liu, Solvothermal reaction route to nanocrystalline semiconductors AgMS₂ (M=Ga, In), *Chem. Commun.* (1999) 1093–1094. <https://doi.org/10.1039/a902218j>.
- [100] H. Wu, X. Li, Y. Cheng, Y. Xiao, Q. Wu, H. Lin, J. Xu, Y. Wang, The synergistic role of double vacancies within AgGaS₂ nanocrystals in carrier separation and transfer for efficient photocatalytic hydrogen evolution, *Catal. Sci. Technol.* 9 (2019) 5838–5844. <https://doi.org/10.1039/C9CY01488H>.
- [101] Infrared Nonlinear AgGaS₂, AgGaSe₂, GaSe, ZnGeP₂ (ZGP) Crystals, (n.d.). https://eksmaoptics.com/nonlinear-and-laser-crystals/nonlinear-crystals/infrared-nonlinear-aggas2-aggase2-gase-zngep2-crystals/?gclid=CjwKCAjwnZaVBhA6EiwAVVYv9BM1ZcJUmNGwYb05CDQKjdU6kbvNzjnM-6vUfKh3LiLzMmCtZ-WBSBoCOaYQAvD_BwE (accessed June 13, 2022).
- [102] A. Adhikary, H. Yaghoobnejad Asl, P. Sandineni, S. Balijapelly, S. Mohapatra, S. Khatua, S. Konar, N. Gerasimchuk, A.V. Chernatynskiy, A. Choudhury, Unusual Atmospheric Water Trapping and Water Induced Reversible Restacking of 2D Gallium Sulfide Layers in NaGaS₂ Formed by Supertetrahedral Building Unit, *Chem. Mater.* 32 (2020) 5589–5603. <https://doi.org/10.1021/acs.chemmater.0c00836>.
- [103] T.V. Vu, A.A. Lavrentyev, B.V. Gabrelian, D.D. Vo, P.D. Khang, L.I. Isaenko, S.I. Lobanov, A.F. Kurus', O.Y. Khyzhun, Optical and electronic properties of lithium thiogallate (LiGaS₂): experiment and theory, *RSC Adv.* 10 (2020) 26843–26852. <https://doi.org/10.1039/D0RA03280H>.
- [104] D. Hou, A.S. Nissimagoudar, Q. Bian, K. Wu, S. Pan, W. Li, Z. Yang, Prediction and Characterization of NaGaS₂, A High Thermal Conductivity Mid-Infrared Nonlinear Optical

- Material for High-Power Laser Frequency Conversion, *Inorg. Chem.* 58 (2019) 93–98. <https://doi.org/10.1021/acs.inorgchem.8b01174>.
- [105] S. Shim, W.B. Park, M. Kim, J. Lee, S.P. Singh, K.-S. Sohn, Cyan-Light-Emitting Chalcogenometallate Phosphor, $\text{KGaS}_2:\text{Eu}^{2+}$, for Phosphor-Converted White Light-Emitting Diodes, *Inorg. Chem.* 60 (2021) 6047–6056. <https://doi.org/10.1021/acs.inorgchem.1c00509>.
- [106] J.S. Jang, S.H. Choi, N. Shin, C. Yu, J.S. Lee, AgGaS₂-Type Photocatalysts for Hydrogen Production under Visible Light: Effects of Post-Synthetic H₂S Treatment., *ChemInform.* 38 (2007). <https://doi.org/10.1002/chin.200752018>.
- [107] D. Friedrich, M. Schlosser, A. Pfitzner, Synthesis and Structural Characterization of the layered Selenogallate RbGaSe_2 , *Z. Für Anorg. Allg. Chem.* 643 (2017) 1589–1592. <https://doi.org/10.1002/zaac.201700288>.
- [108] P. Lemoine, D. Carré, M. Guittard, Structure du sulfure de gallium et de potassium, KGaS_2 , *Acta Crystallogr. C.* 40 (1984) 910–912. <https://doi.org/10.1107/S0108270184006223>.
- [109] S. Balijapelly, P. Sandineni, A. Adhikary, N.N. Gerasimchuk, A.V. Chernatynskiy, A. Choudhury, Ternary alkali ion thiogallates, A_5GaS_4 (A = Li and Na), with isolated tetrahedral building units and their ionic conductivities, *Dalton Trans.* 50 (2021) 7372–7379. <https://doi.org/10.1039/D1DT00766A>.
- [110] A.P. Yelisseyev, M.K. Starikova, V.V. Korolev, L.I. Isaenko, S.I. Lobanov, Photoluminescence of lithium thiogallate LiGaS_2 , *J. Opt. Soc. Am. B.* 29 (2012) 1003. <https://doi.org/10.1364/JOSAB.29.001003>.

Chapter 3. Materials and methods

Part 1. Materials

1. Embryonic zeolites

Embryonic zeolites: aluminosilicate (EZ_{Al-Si}) (Si/Al=50) and all-silica (EZ_{Si}) were synthesized in LCS and applied as the carriers for presented catalytic systems (**Chapter 4, 5**).

Samples code: the oxide form of the samples prior to the catalytic test was denoted as EZ_{Si}-x%Me. The sulfide samples were denoted as EZ_{Si}-x%MeS₂, where Me is Mo or Co loading. The sample codes for spent catalysts were EZ_{Si}-5%(Mo₂C)_S or EZ_{Si}-5%(Mo₂C)_O, where index S is used for sulfide-derived, O-for oxide derived catalyst.

1.2 Preparation of EZ carriers

The initial gel composition for the aluminum-containing EZ_{Al-Si} synthesis was 9 TPAOH:0.25 Al₂O₃:25 SiO₂:430 H₂O:100 EtOH, and for all-silica EZ_{Si} it was 9 TPAOH:25 SiO₂:430 H₂O:100 EtOH where TPAOH stands for tetrapropylammonium hydroxide [1]. A typical preparation procedure includes mixing the TPAOH solution (20% in water, Alfa Aesar) with distilled water. In the case of synthesis of the embryonic zeolite Al₂(SO₄)·18H₂O (Sigma-Aldrich, 98%) was subsequently added and the system homogenized. Tetraethyl orthosilicate (TEOS Sigma-Aldrich, 98%) was then added, and the mixture stirred for 6 h leading to the formation of a water-clear homogeneous sol. The solid product was recovered by freeze-drying (-94 °C under vacuum). The recovered solids were ion-exchanged with 0.5 mol ammonium nitrate solution, washed with distilled water, and dried under air. A ZSM-5 (Si/Al=47.6) provided by Tosoh was used as a reference catalyst; results are presented in **Chapter 4**.

1.3 Metal loading and sulfidation

1.3.1 Wetness impregnation (WI)

Mo oxide-decorated catalysts were prepared by incipient wetness impregnation on the embryonic zeolite carriers. The samples were loaded with 5 wt. % of Mo and denoted as EZ_{Al-Si}-5%Mo, EZ_{Si}-5%Mo, and ZSM-5-5%Mo. (NH₄)₆Mo₇O₂₄·4H₂O (Alfa Aesar, 99%) was used as a source of Mo. After drying at room temperature, all samples were calcined at 550 °C for 5h in static air. In the case of various metal loading, the current metal amount was noted before wt. For instance,

EZ_{Si}-9%Mo. The Co or Mo-Co loaded samples were denoted EZ_{Si}-5%Co, EZ_{Si}-5%Co-1%Mo or EZ_{Si}-5%Co-1.7%Mo (**Chapter 4**). For Co-doped samples Co(NO₃)₂·6H₂O (Acros, 99%) was used as Co source.

Generally, EZ_{Al-Si}-x%Mo samples had bright green coloration, EZ_{Si}-x%Mo demonstrated pale blue or pale green coloration that could be changed in time due to the various humidity. The Mo-Co oxidic samples were pale purple, pure Co decorated EZ was dark brown.

1.3.2 Hydrothermal treatment (HT)

A hydrothermal treatment in a neutral environment was also used to load the active metal phase. A molybdenum salt solution was prepared by dissolving (NH₄)₆Mo₇O₂₄·4H₂O (PMA) salt in distilled water and added to EZ placed in a polypropylene bottle. The wt.% PMA added was calculated on the basis of a dry EZ. The obtained suspension was treated for 24h at 80 °C with stirring in an oil bath. After separation of the liquid phase, the solid was dried at room temperature for several hours and 1h at 60°C before calcination. The harvesting greenish powder was calcined at 550 °C for 5h under air atmosphere. Prepared samples were denoted EZ_{Si}-x%Mo-HT.

Unless otherwise noted, the samples were prepared by wetness impregnation. In the case of comparing different methods for obtaining oxide phases, a designation WI or HT was added to the sample code: EZ_{Si}-x%Mo-WI (**Chapter 4**) and EZ_{Si}-x%Mo-HT (**Chapter 5**).

1.3.4 Sulfurizing

Mo sulfidation was performed under an H₂S/H₂ gas flow (30 ml/min, 10 vol% H₂S). 300 mg of the pelletized sample (35/45 mesh) was loaded in a Pyrex reactor, first heated under an N₂ flow at 140 °C for 2 h, then at 350 °C (2,8 °C·min⁻¹ ramp rate) for 2h under an H₂S/H₂ flow, cooled down to 180 °C and finally under a flow of dry N₂ to room temperature and kept there for 3 h. The samples were denoted EZ_{Al-Si}-5%MoS₂, EZ_{Si}-5%MoS₂, ZSM-5-5%MoS₂ (Chapter 3), EZ_{Si}-5%MoS₂-WI/HT (**Chapter 5**). The cobalt or molybdenum-cobalt decorated samples were prepared by the same corresponding protocol and denoted similarly.

After sulfidation, all samples become black. The presence of dark-blue coloration indicated the not completed process.

2. Thiogallates synthesis

The synthesis of potassium thiogallate (KGaS₂) by a method developed in the framework of present study. The crystals of KGaS₂ were obtained via a solvothermal synthesis using Ga₂O₃ (99.99%, 50 mesh powder, Alfa Aesar), sulfur (≥ 99.5%, Sigma-Aldrich), and KNO₃ (≥ 99.0%, Sigma-Aldrich). Ethylenediamine (EDA) (≥ 99.5%, Fluka Analytical) and 1-2-(aminoethyl)piperazine (AEP) (98%, Alfa Aesar) were used as the solvent and the template, respectively. The solids were loaded at a molar ratio Ga₂O₃/S/KNO₃=1/25.5/2.3, followed by template (EDA or AEP) addition to their mixture. The resultant suspension was stirred at room temperature for 30 min. The formed brownish suspension was placed in stainless steel autoclave with a Teflon liner at 190 °C for 1-7 days under static conditions. The solid was recovered by filtration, washed with ethanol, and dried at 50 °C for 1 h in an air atmosphere.

All as-prepared samples were washed with EtOH at 350 °C, before the catalytic application was calcined under N₂ in the tubular oven. The results are presented in **Chapter 5**.

3. Characterization

3.1. Physicochemical characterization

3.1.1. X-Ray Diffraction

Powder X-ray diffraction (XRD) is the primary and basic technic for crystalline compounds in the harvested solid samples which are used for structure identification and characterization.

A crystal is an order structure with a precise position of each atom that could scatter X-ray waves. It leads to the production of a regular array of spherical waves. These waves compensate one another in most directions (destructive interference), but there is also constructive interference determined by Bragg's law:

$$n\lambda = 2d\sin\theta$$

Here, n-the diffraction order, θ is the glancing angle, λ -the wavelength, and d-"grating constant".

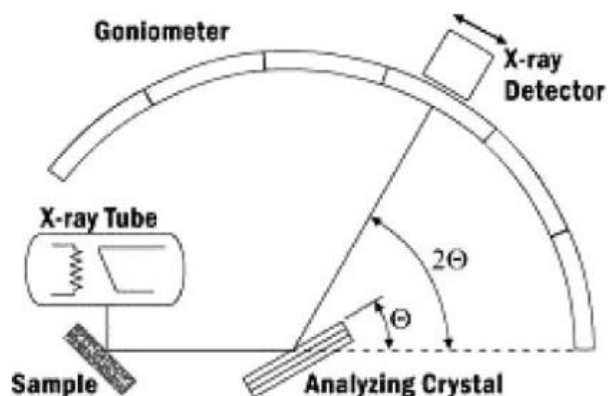


Fig.1-Principal scheme of a diffractometer system.

The typical principal scheme of the diffractometer is presented in **Fig.1**. Produced X-rays are generated by a cathode in the X-ray tube. After filtering, the monochromatic radiation is received. Then, afterward collimation, they are sent to the estimated sample. For X-ray signals the photon intensity is registered as a function to detector angle 2θ . The goniometer is used to maintain the angle and rotate the sample.

For crystalline samples, XRD is a powerful instrument to estimate and examine the type of presented compounds. A unit cell size and all atoms' positions create a quantity of structure 'fingerprints' of different solids. The XRD patterns represent their differences in various characteristic positions and relative intensities. Each pattern is unique to a specific structure.

Nanoscale crystalline materials could not be studied with the same efficiency as their larger counterparts, despite the importance of the XRD technique for solids. One of the limitations for them is crystallite size. The pattern resolution decreases with declining of the particle size. Especially, if it is about 5-10 nm [2]. For nanosized X-Ray amorphous embryonic zeolite, the XRD allowed controlling of the particle size for each formed phase after metal modification. However, under these limitations resolving the formed oxidic, sulfidic, or carbide phases was extremely difficult or impossible.

Experimental procedure. The powder X-ray diffraction (PXRD) patterns were recorded on a PANalytical X'Pert Pro diffractometer using the Cu $K\alpha$ radiation ($\lambda = 1.5418 \text{ \AA}$). The patterns were collected over a range of $4\text{--}50^\circ$ or $4\text{--}80^\circ$ 2θ with a time per step of 0.0167 s^{-1} using a 1° divergence slit.

3.1.2. Raman spectroscopy

Raman spectroscopy provides detailed information about chemical composition, phase purity, and molecular interactions. Raman analysis appertains to the category of vibrational spectroscopy. The monochromatic light produced by laser excites molecular vibration, and their interpretation is used afterward for understanding the results.

Raman, in contrast to infrared spectroscopy, is more effective for homonuclear bonds, secondary structural elements, and non-polar bonds. It is applied for differentiation between vibrations of C=C, C-C in organic compounds, and is more sensitive to metal-O, Me-S (without probe molecule presence), and carbides for inorganics.

In the framework of the study of Mo and Co modified embryonic zeolite, the important region for characterization was 300-1000 cm^{-1} . The Raman technique enabled the determination of the composition of the oxidic and sulfidic phases. However, the presence of carbon deposition after the catalytic test limited the carbide phase characterization. The diversity between coke and CNT [3] with defects could not be accurately assessed for carbon-contained materials. **Table 1** is presented the most important vibration mode values for various phases analyzed in this thesis.

Table 1. Raman vibrational modes of various phases related to the current study.

	Raman shift, cm^{-1}	Reference
<i>Oxidic phase (Mo)</i>		
$\alpha\text{-MoO}_3$	990, 821, 671	[3]
$\text{Mo}_7\text{O}_{24}^{6-}$	956, 900, 860, 360	[4]
<i>Sulfidic phase</i>		
2H- MoS_2	403, 370	[5,6]
<i>Oxidic phase (Mo-Co)</i>		
Co_3O_4	197, 484, 523, 62, 691	[7]
CoO_x	189, 466, 517, 658	[7]
<i>Sulfidic phase</i>		
CoS	676, 517, 475	[8]
CoS_2	393, 292	[8]
<i>Carbide phase</i>		
Mo_2C	143, 170, 213, 235, 652	[9]
Carbon nanotubes (CNT)	1300–1400, 1584, 2600–2800	[10]

Experimental procedure. The Raman spectra were acquired with a green laser at 532 nm (Jobin Yvon Labram 300 confocal Raman spectrometer coupled to a microscope and CCD detector). Spectra were recorded at ambient conditions in the range between 100 and 1200 cm^{-1} for oxides, sulfides, and carriers and from 1000 -1800 cm^{-1} for carbides.

3.1.3. Fourier transformed infrared spectroscopy

Fourier-transformed infrared spectroscopy (FTIR) is an essential tool for the analysis of zeolite-based catalysts. Various IR techniques are developed to study the composition and acidity of heterogeneous catalysts. For instance, a special place is taken by IR spectroscopy with probe molecules such as pyridine, CO, and NO. The monitoring of IR vibrations after their adsorption and desorption leads to a better understanding of the acid or active site concentration.

The analysis is carried out according to the following principle [11] (**Fig.2**). The infrared light traverses a wafer/pellet and interacts with it. The infrared radiation stimulates the movement of molecules and atomic bonds. These movement are described as rotational or vibrational.

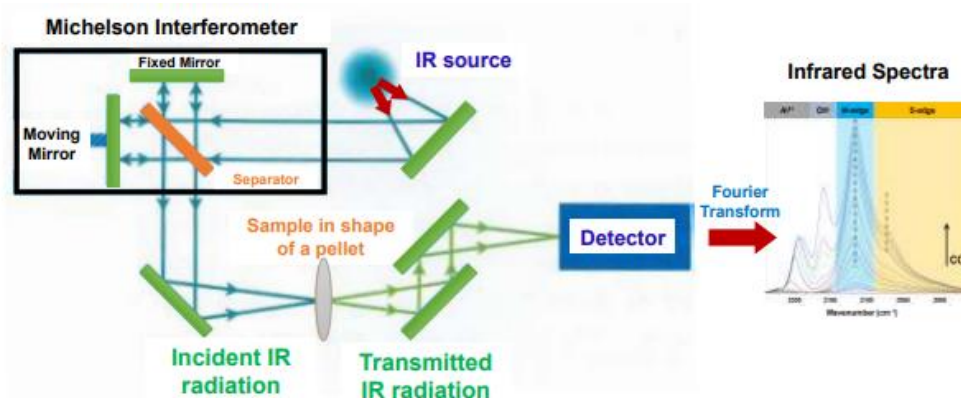


Fig.2- Basic concept of a typical Fourier-transform infrared spectrometer [12].

Experimental procedure. Before analysis, all samples should be formed as a self-supporting wafer with 2 cm^2 surface. Before introducing the probe molecule, all humidity or possible pollution should be removed by activation at 450 $^{\circ}\text{C}$ and under vacuum.

Pyridine was adsorbed to determine the concentration Brønsted and Lewis sites. At a pressure equal 1 torr it reached saturation. The wafer was heated from r.t till the end of

adsorption with 50 °C stepwise for 15 min at each step. After analysis, samples weight was normalized to 10 mg. For determination acidity were used bands' area at 1545 cm^{-1} (Brønsted, extinction coefficient $\epsilon=1.8 \text{ cm} \cdot \mu\text{mol}^{-1}$) and 1450 cm^{-1} (Lewis, extinction coefficient $\epsilon=1.5 \text{ cm} \cdot \mu\text{mol}^{-1}$) collected after desorption at 150 °C [1].

3.1.4. N₂ adsorption-desorption

The N₂ adsorption-desorption technique possesses a powerful potential for porous materials. The obtained data are used for isotherm model, calculations of surface area, pore volume, and pore size distribution.

Gas adsorption is based on the molecules' redistribution between the bulk phase and the surface layer. Adsorption refers to spontaneous processes occurring in heterogeneous systems at the interface. Depending on the mechanism of adsorption and the nature of the interaction between adsorbate molecules with the surface of the adsorbent, the shape of the isotherm is various. For a qualitative analysis of isotherms, the IUPAC classification of isotherms is used [13]. The character of the adsorption isotherm shape depends on the amount of the adsorbed gas under various pressure and fixed temperature (**Fig.3**).

Microporous materials are described by I type of isotherm (**Fig.3**).

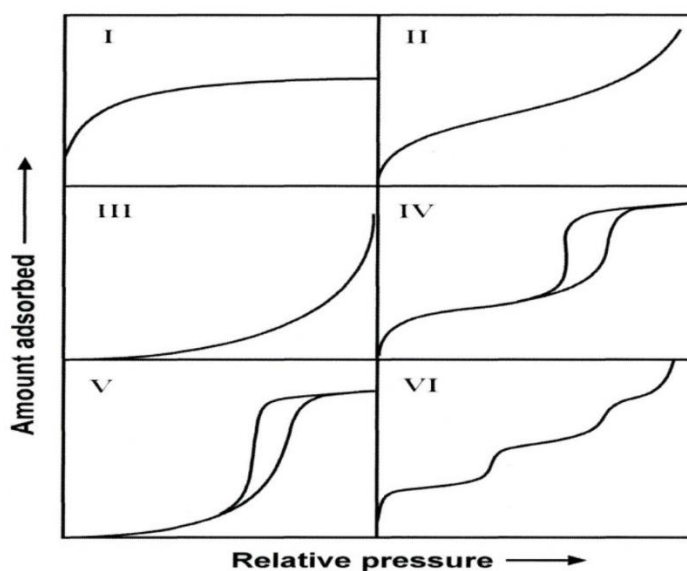


Fig.3- The standard IUPAC classification of adsorption isotherms.

In the course of the PhD thesis, N₂ adsorption-desorption analysis was applied for structure collapse prevention, controlling samples' repeatability. The effect on the surface area and total pore volume was studied for various modified states of the materials.

Experimental procedure. Nitrogen physisorption was performed on a Micromeritics ASAP 2020 surface area analyzer. The calcined samples were analyzed after degassing at 300 °C, and the ion exchange samples were degassed at 150 °C and analyzed after it. The total volume was calculated from the volume adsorbed at P/P₀= 0.95. The microporous volume (V_{mic} , cm³·g⁻¹) and the external surface area (S_{ext} , m²·g⁻¹) were obtained from the t-plot method based on the Harkins–Jura equation.

3.1.5. Scanning Electron Microscopy

Scanning Electron Microscopy (SEM) is a scanning process by an electron beam with producing a magnified image (resolution 1 mm to 1 nm or lower). The 'gun' produces the electron beams. These electrons dissipate as a variety of signals after interaction with solid surface. The obtained signals are presented by secondary electrons (SE, the most important for the accumulation of the SEM images), backscattered electrons (BSE), diffracted backscattered electrons (EBSD), and others (**Fig.4**). The SE and BSE are collected one by one signals are used for samples visualization [14,15].

This type of analysis has become essential for the study of the thiogallates. For the collected crystals, the crystallites' size, geometry, and purity were investigated by SEM. For the embryonic zeolite-based samples, by the SEM, the CNT formation was detected. However, for X-Ray amorphous materials, this analysis is not appropriate.

Experimental procedure. The scanning electron micrographs were collected on a MIRA-LMH (Tescan) SEM equipped with a field emission gun under an acceleration voltage of 30 kV. All samples before analysis were deposed to the carbon tape and treated under the metal (Pt/Pd) vapors.

3.1.6. Energy Dispersive X-ray Spectroscopy

The energy Dispersive X-ray Spectroscopy (EDX) [16] could assist during the SEM scanning for the identification of the elements. As it was shown in **Fig.4** the solid surface also emits X-rays.

The EDX detector used them to authenticate most elements by their own characteristic emissions. EDX is used for qualitative and quantitative characterization.

For the samples in the sulfidic form (sulfidic carbide precursors and thiogallates) the SEM/EDX is an alternative to quantitative spectroscopic analysis, allowing analysis of fresh samples in several minutes. For MoS₂ samples, during the quantification, an automatic peaks deconvolution was used to decrease the possible error. The Mo and S peaks are partially overlapped, but the deconvolution mode helps for higher accuracy.

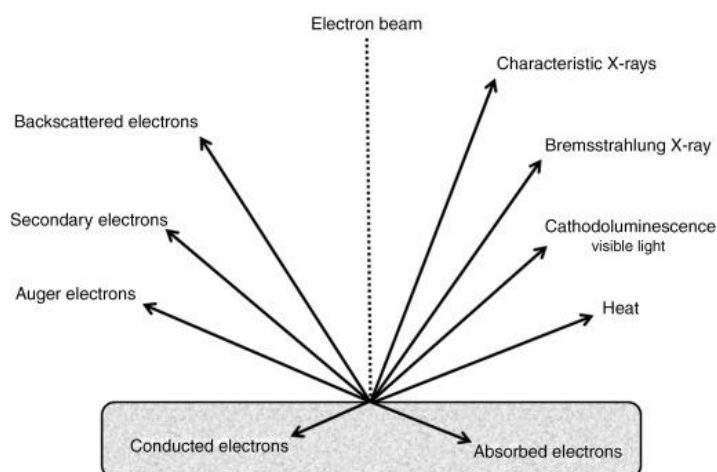


Fig.4- Main signals emitted due to the interaction between the electron beam and the sample [15].

The element distribution was investigated by EDS elemental mapping for applied catalysts.

Experimental procedure. The data was collected on a MIRA-LMH (Tescan) scanning electron microscope. The EDS analyses were obtained by the SDD detector using an accelerating voltage of 20.0 kV. An element map was collected for 10 minutes.

3.1.7. Thermogravimetry

For the characterization of the temperature-dependent properties, thermogravimetry has been applied. In the first place, this technique for presented materials allows clarifying the humidity content in the ion-exchange embryonic zeolite used for metal addition and for the determination of coke percent after catalytic tests. Thermogravimetry (TG) and differential

scanning calorimetry (DSC) is measured at the same time. For TGA, the reference and studied sample weight are measured independently. The sensitivity-calibrated independent drive coils perform it during the heating process. The difference between these masses is recorded as the signal. The TGA curve is represented by collected data: mass or percentage of the initial mass as a function of temperature or time. For DCS, the difference in temperature between the sample and reference material is collected as the function of the time. Phase transformations are interpreted from exothermic or endothermic changes. The enthalpy change is calculated from the area of the DTA peak. It does not depend on the material's heat capacity.

For a spent catalyst, the TGA is a rapid way to evaluate a total coke amount or an amount of soft and hard coke. Moreover, TGA characterization is useful for the detection of some interphase conversions. The untypical increase in the sample weigh curve could indicate it. Additionally, a comparison of the degradation temperature range could lead to distinctions among various carbon-based materials: *in situ* formed carbon nanotubes (CNT) or coke. For instance, amorphous carbon degradation starts at a temperature lower than 400 °C, for MWCNT this parameter is shifted to 500-600 °C [17].

Experimental procedure. TGA/DTA measurements of embryonic-based samples were carried out with a SETSYS SETARAM analyzer. The temperature was increased from 30 to 800 °C at 5 °C/min in reconstituted (80 % N₂ + 20 % O₂) dry air (40 mL/min).

3.1.8 Ultraviolet-visible spectroscopy

Ultraviolet-visible spectroscopy (UV-Vis) is used to determine the optical and electronic properties of solids and liquids. It is based on the measurement of the number of discrete wavelengths of UV or visible light that are absorbed by or transmitted through a sample in comparison to a reference or blank sample [18]. The VIS region is 400-800 nm, and UV is 200-400 nm.

In this study, this technique was applied to the thiogallates a additional proof of the detected phase formation.

Experimental procedure. Ultraviolet-visible (UV-Vis) spectra of the samples were recorded with Cary 4000 spectrometer from Varian. The spectrum acquisition was done between 800-200 nm with a speed of 300 nm/min.

3.1.9 Solid-state nuclear magnetic resonance

Solid-state nuclear magnetic resonance (NMR) is a spectroscopic atomic-level technique for determination of the chemical local environment, and 3D structure [19]. It is based on the nuclear spin interactions and the effects of magnetic fields on nuclear spins in solids.

Some elements' nuclei have a specific characteristic spin (I): integral spins ($I = 1, 2, 3$), half-integral spins ($I = 1/2, 3/2, 5/2$), or some of them could be without spin ($I = 0$, as ^{12}C , ^{16}O , ^{32}S). A spinning charge generates the magnetic field with a magnetic moment (μ). When magnetic nuclei are irradiated with an alternating magnetic field with a frequency corresponding to the difference between these discrete energy levels, the magnetic nuclei begin to move from one level to another while absorbing the energy of the alternating field. When exposed to an alternating magnetic field, the nucleus begins to interact with this field with an increase in amplitude, which can lead to resonance. At the moment of resonance, the absorption increases sharply and acquires a spectrum with a clearly defined maximum.

For structure determination of zeolite-like materials, ^{27}Al and ^{29}Si NMR are important research tools. The ^{29}Si NMR shifts are basically located in a range between +50 and -200 ppm [20], while the ^{27}Al shifts are between 0-90 ppm [21].

The ^{27}Al NMR is applied to understand the effect of the treatment conditions and metal impregnation. Also, the ratio between tetrahedral framework aluminum atoms, extra framework octahedral aluminum atom, and AlMoO_4 phase.

The ^{29}Si NMR could be applied for crystalline and for amorphous solids for the clarification of the local structure order. For the EZ-based structure, this analysis served as additional evidence of high short-range order [22]. The structure units' stability after 'soft' or 'extremal' treatment and the metal loading influence on the embryonic units are evidenced and explained based on this analysis.

All ^{27}Al NMR measurements were done with 4 mm (o.d.) zirconia rotors spun at 14 kHz on a Bruker Avance 400 spectrometer operating at 100.6 MHz. ^{29}Si MAS NMR was recorded on a Bruker Avance 500 spectrometer operating at 130.3 MHz. TMS was the reference for ^{29}Si , while a 1M $\text{Al}(\text{NO}_3)_3$ solution was used for ^{27}Al . The quantification of the spectra was done by integrating the peaks using Dmfit program.

3.1.10 Inductively coupled plasma atomic emission spectroscopy

Inductively coupled plasma atomic emission spectroscopy (ICP-MS) is a spectroscopy technique that used a high-temperature (7000 K) plasma to vaporize, dissociate, excite, and ionize the sample [23]. Obtained ions are extracted, and their signals are focused, analyzed by mass, and quantified.

The ICP-MS measurements were recorded using a 7900 ICP-MS from Agilent Technologies (to verify). Before analysis, all samples were dissolved in aqua regia and HF solutions for homogenization.

3.2 Catalytic test

The catalytic performance of the samples was evaluated in oxidative ethane dehydrogenation (ODH-CO₂). Several additional reverse water gas shift conversion (RWGS) tests were performed on the same samples to exclude the contribution of the methanation.

3.2.1 Oxidative ethane dehydrogenation and dry reforming of ethane (DRE)

300 mg or 150 mg of the 100–400 μm fractioned sample was used for all the CO₂ oxidative ethane dehydrogenation tests. Until the set temperature is reached, the loaded catalysts are treated at 300 °C under the reactants flow for 1-2 hours. The flow rate accuracy, verifying the accuracy of flow rates. Time is determined by the presence of traces of air in the gas stream. After, the set temperature reached a 10 or 3 °C/min ramp rate. The 10 °C/min ramp rate was applied by default as a standard mode. In the case of lowering it to 3 °C/min, this was indicated in the appropriate discussion. After the reaction, the reactor cooled down to room temperature under a dry N₂ flow.

The outlet gas flow is analyzed online with a gas chromatograph (Interscience Compact GC) equipped with three detectors: two TCDs and one FID. The TCD detector is a thermal conductivity detector. It's one of the most popular detectors for GS that could be applied for CO, CO₂, methane, C₂ fraction, N₂, and H₂. A gas examination is based on various changes in components' thermal conductivity. The FID detector is a flame ionization detector, it is applied for the evaluation of the alkane-alkene and aromatics mixture. The flame during the combustion

ionizes some gases, and it becomes more electrically conductive. This conductivity leads to the detector response.

A Molsieve 5A, Rt-QBond, Rtx-1 columns were used to separate light gases (H₂, N₂, CO, CO₂), light hydrocarbons (CH₄, C₂H₄, C₂H₆) and aromatics (from benzene till naphthalene), respectively. A Molsieve 5A is a capillary and porous-layer open-tubular (PLOT) column with aluminosilicate incorporation. It is applied for light hydrocarbons, oxygen, nitrogen, CO, and separation in a short time range. The second column, Rt-QBond is a nonpolar PLOT with polymer incorporation (divinylbenzene). It separates isomeric hydrocarbons from C₁ up to C₁₂, oxygenated compounds. Another nonpolar column is Rtx-1 with dimethylpolysiloxane. It is a general-purpose tool for light and heavy hydrocarbons, oil oxygenates, and S-contained compounds.

The standard tests were performed with a CO₂/C₂H₆/N₂= 49.5/36.5/14 (vol.%) mixture, in the temperature range 700-800 °C, at atmospheric pressure with a WHSV (C₂H₆) = 5.9 (g_{C₂H₆+CO₂}/g_{catalyst} × h). WHSV tuning was performed in the 5.9-17.7 h⁻¹ range with constant N₂ flow.

The assignment of the process to ODH-CO₂ or DRE was based on the CO₂/C₂H₆ conversion ratio and CO/C₂H₆ ratio.

Carbon dioxide (CO₂ conversion), ethane conversion (C₂ conversion), ethylene selectivity (C₂= selectivity), and CO selectivity (CO selectivity) were obtained as follows; the sum of the selectivities of the C₃-C₆ fraction and aromatics was labeled heavies:

$$\text{Conversion}(i) = \frac{C_{inlet}(i) - C_{outlet}(i)}{C_{inlet}(i)} \cdot 100\%$$

$$\text{Carbon selectivity}(i) = \frac{F(i)}{\sum F(i)} \cdot 100\%,$$

where $F(i)$ – mol of the C in the product compound

For samples tested under ODH-CO₂-route, it was considered that ethane is not converted to CO. Ethane is converted to ethylene, methane and heavies, CO₂ is fully converted to CO. Thus, for ODH-CO₂-route we consist carbon selectivity as selectivities to the C₂ products ($\sum F(i)$ is sum of ethylene, methane and heavies). CO is not taken to the calculation.

In **Chapter 5**, when ethane processing is going under mixed routes: ODH-CO₂ and DRE, ethane converts as to ethylene, as to CO. All selectivity calculations were performed with CO

($\sum F(i)$) is sum of ethylene, methane, heavies and CO). These selectivities are labelled as selectivity of all C-products.

In all the experiments, N₂ was used as an internal standard to measure conversion and establish mass balance. The mass balance in all the reported experiments was at least 99% (**Table 2**).

Table 2. Carbon Mass Balance, C₂H₆/CO₂ = 1/0.74, 700 °C.

Product	mol/min (average)
C2 inp	2.69E-02
C2 out	2.40E-02
C2=	2.65E-03
CH ₄	4.48E-05
C4	1.31E-06
C5	8.93E-07
C6	1.22E-06
Benzene	3.96E-06
Tolyene	1.22E-06
Xylenes	8.35E-08
CO ₂ inp	1.54E-02
CO ₂ out	1.45E-02
CO	1.12E-03
Input flow total	4.23E-02
Output flow total	4.23E-02
Delta, %	0.5

In order to reveal the catalytic impact of the catalyst on the reaction yield, a blank test without any catalyst was performed under the same operating conditions (same linear velocity, same temperature, same total and partial pressure of the reagents). In the blank test C2 (ethane), N₂, and CO₂ were co-fed in the same ratio as in the catalytic reaction (C₂H₆/CO₂/N₂=49.5/36.5/14 (vol.%)). The blank test without a catalyst is referred to in the text as a thermal process (“thermal”).

3.2.2 Techno-economical analysis

A techno-economic analysis was done using an Aspen Plus simulator to compare our results with those typical of ethane steam cracking from the literature. The simulations were for

a typical industrial-scale capacity of ethylene production of 1000 kt/year. The physical property databanks and methods as well as ASPEN Plus® models used, are summarized in **Table 3**.

Table 3. Aspen Plus model assumptions.

Aspen Plus databank and property method used in the process model	
Databank	APV90 PUR35, APV90 AQUEOUS, NISTV90 NIST-TRC
Stream class	CONVEN
Property method	NRTL, PR-BM
Unit operation model	
Reactor	Ryield, as per the carbon yield distribution in table 3
Heat exchanger	Heater
Flash/Separator	Flash2/Sep
Distillation column	DSTWU
Mixer	Mixer
Pressure change	Comp

3.2.3 Reverse water gas shift reaction

RWGS reaction was performed under the same protocol as described in 3.2.1. The gas mixture for this type of experiment was: CO₂/H₂/N₂= 49.5/36.5/14 (vol.%), in the temperature range 700-800 °C. The WHSV's choice depends on what mass of catalyst was used in most experiments with ethane for the corresponded experiments.

Conclusions

The summary of analysis techniques is presented in **Table 4**. Presented methods were complementary and allowed to provide a piece of general information about samples during their all transformation.

Table 4. Applied characterization methods

Method	Purposes for EZ-based materials	Purposes for thiogalates
X-Ray Diffraction	Study of the carbide formation and its following oxidation to oxides. Study of the formation of bulkier clusters	Crystallinity, phase purity verification.
Raman	Phase confirmation, C-based materials characterization.	
FTIR spectroscopy	Study of the carriers' acidity.	
N ₂ adsorption-desorption	Surface area, pore size, pore volume evaluation.	Surface area, pore size, pore volume evaluation.
Scanning electronic microscopy	CNT indication.	Morphology and size of the crystal.
Energy Dispersive X-ray Spectroscopy	Element distribution uniformity evaluation. Quantitative analysis.	Quantitative analysis.
Thermogravimetry	Refinement of the content of pure embryonic zeolite without moisture and traces of the template before Me addition. Coke content characterization. Coke-carbide diversification.	
Ultraviolet-visible spectroscopy		Structure verification.
Solid-state nuclear magnetic resonance	Understanding the local order in solids.	

References

- [1] Synthesis of Embryonic Zeolites with Controlled Physicochemical Properties | Chemistry of Materials, (n.d.). <https://pubs.acs.org/doi/10.1021/acs.chemmater.9b05258> (accessed August 23, 2021).
- [2] C.F. Holder, R.E. Schaak, Tutorial on Powder X-ray Diffraction for Characterizing Nanoscale Materials, *ACS Nano*. 13 (2019) 7359–7365. <https://doi.org/10.1021/acs.nano.9b05157>.
- [3] S.-H. Lee, M.J. Seong, C.E. Tracy, A. Mascarenhas, J.R. Pitts, S.K. Deb, Raman spectroscopic studies of electrochromic α -MoO₃ thin films, *Solid State Ion*. 147 (2002) 129–133. [https://doi.org/10.1016/S0167-2738\(01\)01035-9](https://doi.org/10.1016/S0167-2738(01)01035-9).
- [4] E. Dominguez Garcia, J. Chen, E. Oliviero, L. Oliviero, F. Maugé, New insight into the support effect on HDS catalysts: evidence for the role of Mo-support interaction on the MoS₂ slab morphology, *Appl. Catal. B Environ*. 260 (2020) 117975. <https://doi.org/10.1016/j.apcatb.2019.117975>.
- [5] Y. Yao, K. Ao, P. Lv, Q. Wei, MoS₂ Coexisting in 1T and 2H Phases Synthesized by Common Hydrothermal Method for Hydrogen Evolution Reaction, *Nanomaterials*. 9 (2019) 844. <https://doi.org/10.3390/nano9060844>.
- [6] N.H. Attanayake, A.C. Thenuwara, A. Patra, Y.V. Aulin, T.M. Tran, H. Chakraborty, E. Borguet, M.L. Klein, J.P. Perdew, D.R. Strongin, Effect of Intercalated Metals on the Electrocatalytic Activity of 1T-MoS₂ for the Hydrogen Evolution Reaction, *ACS Energy Lett*. 3 (2018) 7–13. <https://doi.org/10.1021/acsenergylett.7b00865>.
- [7] J. Zhu, L. Huang, Y. Xiao, L. Shen, Q. Chen, W. Shi, Hydrogenated CoO_x nanowire@Ni(OH)₂ nanosheet core–shell nanostructures for high-performance asymmetric supercapacitors, *Nanoscale*. 6 (2014) 6772. <https://doi.org/10.1039/c4nr00771a>.
- [8] D. Ma, B. Hu, W. Wu, X. Liu, J. Zai, C. Shu, T. Tadesse Tsega, L. Chen, X. Qian, T.L. Liu, Highly active nanostructured CoS₂/CoS heterojunction electrocatalysts for aqueous polysulfide/iodide redox flow batteries, *Nat. Commun*. 10 (2019) 3367. <https://doi.org/10.1038/s41467-019-11176-y>.
- [9] T. Li, W. Luo, H. Kitadai, X. Wang, X. Ling, Probing the Domain Architecture in 2D α -Mo₂C via Polarized Raman Spectroscopy, *Adv. Mater*. 31 (2019) 1807160. <https://doi.org/10.1002/adma.201807160>.
- [10] A. Jorio, R. Saito, Raman spectroscopy for carbon nanotube applications, *J. Appl. Phys*. 129 (2021) 021102. <https://doi.org/10.1063/5.0030809>.
- [11] N.B. Colthup, Infrared Spectroscopy, in: *Encycl. Phys. Sci. Technol.*, Elsevier, 2003: pp. 793–816. <https://doi.org/10.1016/B0-12-227410-5/00340-9>.
- [12] L.A.Z. Sanchez, Supported metal disulfide (TMS) catalysts for ultra-deep HDS : coupling of IR spectroscopy and microscopy for a deeper insight into active sites, phdthesis, Normandie Université, 2019. <https://tel.archives-ouvertes.fr/tel-02872878> (accessed May 16, 2022).
- [13] Z. AlOthman, A Review: Fundamental Aspects of Silicate Mesoporous Materials, *Materials*. 5 (2012) 2874–2902. <https://doi.org/10.3390/ma5122874>.
- [14] Scanning Electron Microscopy (SEM), Techniques. (n.d.). https://serc.carleton.edu/research_education/geochemsheets/techniques/SEM.html (accessed May 9, 2022).

- [15] M. de Assumpção Pereira-da-Silva, F.A. Ferri, Scanning Electron Microscopy, in: Nanocharacterization Tech., Elsevier, 2017: pp. 1–35. <https://doi.org/10.1016/B978-0-323-49778-7.00001-1>.
- [16] A.V. Girão, G. Caputo, M.C. Ferro, Application of Scanning Electron Microscopy–Energy Dispersive X-Ray Spectroscopy (SEM-EDS), in: Compr. Anal. Chem., Elsevier, 2017: pp. 153–168. <https://doi.org/10.1016/bs.coac.2016.10.002>.
- [17] E.R. Edwards, E.F. Antunes, E.C. Botelho, M.R. Baldan, E.J. Corat, Evaluation of residual iron in carbon nanotubes purified by acid treatments, Appl. Surf. Sci. 258 (2011) 641–648. <https://doi.org/10.1016/j.apsusc.2011.07.032>.
- [18] Theory of UV-Visible Spectroscopy, JASCO Inc. (n.d.). <https://jascoinc.com/learning-center/theory/spectroscopy/uv-vis-spectroscopy/> (accessed May 9, 2022).
- [19] B. Reif, S.E. Ashbrook, L. Emsley, M. Hong, Solid-state NMR spectroscopy, Nat. Rev. Methods Primer. 1 (2021) 2. <https://doi.org/10.1038/s43586-020-00002-1>.
- [20] M. Laird, N. Herrmann, N. Ramsahye, C. Totée, C. Carcel, M. Unno, J.R. Bartlett, M. Wong Chi Man, Large Polyhedral Oligomeric Silsesquioxane Cages: The Isolation of Functionalized POSS with an Unprecedented Si₁₈O₂₇ Core, Angew. Chem. Int. Ed. 60 (2021) 3022–3027. <https://doi.org/10.1002/anie.202010458>.
- [21] M. Choi, K. Matsunaga, F. Oba, I. Tanaka, ²⁷Al NMR Chemical Shifts in Oxide Crystals: A First-Principles Study, J. Phys. Chem. C. 113 (2009) 3869–3873. <https://doi.org/10.1021/jp810484j>.
- [22] J. Sanz, NMR Techniques for the Study of Crystalline and Amorphous Solids, in: C.R.A. Catlow (Ed.), Defects Disord. Cryst. Amorph. Solids, Springer Netherlands, Dordrecht, 1994: pp. 157–188. https://doi.org/10.1007/978-94-011-1942-9_8.
- [23] D. Pröfrock, A. Prange, Inductively Coupled Plasma–Mass Spectrometry (ICP-MS) for Quantitative Analysis in Environmental and Life Sciences: A Review of Challenges, Solutions, and Trends, Appl. Spectrosc. 66 (2012) 843–868. <https://doi.org/10.1366/12-06681>.

**Chapter 4. A Low Carbon Route to
Ethylene: Ethane Oxidative
Dehydrogenation with CO₂ on
Embryonic Zeolite Supported Mo-
Carbide Catalyst**

1. Introduction

Ethylene is the largest-volume petrochemical building block, produced primarily by steam cracking of oil fractions [1]. In 2020, the worldwide ethylene production capacity was 201 million tons, with an expected increase to 263 million tons in 2030 [2,3]. Ethylene is used to produce a wide spectrum of products like plastics, fibers, and other chemicals in the packaging, transportation, and construction industries. Polyethylene is the single-largest outlet, accounting for about 60% of global ethylene consumption in 2020. Other major applications include the production of ethylene oxide, ethylene dichloride, and ethylbenzene.

Steam cracking of oil fractions is the major process currently used to produce ethylene; a smaller contribution comes from refinery processes such as fluid catalytic crackers and cokers. It is a mature and well-established technology, which operation is considered near-optimal considering constant incremental improvements of the technology over 80+ years [4,5], leading to a thermal efficiency of close to 95% [6]. However, cracking is a very endothermic reaction taking place at high temperatures. As a result, ethylene production via steam cracking consumes about 30 % of the energy used in the chemical industry. In particular, as ethylene production by steam cracking consumes roughly between 17-25 GT/ton of ethylene while releasing about 1.2 tons of CO₂ per ton of olefin produced [5]; it is with about 260 million tons of CO₂ emissions worldwide per year [6], one of the largest contributors to greenhouse gas emissions in the manufacturing sector. Alternative routes and feedstocks need to be explored and developed to foster sustainable development of olefins production. In the last decade, the ongoing shift to lighter hydrocarbons as steam cracking feedstock has prompted research and development of alternative on-purpose production routes to ethylene.

One of the options for sustainable ethylene production is the utilization of bio feedstock: either bioethanol or bio hydrocarbon fractions [7–9]. Bioethanol dehydration shows advantages in energy consumption and in capital investments relative to conventional steam cracking due to simpler product slate and lower reaction temperature. Until the mid-1940s, a significant portion of the ethylene produced industrially was produced from bioethanol. Afterward, steam cracking of hydrocarbons, because of their superior economies of scale and lower feedstock costs, became the main source of ethylene. Currently, with the significantly increased cost of natural gas and

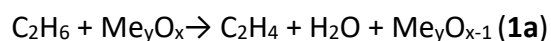
crude oil together with the need to reduce the carbon intensity of the petrochemical industry, the downstream industry is renewed interest in ethylene-from-ethanol plants [10,11]. So, this route will certainly regain importance but will not fulfill the total demand for ethylene due to the competition for feedstock with biofuel production. The availability of bio-naphtha and bio-propane as feedstock for olefins production is still limited [8]. The direct conversion of the cellulosic biomass or bio-oil remains an attractive route but mainly provides aromatic fractions [12–14].

So, a reduction of the carbon intensity of ethylene production routes remains a very important task for the petrochemical industry. The oxidative dehydrogenation of ethane (ODH) shows good prospects to reduce greenhouse gases emissions in comparison to a conventional ethane cracker due to a number of advantages, including lower energy consumption, simpler production slate, and potential elimination of the equilibrium limitations [15,16]. One of the main limitations remains the development of an efficient and stable high-temperature catalyst. Already in the early 80's, Phillips Petroleum proposed the first industrial Li-SnCl₂-MgO catalyst for oxidative dehydrogenation of ethane with oxygen [17]. This process did not require acetylene hydrogenation and had the potential to reduce energy consumption in an ethylene plant, allowing operations at 700 °C instead of 850 °C, and providing a higher ultimate yield of 90.5% ethylene [17] compared to the thermal process. However, as CO₂ was an important by-product, the economics were not better than state-of-the-art steam crackers. Recently, the topic regain attention the two semi-commercial oxidative dehydrogenation (ODH) of ethane processes were proposed [18–20]. Oxygen as an oxidant could be used in gaseous form or from catalysts' metal oxides lattice. One such promising on-purpose Oxidative Dehydrogenation of Ethane (ODH-E) technology is proposed by the Linde/Clariant partnership; a high selectivity to valuable products (ethylene and acetic acid) compared to steam cracking combined with a significant reduction potential of the CO₂ footprint is promised. Moreover, the reaction takes place under mild conditions, for instance, at atmospheric pressure and a maximum temperature of 400 °C [21]. However, as oxygen is applied as an oxidant, CO₂ is still present in products.

Another ODH option is based on chemical looping (CL-ODH). In CL-ODH, ethane is oxidatively dehydrogenated to ethylene and water following a typical Mars-van Krevelen

mechanism with the participation of lattice oxygen from the catalyst (Catalyst reduction, **Reaction 1a**) and its exothermic air regeneration (**Reaction 1b**), further providing heat to the endothermic ethane dehydrogenation to ethylene [22].

CL-ODH (Reduction)

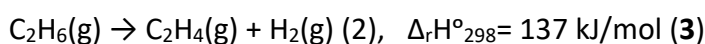
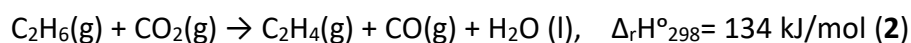


CL-ODH (Regeneration)



Other alternative approaches, currently at the laboratory scale, also using CO₂ as an oxidant to produce value-added ethylene from ethane, are proposed [18,19]. Such processes are attractive because they may lead to a CO₂-negative route in ethylene production. An additional benefit is a significant decrease in energy consumption downstream as hydrogen will not need purification: it will be consumed *in situ* to convert CO₂ to CO, and the latter could further be used to produce methanol, carbonylate, or hydroformylate other feedstocks. This approach is particularly interesting in view of recent trends to “electrify” steam crackers [23–25].

It is of note that the enthalpies of **reactions 2** and **3** ($\Delta_r H^\circ_{298}$) to produce ethylene from ethane by steam cracking and ODH-CO₂ are very close:



The ODH-CO₂ reaction was first reported by Lunsford *et al.* [26] using Li/MgO catalysts. Krylov *et al.* [27] investigated the ODH-CO₂ using several oxide catalysts (Fe₂O₃, Cr₂O₃, MnO₂) and multi-component systems. In the ODH-CO₂ at 800 °C, MnO₂-based catalysts exhibited high activities but low ethylene selectivity [28]. Nakagawa *et al.* [29] studied the dehydrogenation of C₂H₆ by CO₂ on several oxides and reported that gallium oxide (Ga₂O₃) is an effective catalyst for this reaction, giving a C₂H₄ yield of 18.6% with a selectivity of 94.5% at 650 °C.

Several reactions may occur in parallel, including oxidative dehydrogenation (ODH), reverse water-gas-shift (RWGS), or dry reforming of ethane (DRE) [30]. For the ODH-CO₂ reaction, precious metals, oxide [31], and carbide [30]-based catalysts are reported. Most of the catalytic systems are based on Pt [32], Ni [33], Co [34], Cr [35,36], Fe [37] oxides deposited on zeolite or oxide carriers.

Only a few Mo-based materials were reported for the ODH-CO₂ of ethane [38–40], but molybdenum carbide is well known as an alternative catalyst to noble metals in the highly selective reduction of CO₂ to CO [41,42]. Very high conversions of ethane in co-processing with CO₂ to produce hydrogen, ethylene, and CO were reported on the catalysts made up of the oxides of cobalt and molybdenum [38,43]. 58% conversion of ethane, 10.3% of CO₂, and 21.9% ethylene yield were achieved over these systems at 700 °C [43]. The conversion of ethane in these studies was higher relative to the thermodynamic equilibrium values of ethane conversion alone due to a significant contribution of secondary reactions [44]. Relatively low selectivity to ethylene showed a significant contribution to the direct ethane dehydrogenation resulting in high hydrogen production [38,43].

Mo₂C supported on SiO₂ was found to be an effective catalyst for the dehydrogenation of ethane to ethylene in the presence of CO₂. The selectivity to ethylene at 600–650 °C was 90–95% at an ethane conversion of 8–30%. At higher temperatures, dry reforming of ethane penalized ethylene yield. It is assumed that Mo oxycarbides formed in the reaction between CO₂ and Mo₂C play an important role in ethane activation [45]. Recently, a Mo-containing catalyst was reported for ODH-CO₂ but again only at 600 °C with relatively modest performance [30,46]. Oxygen from CO₂ appears crucial in cleaving the ethane C-C bond, increasing ethylene production. The addition of a Fe promoter accelerated the formation of surface oxygen species and stabilized them from reduction by ethane, leading to a shorter induction period, higher ethylene yield, and improved stability [30]. However, the main problems with Mo₂C catalysts operating at high temperatures remain the coking, sintering of the active Mo-species from cycle to cycle, and a significant contribution of the dry reforming reaction.

In order to design a stable at high-temperature Mo₂C-supported catalyst, we propose a different approach consisting of the utilization of MoS₂ precursors in place of oxides and embryonic zeolites (EZ) [47] as support in place of silica or alumina. An advantage of embryonic zeolites is the high surface area with a significant micropore volume resulting in the good dispersion and accessibility of all types of active sites [48]. In addition, EZ undergoes changes in surface area after the first heating cycle above 600 °C [48], which stabilizes the metal against sintering while keeping the active sites still accessible for the small molecules. After the first

surface reduction, substantially no changes occur with these materials upon consecutive thermal cycles. In this context, the embryonic zeolites as support could also stabilize the formed molybdenum carbide phase at high temperatures. However, the aging of EZ zeolite is a long process, what may lead to the agglomeration of MoO_x-oxides species before carburization. In order to limit the agglomeration of the MoO_x species during the first heating cycle, the idea was to use a MoS₂-precursor supported on EZ. Supported sulfides, especially MoS₂, are also known for CO₂ hydrogenation at high-pressure [49], but using MoS₂ for oxidative or non-oxidative ethane dehydrogenation was never reported to the best of our knowledge.

This work reports the preparation of a novel thermally stable Mo-based catalyst supported on EZ carriers from a MoS₂ – precursor (Mo₂C@EZ), its comprehensive characterization, and catalytic performances in ODH-CO₂ of ethane.

2. Results and discussion

2.1. Characterization of the catalysts

X-ray diffraction (XRD) indicates that on all samples, the embryonic carrier and the supported metal phase are X-ray amorphous (**Fig. 1a**), and EDX mapping indicates the metal is uniformly distributed on the EZ (**Fig. 1b**).

The 77-K nitrogen sorption-desorption isotherms of the EZ carriers (**Fig. 2a**) and the corresponding Mo- and MoS₂ – derivatives (**Fig. 2b**) show the Type IV isotherms. The mesoporosity is attributed to the intercrystallite spaces between the embryonic units and is observed in all the cases. After impregnation with the metal precursor, micropore volume drops from about 90 cm³/g to 70 cm³/g for the Al-containing embryonic sample (EZ_{Al-Si}) and to 45 cm³/g for all-silica embryos (EZ_{Si}). Mesopore volume decrease is observed only to a very small extent after each treatment for the catalysts. The results show that the metal precursors are mainly located in micropores of the supports.

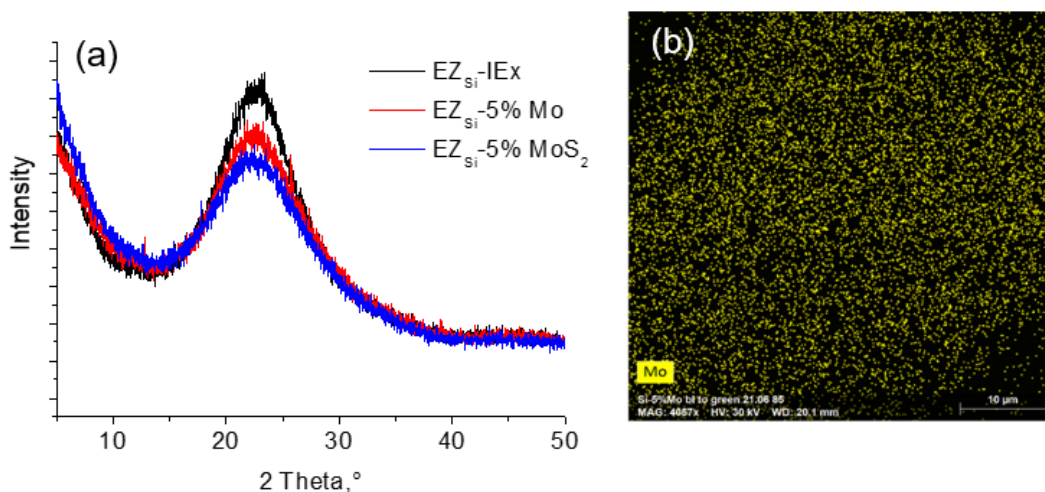


Fig. 1- a) XRD patterns of EZ_{Si}-IEx, EZ_{Si}-5%Mo, EZ_{Si}-5%MoS₂; b) EDX elemental mapping of Mo in EZ_{Si}-5%Mo.

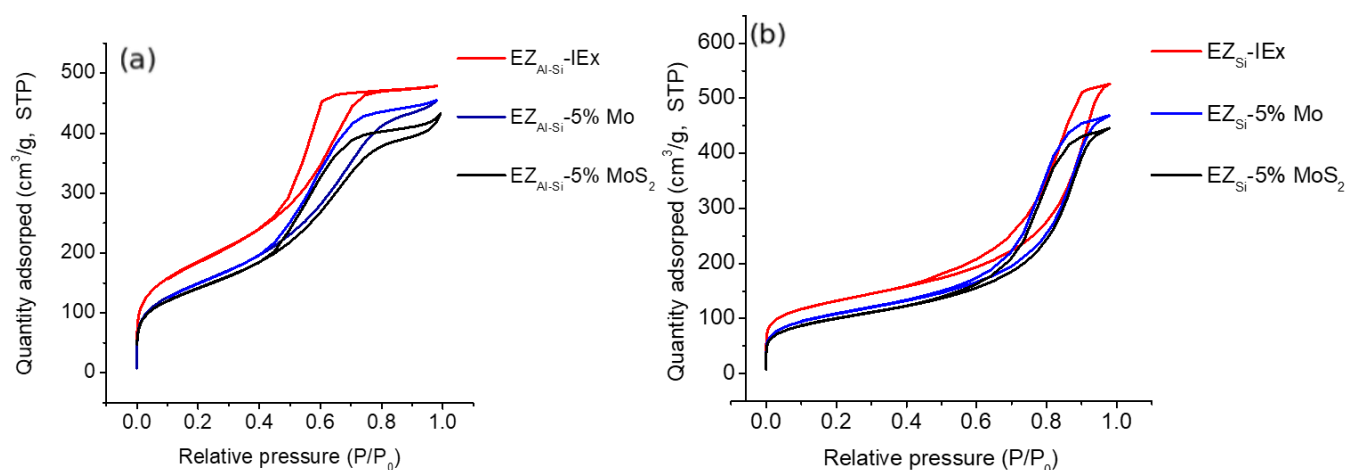


Fig. 2- N₂ adsorption-desorption isotherms: a)EZ_{Al-Si}-based; b)EZ_{Si}-based.

Raman spectroscopy was used to identify the nature of the metal phase in the EZ-supported catalysts (**Fig.3**). The spectrum of EZ_{Si}-5%Mo shows a wide band with two overlapping peaks at 990 cm⁻¹ and 950 cm⁻¹ and two better-resolved bands at 854 cm⁻¹ and 821 cm⁻¹. These bands can be assigned to polymolybdates (950 cm⁻¹, 854 cm⁻¹) [50] and α-MoO₃ (990 cm⁻¹, 821 cm⁻¹) [51] phases. In contrast, the EZ_{Al-Si}-5%Mo spectrum displays only an intense band at 990 cm⁻¹ with a shoulder at 854 cm⁻¹. We assume that both phases are also present on the latter catalyst, the polymolybdate phase being predominant.

The band at 480 cm⁻¹ [52] corresponds to Si-O stretching in the SiO₂ tetrahedra and is attributed to 4-membered rings often reported at 472 cm⁻¹ [53]. Both, EZ_{Si}-IEx and EZ_{Al-Si}-IEx display low-intensity bands around 970 and 1035 cm⁻¹. The 970 cm⁻¹ band is assigned to Si-O stretching vibrations in terminal Si-OH groups [54], while the 1035 cm⁻¹ band is characteristic for the stretching of alkyl chains of the protonated nitrogen atom of the organic template.

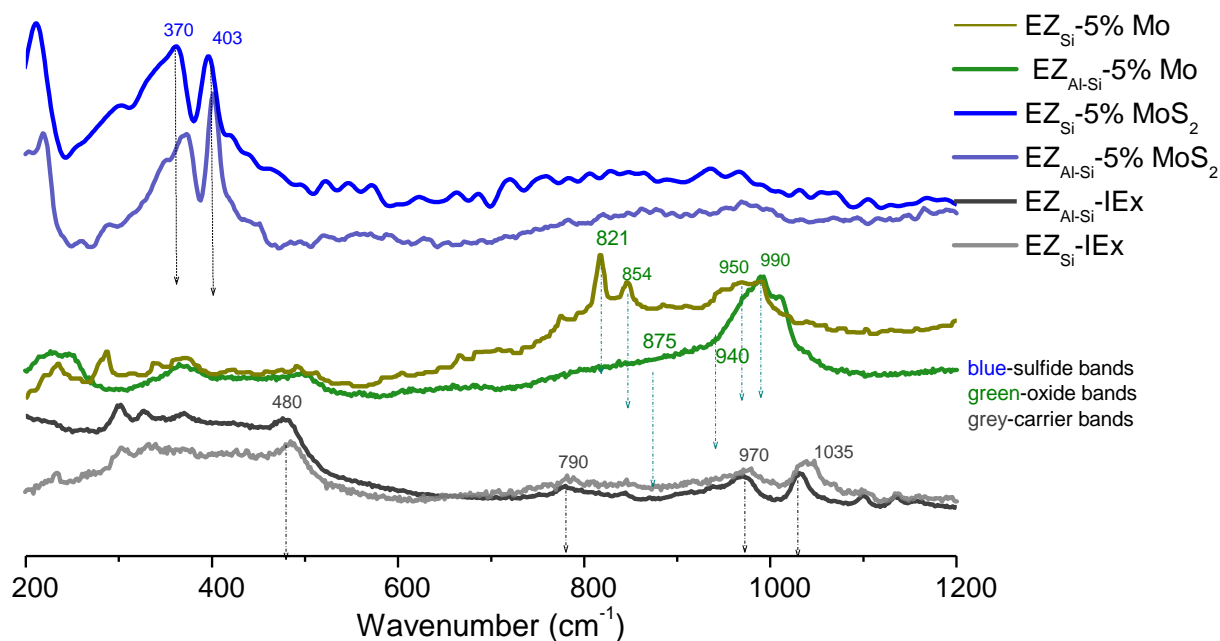


Fig. 3- Raman spectrum of EZ decorated with molybdenum oxide and sulfide phases.

The conversion of the oxide to the sulfide phase can also be monitored by Raman spectroscopy. Bands at 370 and 403 cm⁻¹ are attributed to 2H-MoS₂ phase [55,56]. The wideband with a maximum of about 230 cm⁻¹ is characteristic of silica tetrahedra in a bulk SiO₂ phase and remains unchanged after full oxide conversion.

The high-temperature stability of the catalyst carrier is studied by solid-state ²⁷Al and ²⁹Si NMR. The nature of the silicon environment in the parent all-silica EZ and Mo loaded after one calcination at 550 °C and subsequent calcination at 550 °C and at 700 °C is presented in **Fig. 4a**. All spectra display large peaks centered around -110 ppm, and the CP MAS spectrum exhibited a low resolved peak around -100 ppm. Only the parent contains a relatively large amount of Q³ species. Small amounts of Q² species (-97 ppm) can be observed in EZ_{Si}-IEx and EZ_{Si}-5%Mo-550.

All spectral deconvolutions are summarized in **Table 1**. They indicate that metal impregnation increases the number of Q⁴ units along with a full disappearance of the Q³ and Q²'s.

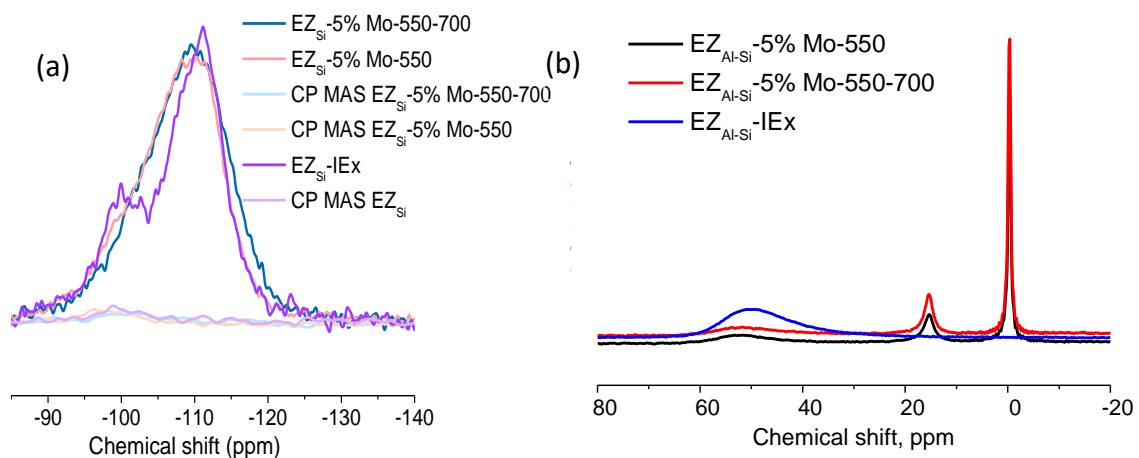


Fig. 4- Solid-state NMR analysis of the parent materials after ion exchange and Mo-loading: a) ²⁹Si NMR (1pulse) and CP MAS spectra; b) ²⁷Al NMR spectra.

Table 1. Relative percentage of Q², Q³, and Q⁴ silicon environments in EZ_{Si}-parents and calcined derivatives.

Sample	Q ²	Q ³	Q ⁴
EZ _{Si} -IEx	7	48	45
EZ _{Si} -5%Mo-550	2	22	76
EZ _{Si} -5%Mo-550-700	-	27	73

During the high-temperature treatment of silica-alumina embryos (550 °C or consecutive calcination at 550 and 700 °C) after Mo loading, Al is extracted from tetrahedral positions, **Fig.4b** while the parent, ion-exchanged with NH₄NO₃, does not contain any octahedral Al. The calcined samples loaded with 5 wt.% Mo, three types of aluminum coexist (Al^{IV}, Al^{VI}, and Al₂(MoO₄)₃), witnessing the catalysts alteration at high temperatures.

2.2. Catalytic performances

It is known that above 650 °C, MoO_x and MoS₂ species react with hydrocarbons to produce Mo₂C [57,58]. The mechanism of Mo₂C phase formation from MoS₂ in the presence of CH₄ and H₂

is described [59]. The carbide formation from MoO₃ under C₂H₆ and C₄H₁₀ is also reported [60]. In this contribution, the active Mo₂C phase is obtained *in situ* by subjecting the Mo-containing precursor in a contact with the mixture of C₂H₆/CO₂=1/0.74 at 700 °C. The hypothesis on Mo₂C formation is based on the typical profile of the TG curve [61] and on the observation of the characteristic bands for the graphitized carbon in Raman spectra synthesized with non-methane carburization agent [62, 63]. The TGA curves of the spent Mo₂C-containing samples demonstrated a slight weight increase up to 470 °C due to the oxidation reaction of Mo₂C to MoO₃ (**Fig.5**). However, the analysis of Mo₂C on the spent catalysts by Raman spectroscopy is a difficult task. The sulfidic form on the precursor is confirmed by the two bands around 370 and 403 cm⁻¹ (**Fig.6**), both bands are disappeared on the spent Mo₂C-containing samples. That shows the transformation of the MoS₂ -species to a different species. In addition, two new intense bands are detected in the region of C-C vibrations – (band D) at 1350 and (band G) 1600 cm⁻¹ on the sample after the reaction. They are typically attributed to the graphitized carbon (Fig.5) [64]. The intensity ratio of G (1580 cm⁻¹) to D (1350 cm⁻¹) band reflects the graphitization degree of catalysts [63]. These data suggest that the excess of methane led to the formation of graphitic carbon with the characteristic bands at 1350 and at 1600 cm⁻¹, which are also typically observed when the Mo₂C phase is formed [63]. The same covering of Mo-C bands was demonstrated under ethane, while XRD confirmed the formation of the claimed phase [63].

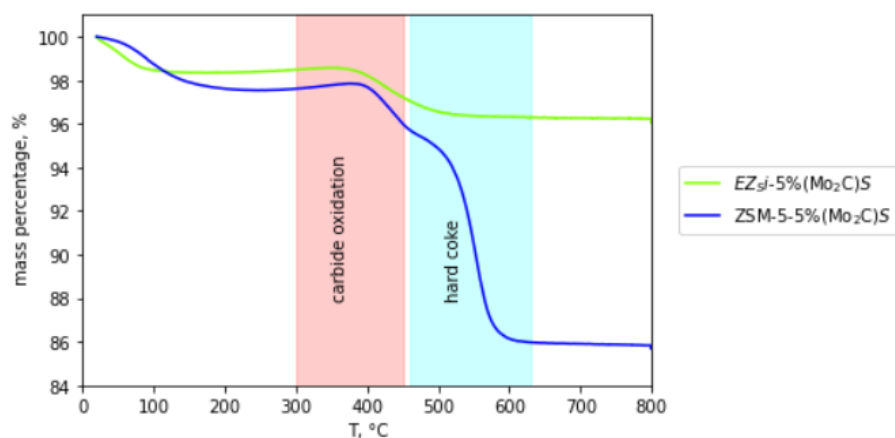


Fig. 5- Temperature programmed oxidation (30-800 °C at 5 °C/min in reconstituted (80 % N₂ + 20 % O₂) dry air (40 mL/min)) of carbonaceous residues on used EZSi-5%(Mo₂C)_S and ZSM-5-5%(Mo₂C)_S catalysts (P = 1 atm, C₂H₆/CO₂ = 1/0.74 WHSV = 5.9 h⁻¹, 700 °C, TOS-average 3-5 hours-on-stream).

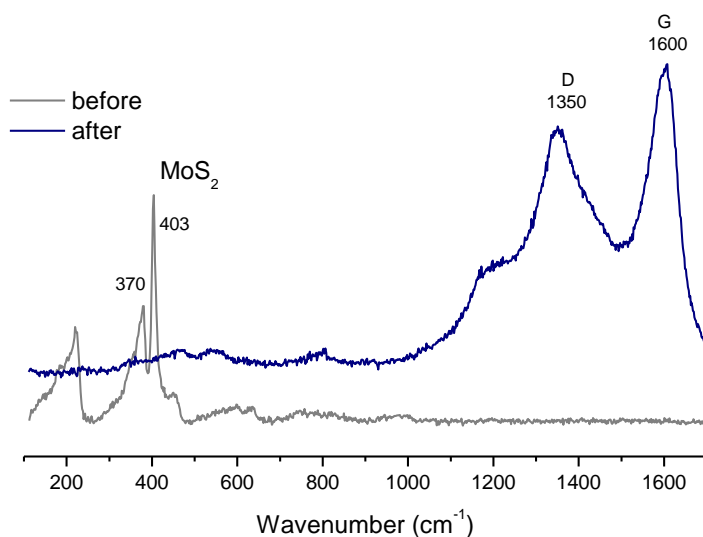


Fig. 6- Raman spectrum of embryonic zeolite decorated with sulfide phase before and after the catalytic test at 700 °C over EZ_{Si}-5%(Mo₂C)_S.

2.2.1. Impact of Mo-precursor:MoO_x vs MoS₂

Thermal, *i.e.*, the non-catalytic transformation of the mixture of ethane and CO₂ at 700 °C, results in ethane to ethylene conversion level, which is close to the thermodynamic equilibrium, with the ethylene selectivity above 95%. However, only a very limited CO₂ conversion is observed in this case. In contrast, the presence of the Mo₂C-supported on embryonic zeolite catalyst, formed from MoS₂ or MoO_x -precursors (EZ_{Si}-5%(Mo₂C)_S or EZ_{Si}-5%(Mo₂C)_O), leads to a significantly higher CO₂ conversion. One can also see that the EZ_{Si}-5%(Mo₂C)_S from MoS₂-precursor performs CO₂ transformation substantially without decreasing the ethane conversion in comparison with the one in the thermal process (**Fig.7a**). Moreover, the selectivity to ethylene is higher (**Fig.7b**). In contrast, the MoO_x-derived catalyst displays not only lower CO₂ conversion in comparison with the MoS₂-derived catalyst but also significant activity in ethylene hydrogenation back to ethane and very high methane selectivity (**Fig.7a**, **Fig.7b**).

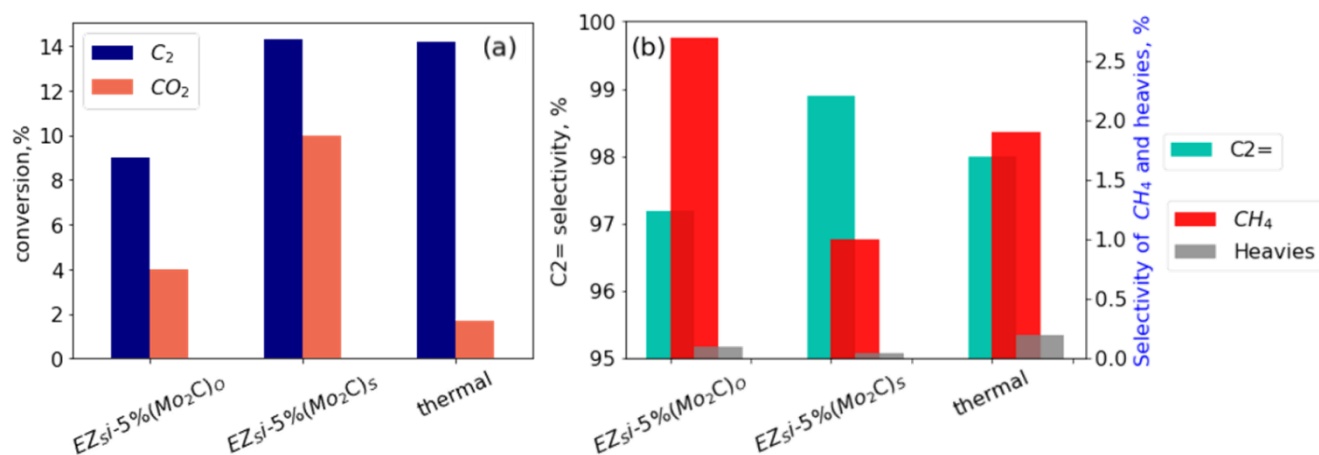


Fig. 7. ODH-CO₂ of ethane on EZSi-5%(Mo₂C)_O, EZSi-5%(Mo₂C)_S, and without catalyst: a) conversion of CO₂ and ethane; b) selectivities to the products (coke-free basis, 700 °C, C₂H₆/CO₂=1/0.74, WHSV = 5.9 h⁻¹, average level for 2-5 hours-on-stream).

The results summarized in **Table.2** show that only a few by-products are produced in all the cases. The MoS₂-derived catalyst also demonstrates higher stability than the MoO_x-derived one (**Fig.8**) and the highest selectivities in all cases. Therefore, the MoS₂-derived catalyst was selected for further investigation.

Table 2. Selectivities on the EZSi-5%(Mo₂C)_O and EZSi-5%(Mo₂C)_S catalysts vs thermal (no catalyst). (Coke-free basis, 700 °C, C₂H₆/CO₂=1/0.74, WHSV = 5.9 h⁻¹, TOS-average 2-5 hours-on-stream). (Ethane average conversion: thermal-14.3%, EZSi-5%(Mo₂C)_O-9%, EZSi-5%(Mo₂C)_S-14.2%; CO₂ average conversion: thermal-1.7%, EZSi-5%(Mo₂C)_O-4%, EZSi-5%(Mo₂C)_S-10%).

Sample	C ₂ =,%	CH ₄ ,%	CO,%	Heavies,%
Thermal	99.14	0.56	0.09	0.21
EZSi-5%(Mo ₂ C) _O	70.42	1.11	28.27	0.19
EZSi-5%(Mo ₂ C) _S	70.81	0.77	28.25	0.17

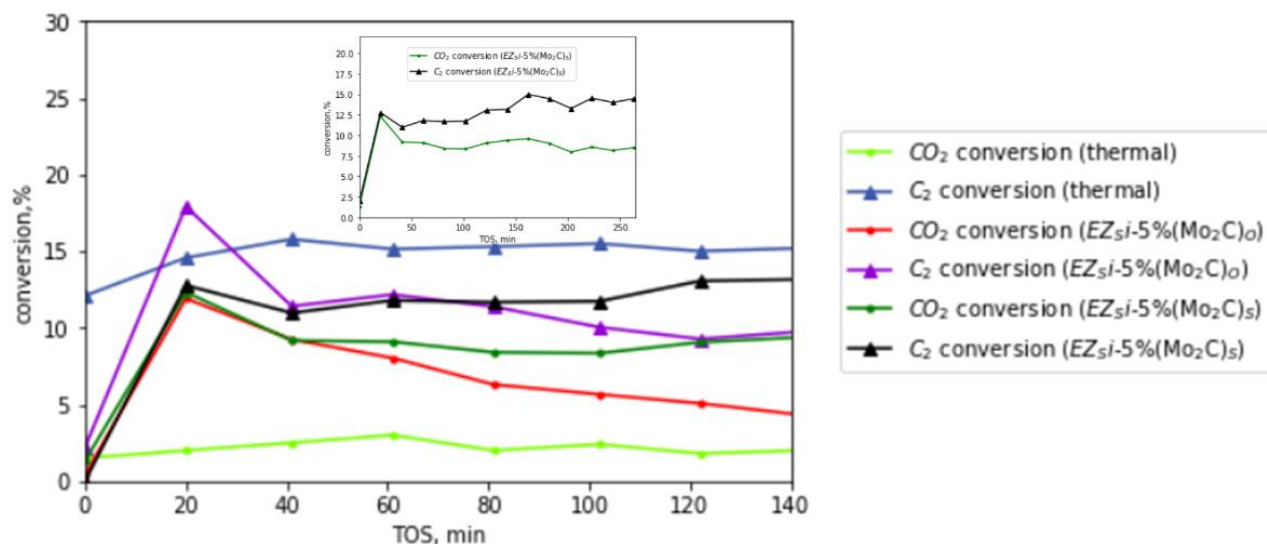


Fig. 8- Evolution of CO₂ and ethane (C₂) thermal and on EZ_{Si}-5%(Mo₂C)_o- and EZ_{Si}-5%(Mo₂C)_s catalysts conversion as a function of time on stream, TOS (T =700 °C, P = 1 atm, C₂H₆/CO₂ = 1/0.74, WHSV =5.9 h⁻¹).

2.2.2. Impact of the catalyst carrier

The performances in the ODH-CO₂ reaction of a series of MoS₂-derived catalysts supported on EZ of different acidity (EZ_{Si}-5%(Mo₂C)_s, EZ_{Al-Si}-5%(Mo₂C)_s, ZSM-5-5%(Mo₂C)_s) was evaluated. An embryonic zeolite and a conventional ZSM-5 with a crystal size of about 1 μm with a similar Si/Al atomic ratio were used for the study. The Bronsted acidity (BAS) and the Lewis acidity (LAS) of the supports before metal impregnation was assessed by FTIR adsorption of pyridine (**Table 3**). While the siliceous EZ_{Si} did not display any acidity, the Al-containing embryonic zeolite (EZ_{Al-Si}) showed some acid properties (**Table 3**). As expected, the highest acidity was measured on the zeolite carrier (ZSM-5).

Table 3. Acid site concentration on ZSM-5 and Al-containing embryonic zeolite measured by FTIR with pyridine probe molecule.

Sample	LAS, μmol/g	BAS, μmol/g
ZSM-5 (Si/Al=47)	235	1094
EZ _{Al-Si} (Si/Al=43)	57	185

The initial CO₂ and C₂H₆ conversions on the catalysts prepared on acidic support (ZSM-5-5%(Mo₂C)_s and EZ_{Al-Si}-5%(Mo₂C)_s) were significantly higher than on siliceous one (**Fig. 9**). In the case of ZSM-5-5%(Mo₂C)_s, ethane and CO₂ conversions were 37 % and 30 %, respectively. However, the main products were coke and aromatics, leading to rapid deactivation: down to 18% C₂H₆ and 13 % CO₂ after 140 min-on-stream, respectively. The result showed that the strong acidity of the support, which is typical for the zeolites is not desirable and leads to many side reactions.

The embryonic zeolite with a bulk Si/Al ratio close to the ZSM-5 one showed lower acid site concentration and, as a consequence, slower deactivation in comparison to the one on ZSM-5 support. It should be mentioned that the selectivity patterns on the Al-containing EZ_{Al-Si}-5%(Mo₂C)_s catalyst and on Al-free EZ_{Si}-5%(Mo₂C)_s catalysts looked more similar. One of the potential advantages of the Al-containing embryonic zeolite is the higher activity in CO₂ hydrogenation. However, higher coke content, in addition to higher methane selectivity, makes the acidity a disadvantage in this reaction (**Fig.5**).

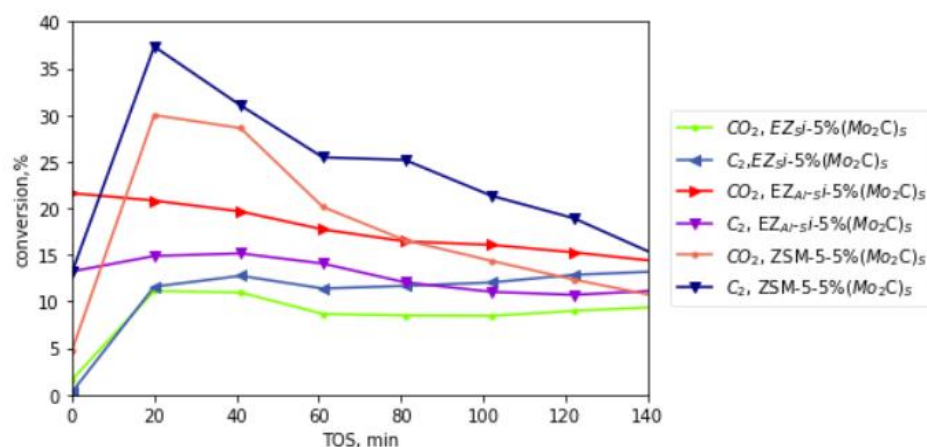


Fig. 9- Conversions of ethane (C₂) and CO₂ on EZ_{Si}-5%(Mo₂C)_s and EZ_{Al-Si}-5%(Mo₂C)_s and ZSM-5-5%(Mo₂C)_s as a function on time-on-stream (P = 1 atm, C₂H₆/CO₂ = 1/0.74, WHSV = 5.9 h⁻¹, TOS-average 3-5 hours-on-stream).

2.2.3. Performance of Al-free EZ_{Si}-5%(Mo₂C)_S in ODH-CO₂ of ethane

The selected purely silicious EZ_{Si} material showed to be advantageous in the dispersion and stabilization of Mo₂C while preventing deactivation due to coke formation (**Fig.10a**, **Fig.5**). Indeed, MoS₂-precursor supported on EZ extends the operating temperature range of Mo₂C catalysts compared to previously published results [36,37,45], in addition to suppressing the unwanted side reactions of methanation and dry-reforming. Remarkably, the selectivity to ethylene is even higher at the same process temperature than in the thermal process (**Fig.10b**).

The difference in ethane's catalytic and thermal conversion is due to some ethylene hydrogenation. Although the activity in ethylene hydrogenation is significantly lower on the catalyst than the one in CO₂ conversion to CO, it is worth comparing the selectivity at different temperatures at the same level of conversion.

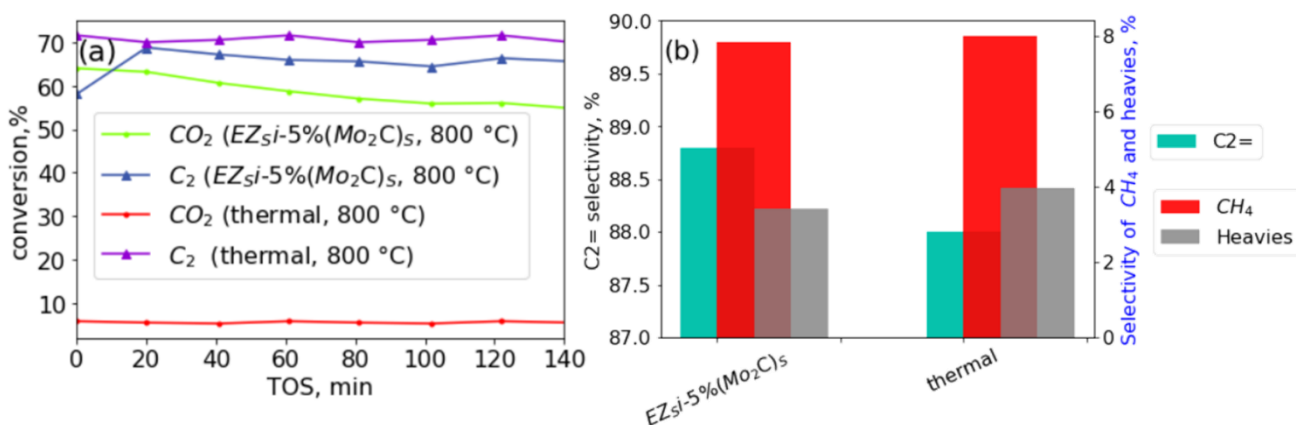


Fig. 10- ODH-CO₂ of ethane (C₂) on EZ_{Si}-5%(Mo₂C)_S and without catalyst: a) conversion of CO₂ and ethane as a function on time-on-stream; b) selectivities to the products (coke-free basis, T=800 °C, P = 1 atm, C₂H₆/CO₂ = 1/0.74, WHSV = 5.9 h⁻¹).

The selected catalyst (EZ_{Si}-5%(Mo₂C)_S) was tested at different temperatures, and its performance was compared with the thermal (without catalyst) transformation of ethane in the presence of CO₂ (**Fig. 11**). Due to some partial hydrogenation, the apparent ethane conversion level at the same temperature was slightly lower than in the thermal process (**Fig.12**). In order to compare the results, the data were linearly extrapolated to the same level of conversion. Three conversion levels of ethane were selected for the comparison: low conversion (15%), mid

conversion (40%), and high conversion (66%). In contrast to literature data on Mo₂C type of materials [45], one can see that at about 50% of CO₂ conversion to CO (reverse water-gas-shift reaction), the methanation and the dry reforming remained insignificant in the studied system (**Fig. 11**). In all cases, the ethylene selectivities in ODH-CO₂ of ethane were found very close between catalytic and non-catalytic processes. The impact on ethylene selectivity did not exceed 1-3 % for all the conversion levels of ethane, which could be considered insignificant. One can see that the presence of catalyst allows achieving a 50% conversion level of CO₂ without decreasing the selectivity to ethylene in comparison with the thermal process at the conversion of ethane up to 66% (**Fig.11**). All the results were obtained in the temperature range 700-800 °C what is the industrially relevant temperature range for the ethane cracking. A detailed comparison with the ethane cracking of the obtained catalyst performance is given below.

2.3. Techno-economical analysis of the ODH-CO₂ process based on an EZ_{Si}-5%(Mo₂C)_s catalyst

As mentioned in the introduction section, the emerging technological solutions aim to produce ethylene from ethane with lower CO₂ emissions in comparison with an ethane cracker.

The endothermic cracking of ethane (its C-C and C-H bonds require dissociation energies of 345 and 413 kJ/mol, respectively) to ethylene yield is limited. It requires high temperature and leads to the formation of side products such as aromatics and light gaseous. The catalytic conversion of ethane to ethylene in the presence of an oxidant is a potential solution to the problems outlined above. The ODH-E technology recently developed by Linde/Clariant reports CO₂ emissions reductions in the 23-32% range compared to conventional steam cracking [18]. The EcoCatalytic's CL-ODH technology also claims a 64% substantial reduction in CO₂ emissions compared to a state-of-the-art ethane steam cracker of the same capacity [22]. In the case of the state-of-the-art ethane steam cracker, hydrogen is the by-product. Such hydrogen could alternatively be used as a fuel for heat generation, leading to overall CO₂ emission reduction.

In such a broader context, oxidative dehydrogenation of ethane in the presence of CO₂ (ODH-CO₂) is a promising economical and environmental alternative. This process directly utilizes hydrogen to transform CO₂ into CO, which could further be used as the precursor for producing

valuable chemicals, mitigating CO₂ emissions while simultaneously achieving ethane dehydrogenation. This process can not only reduce CO₂ emission but also simplifies production slate processing by reducing CH₄ and heavies production.

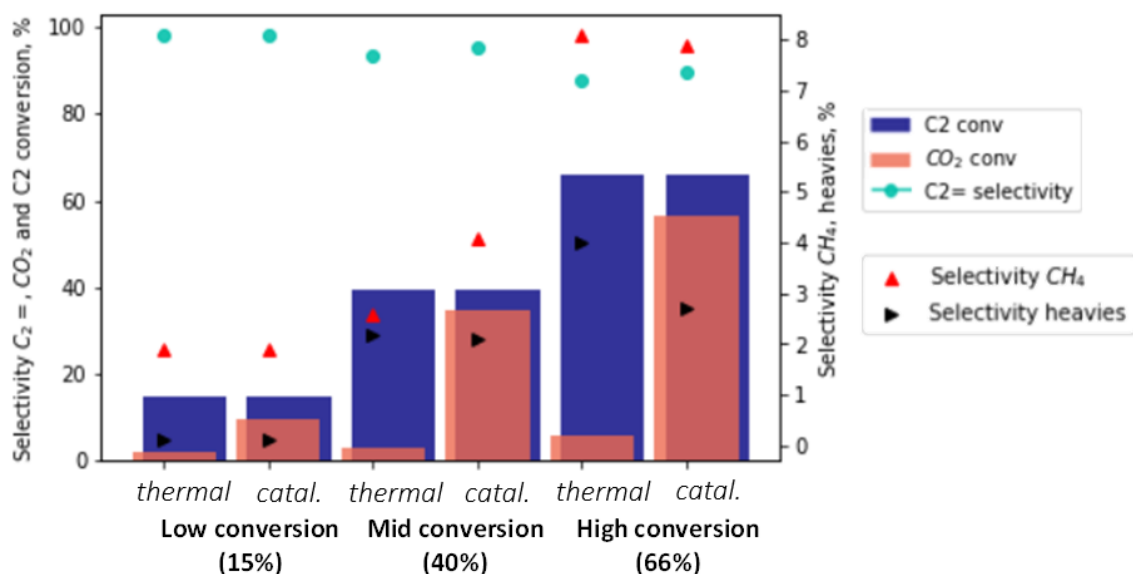


Fig.11-Comparison of catalytic (EZ_{Si}-5%(Mo₂C)_s) and thermal performances in ODH-CO₂ of ethane at the same conversion level of ethane (coke-free basis, C₂H₆/CO₂=1/0.74, WHSV = 5.9 h⁻¹).

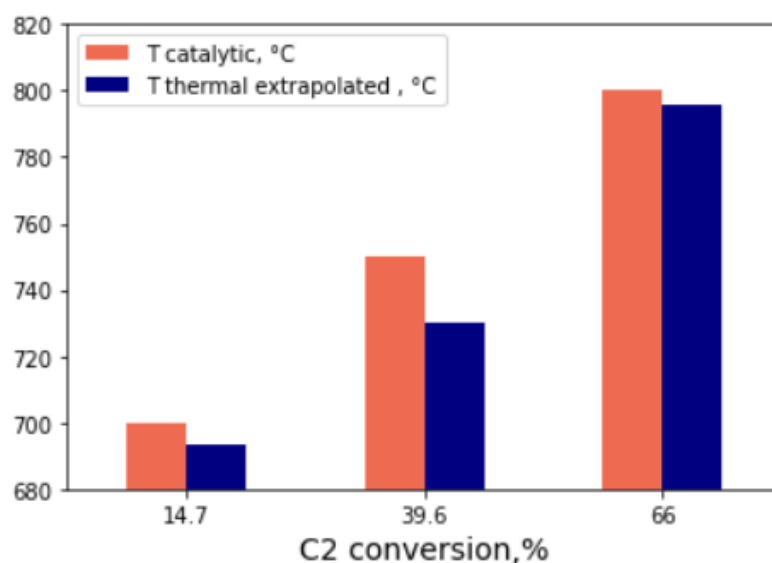


Fig. 12- Comparison of the theoretical temperatures which are required to achieve the same conversion level of ethane in catalytic and non-catalytic experiments.

Steam cracking proceeds through free-radical mechanisms [65], which are inherently characterized by a vast number of species and reactions leading to wide product distribution. Moreover, in steam crackers, acetylene is a by-product. Typically, the acceptable acetylene contaminant level in polymer grade ethylene products is 1 ppmv or lower. Since acetylene will fractionate with ethylene, it needs to be removed before the C₂ fractionation step. An acetylene hydrogenation unit is often required to convert it to ethylene. Consequently, the downstream processing of a steam cracker requires multiple separation units, as shown in **Fig. 13**.

In a state-of-the-art ethane steam cracker, the traces of CO are hydrogenated to CH₄, and the unconverted H₂ is of low grade with a significant amount of methane. The ODH-CO₂ process results in a significant amount of CO, significantly lower methane production, and some remaining hydrogen. So, the light end from an ODH-CO₂ could be considered as syngas, which after an adjustment of hydrogen content, could be directly suitable for MeOH synthesis.

ODH-CO₂ results in a lower amount of heavies, with almost no C₃ fraction and no acetylene, detected in the effluent of the reactor, as seen in **Table 4**. That is very interesting for separation and, eventually, for the energy balance. On the other hand, the C₂/CO₂ fraction should not be necessarily separated and could be recycled back to the reaction session as a feedstock (**Fig 13b**).

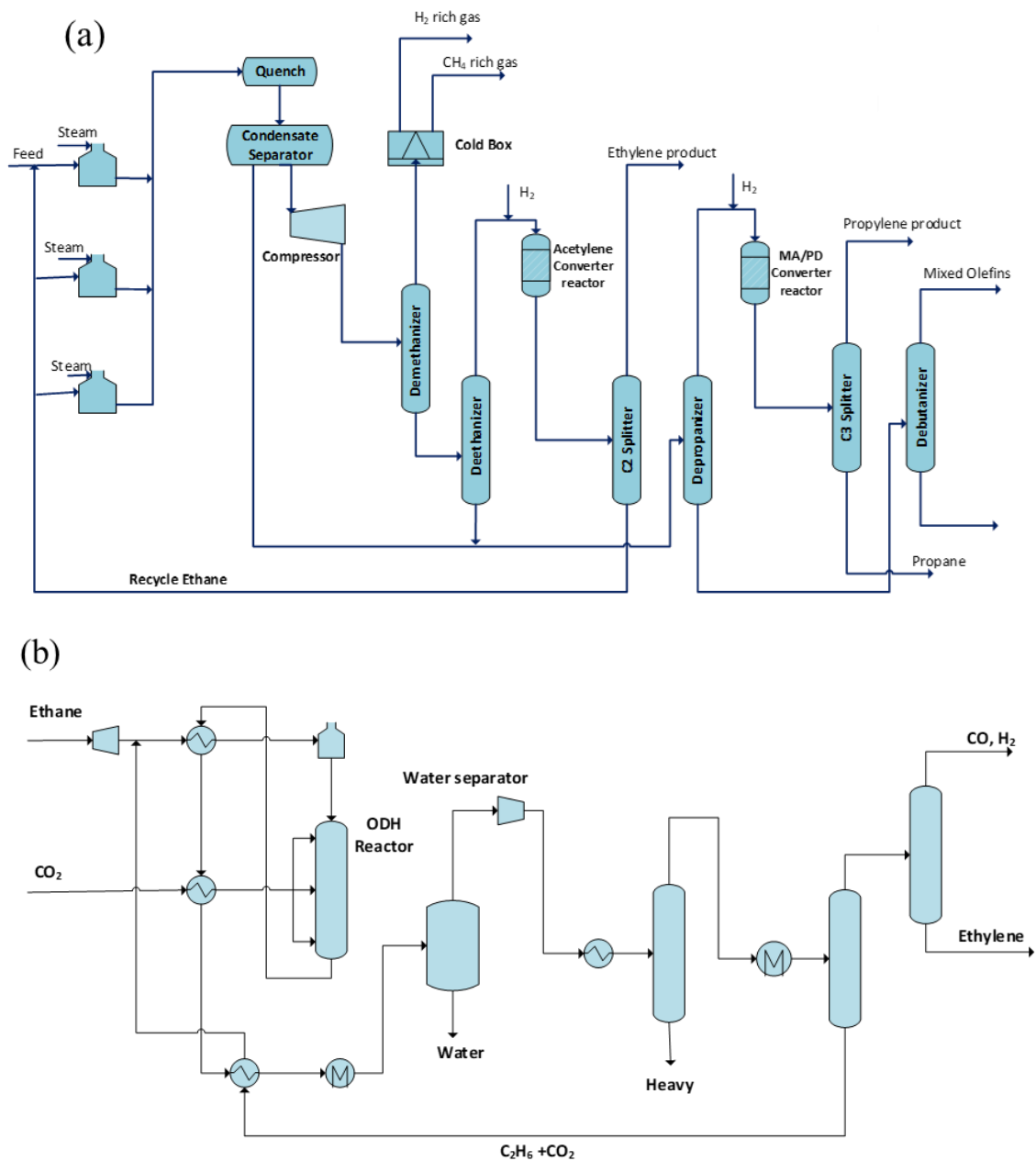


Fig. 13 Process scheme of steam cracking (a) and CO₂-assisted oxidative dehydrogenation (b).

Table 4. Comparison of steam cracking (SC) of ethane and ODH-CO₂.

	SC of ethane [66], 845 °C-outlet	ODH-CO ₂ [this work]
Ethane Conversion (%)	65.0	66.1
Carbon Yield (dry mol%)		
CO	0.00	27.34
CO ₂	0.00	20.71
CH ₄	3.40	4.81
C ₂ H ₂	0.50	0.00
C ₂ H ₄	56.10	27.29
C ₂ H ₆	35.00	19.46
C ₃ H ₆	1.20	0.00
C ₃ H ₈	0.10	0.00
C ₄ H ₆	2.10	0.00
C ₄ H ₈	0.20	0.00
C ₄ H ₁₀	0.20	0.30
C ₅ 's	0.60	0.10
Aromatics (benzene, toluene)	0.60	0.08

Figure 14 highlights the unit operations of a conventional SC plant and an ODH-CO₂ plant. The ODH-CO₂ requires 50% less unit operations compared to an ethane cracker. One can see that ODH-CO₂ may bring significant advantages in terms of investment costs and separation duties and therefore reduce CAPEX and OPEX.

Regarding energy consumption, ethylene production via steam cracking of ethane is very energy consuming: producing 1 ton of ethylene typically requires **21 GJ** of thermal energy (process energy consumed in pyrolysis and separation) and results in approximately **1.2 tons** of CO₂ emissions [5]. In our case, the simulation of the ODH-CO₂ process indicates an energy consumption of **17.4 GJ** of thermal energy to produce 1 ton of ethylene and **consumes 1,09 tons of CO₂**. Therefore, if ODH-CO₂ is implemented based on the current catalytic results, the reduction of CO₂ would be up 109% in comparison with the state-of-the-art ethane cracker making the technology CO₂ negative.

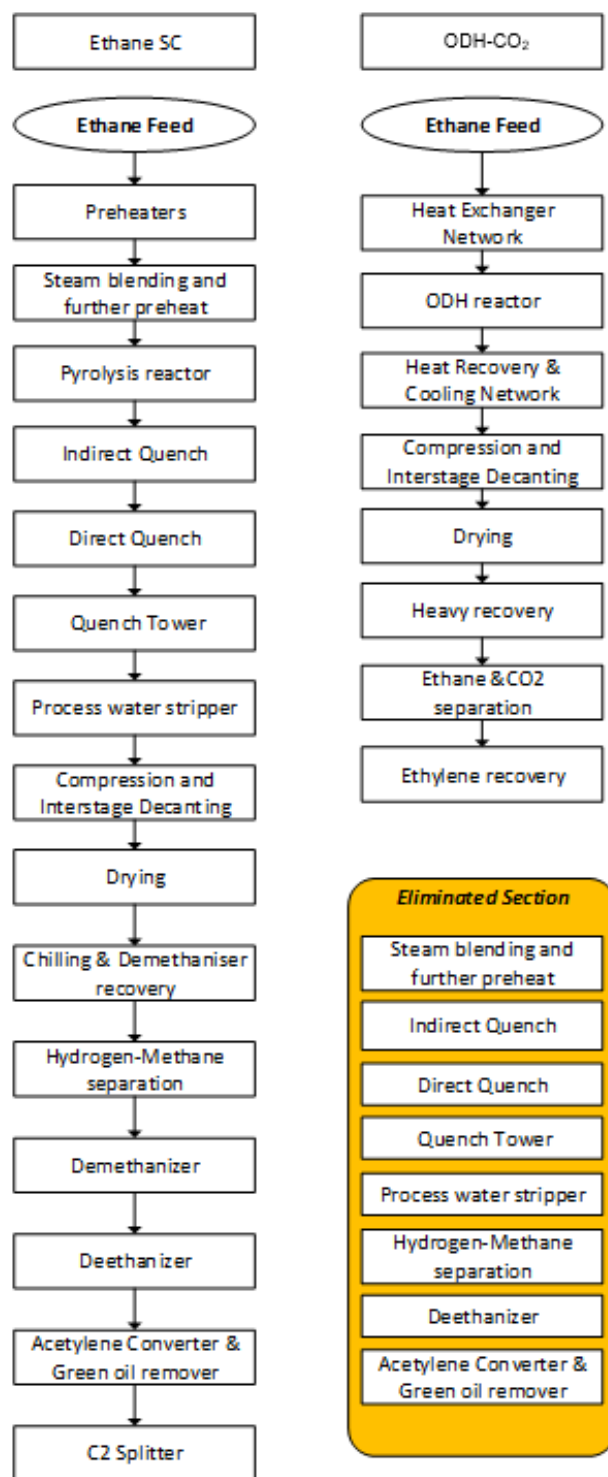


Fig. 14-Comparison in term of unit operations between SC and OHD-CO₂ ([55])

Conclusions

Embryonic zeolites show potential as supports for Mo₂C active species in ODH-CO₂. Supported metal sulfides proved to be efficient precursors of the Mo₂C active phase, which allows the designing of novel thermally stable and highly active catalysts for CO₂ hydrogenation in co-processing with alkenes. This “sulfide” route shows a clear advantage over the “oxide” one and requires only about 5 wt.% of Mo.

Although a detailed formation mechanism from MoS₂ to Mo₂C is still under investigation, it seems that MoS₂ supported on embryonic zeolites prevents sintering of the Mo-species during the carbide formation and results in a more active and stable catalyst for ODH-CO₂ of ethane. The latter allows operating at higher temperatures, avoiding dry reforming and methanation side reactions while producing more selectively ethylene.

The supported Mo₂C displays a good activity in CO₂ hydrogenation without negatively impacting the thermal C₂ conversion to ethylene at a conversion up to 66%. The resulting ODH-CO₂ process could lead to a potentially promising CO₂-negative technology with a much-reduced separation section due to a lower amount of heavies, no acetylene production, and better carbon efficiency. ODH-CO₂ thus brings significant advantages in terms of investment (CAPEX) and operating (OPEX) costs of a greener process.

References

- [1] T.D. Foley, S.W. Sohn, Ethylene production by steam cracking of normal paraffins, WO2002036716A1, 2002.
- [2] Ethylene production capacity globally 2025, Statista, Oxidative Dehydrogenation of Ethane Technology. <https://www.statista.com/statistics/1067372/global-ethylene-production-capacity/> 2021 (accessed September 22, 2021).
- [3] Ethylene Global Supply Demand Analytics Service, Wood Mackenzie. <https://www.woodmac.com/ja/news/editorial/ethylene-global-supply-demand-analytics-service/> 2018, (accessed September 27, 2021).
- [4] H. Zimmermann, R. Walzl, Ethylene, in: Wiley-VCH Verlag GmbH & Co. KGaA (Ed.), Ullmanns Encycl. Ind. Chem., Wiley-VCH Verlag GmbH & Co. KGaA, Weinheim, Germany, 2009: p. a10_045.pub3. https://doi.org/10.1002/14356007.a10_045.pub3.
- [5] T. Ren, M. Patel, K. Blok, Olefins from conventional and heavy feedstocks: Energy use in steam cracking and alternative processes, *Energy*. 31 (2006) 425–451. <https://doi.org/10.1016/j.energy.2005.04.001>.
- [6] Y. Yao, D.J. Graziano, M. Riddle, J. Cresko, E. Masanet, Understanding Variability To Reduce the Energy and GHG Footprints of U.S. Ethylene Production, *Environ. Sci. Technol.* 49 (2015) 14704–14716. <https://doi.org/10.1021/acs.est.5b03851>.
- [7] A. Mohsenzadeh, A. Zamani, M.J. Taherzadeh, Bioethylene Production from Ethanol: A Review and Techno-economical Evaluation, *ChemBioEng Rev.* 4 (2017) 75–91. <https://doi.org/10.1002/cben.201600025>.
- [8] E. Johnson, A carbon footprint of HVO biopropane, *Biofuels Bioprod. Biorefining.* 11 (2017) 887–896. <https://doi.org/10.1002/bbb.1796>.
- [9] W. Vermeiren, N.V. Gyseghem, Procédé de production de produits de craquage par vapocraquage de bio-naphtha et bio-propane obtenus à partir de mélanges complexes d'huiles et de graisses existant à l'état naturel, EP3059295A1, 2016.
- [10] F. Jamil, M. Aslam, A.H. Al-Muhtaseb, A. Bokhari, S. Rafiq, Z. Khan, A. Inayat, A. Ahmed, S. Hossain, M.S. Khurram, M.S. Abu Bakar, Greener and sustainable production of bioethylene from bioethanol: current status, opportunities and perspectives, *Rev. Chem. Eng.* 38 (2022) 185–207. <https://doi.org/10.1515/revce-2019-0026>.
- [11] M. Zhang, Y. Yu, Dehydration of Ethanol to Ethylene, *Ind. Eng. Chem. Res.* 52 (2013) 9505–9514. <https://doi.org/10.1021/ie401157c>.
- [12] A. Corma, G. Huber, L. Sauvanaud, P. Oconnor, Processing biomass-derived oxygenates in the oil refinery: Catalytic cracking (FCC) reaction pathways and role of catalyst, *J. Catal.* 247 (2007) 307–327. <https://doi.org/10.1016/j.jcat.2007.01.023>.
- [13] K.M.V. Geem, T. Dijkmans, J.M. Anthonykutty, S.P. Pyl, A. Harlin, G.B. Marin, Production of Bio-Ethylene: Alternatives for Green Chemicals and Polymers, (2013) 23.
- [14] Q. Yang, H. Zhou, P. Bartocci, F. Fantozzi, O. Mašek, F.A. Agblevor, Z. Wei, H. Yang, H. Chen, X. Lu, G. Chen, C. Zheng, C.P. Nielsen, M.B. McElroy, Prospective contributions of biomass pyrolysis to China's 2050 carbon reduction and renewable energy goals, *Nat. Commun.* 12 (2021) 1698. <https://doi.org/10.1038/s41467-021-21868-z>.

- [15] E. Heracleous, A. Lee, K. Wilson, A. Lemonidou, Investigation of Ni-based alumina-supported catalysts for the oxidative dehydrogenation of ethane to ethylene: structural characterization and reactivity studies, *J. Catal.* 231 (2005) 159–171. <https://doi.org/10.1016/j.jcat.2005.01.015>.
- [16] K. Chen, A. Khodakov, J. Yang, A.T. Bell, E. Iglesia, Isotopic Tracer and Kinetic Studies of Oxidative Dehydrogenation Pathways on Vanadium Oxide Catalysts, *J. Catal.* 186 (1999) 325–333. <https://doi.org/10.1006/jcat.1999.2510>.
- [17] J.H. Kolts, J.P. Guillory, Composition of matter and method of oxidative conversion of organic compounds therewith, US4672145A, 1987.
- [18] (124b) Oxidative Dehydrogenation of Ethane Technology, AIChE Academy. <https://www.aiche.org/academy/conferences/aiche-spring-meeting-and-global-congress-on-process-safety/2020/proceeding/paper/124b-oxidative-dehydrogenation-ethane-technology,2020> (accessed September 22, 2021).
- [19] C.A. Gärtner, A.C. van Veen, J.A. Lercher, Oxidative Dehydrogenation of Ethane: Common Principles and Mechanistic Aspects, *ChemCatChem.* 5 (2013) 3196–3217. <https://doi.org/10.1002/cctc.201200966>.
- [20] F. Cavani, N. Ballarini, A. Cericola, Oxidative dehydrogenation of ethane and propane: How far from commercial implementation?, *Catal. Today.* 127 (2007) 113–131. <https://doi.org/10.1016/j.cattod.2007.05.009>.
- [21] S.C. Arnold, A.M. Gaffney, R. Song, C.Y. Yeh, Process for producing ethylene via oxidative dehydrogenation (ODH) of ethane, US8519210B2, 2013.
- [22] L.M. Neal, V.P. Haribal, F. Li, Intensified Ethylene Production via Chemical Looping through an Exergetically Efficient Redox Scheme, *IScience.* 19 (2019) 894–904. <https://doi.org/10.1016/j.isci.2019.08.039>.
- [23] BASF, SABIC and Linde join forces to realize the world’s first electrically heated steam cracker furnace. <https://www.basf.com/global/en/who-we-are/sustainability/whats-new/sustainability-news/2021/basf-sabic-and-linde-join-forces-to-realize-wolds-first-electrically-heated-steam-cracker-furnace.html> (accessed March 9, 2022).
- [24] Petrochemical companies form Cracker of the Future Consortium and sign R&D agreement - Borealis, Borealisgroup. (2019). <https://www.borealisgroup.com/news/petrochemical-giants-form-consortium-cracker-of-the-future-and-sign-agreement> (accessed September 27, 2021).
- [25] Dow and Shell demonstrate progress in joint technology development for lower CO₂ emission crackers. <https://nl.dow.com/en-us/news/dow-and-shell-electrified-cracker-lowers-emissions.html> (accessed September 27, 2021).
- [26] D. Wang, M. Xu, C. Shi, J.H. Lunsford, Effect of carbon dioxide on the selectivities obtained during the partial oxidation of methane and ethane over Li⁺/MgO catalysts, *Catal. Lett.* 18 (1993) 323–328. <https://doi.org/10.1007/BF00765277>.
- [27] O.V. Krylov, A.Kh. Mamedov, S.R. Mirzabekova, The regularities in the interaction of alkanes with CO₂ on oxide catalysts, *Catal. Today.* 24 (1995) 371–375. [https://doi.org/10.1016/0920-5861\(95\)00061-J](https://doi.org/10.1016/0920-5861(95)00061-J).
- [28] O.V. Krylov, A.Kh. Mamedov, S.R. Mirzabekova, Oxidation of Hydrocarbons and Alcohols by Carbon Dioxide on Oxide Catalysts, *Ind. Eng. Chem. Res.* 34 (1995) 474–482. <https://doi.org/10.1021/ie00041a007>.

- [29] K. Nakagawa, M. Okamura, N. Ikenaga, T. Suzuki, K. Nakagawa, M. Okamura, T. Suzuki, T. Kobayashi, T. Kobayashi, Dehydrogenation of ethane over gallium oxide in the presence of carbon dioxide, *Chem. Commun.* (1998) 1025–1026. <https://doi.org/10.1039/a800184g>.
- [30] S. Yao, B. Yan, Z. Jiang, Z. Liu, Q. Wu, J.H. Lee, J.G. Chen, Combining CO₂ Reduction with Ethane Oxidative Dehydrogenation by Oxygen-Modification of Molybdenum Carbide, *ACS Catal.* 8 (2018) 5374–5381. <https://doi.org/10.1021/acscatal.8b00541>.
- [31] A. Talati, M. Haghghi, F. Rahmani, Oxidative dehydrogenation of ethane to ethylene by carbon dioxide over Cr/TiO₂–ZrO₂ nanocatalyst: Effect of active phase and support composition on catalytic properties and performance, *Adv. Powder Technol.* 27 (2016) 1195–1206. <https://doi.org/10.1016/j.apt.2016.04.003>.
- [32] M. Myint, B. Yan, J. Wan, S. Zhao, J.G. Chen, Reforming and oxidative dehydrogenation of ethane with CO₂ as a soft oxidant over bimetallic catalysts, *J. Catal.* 343 (2016) 168–177. <https://doi.org/10.1016/j.jcat.2016.02.004>.
- [33] A. Qiao, V.N. Kalevaru, J. Radnik, A. Martin, Oxidative dehydrogenation of ethane to ethylene over Ni–Nb–M–O catalysts: Effect of promoter metal and CO₂-admixture on the performance, *Catal. Today.* 264 (2016) 144–151. <https://doi.org/10.1016/j.cattod.2015.08.043>.
- [34] R. Koirala, O.V. Safonova, S.E. Pratsinis, A. Baiker, Effect of cobalt loading on structure and catalytic behavior of CoO_x/SiO₂ in CO₂-assisted dehydrogenation of ethane, *Appl. Catal. Gen.* 552 (2018) 77–85. <https://doi.org/10.1016/j.apcata.2017.12.025>.
- [35] P. Thirumala Bai, S. Srinath, K. Upendar, T.V. Sagar, N. Lingaiah, K.S. Rama Rao, P.S. Sai Prasad, Oxidative dehydrogenation of ethane with carbon dioxide over Cr₂O₃/SBA-15 catalysts: the influence of sulfate modification of the support, *Appl. Petrochem. Res.* 7 (2017) 107–118. <https://doi.org/10.1007/s13203-017-0182-5>.
- [36] T.A. Bugrova, V.V. Dutov, V.A. Svetlichnyi, V. Cortés Corberán, G.V. Mamontov, Oxidative dehydrogenation of ethane with CO₂ over CrO_x catalysts supported on Al₂O₃, ZrO₂, CeO₂ and Ce_xZr_{1-x}O₂, *Catal. Today.* 333 (2019) 71–80. <https://doi.org/10.1016/j.cattod.2018.04.047>.
- [37] S.A. Theofanidis, C. Loizidis, E. Heracleous, A.A. Lemonidou, CO₂-oxidative ethane dehydrogenation over highly efficient carbon-resistant Fe-catalysts, *J. Catal.* 388 (2020) 52–65. <https://doi.org/10.1016/j.jcat.2020.05.004>.
- [38] A. Bakhtyari, S. Zafarnak, H. Taghvaei, M.R. Rahimpour, A. Iulianelli, Simultaneous production of ethylene and hydrogen through carbon-dioxide-assisted conversion of ethane over cobalt-molybdenum catalysts, *J. CO₂ Util.* 47 (2021) 101499. <https://doi.org/10.1016/j.jcou.2021.101499>.
- [39] R.B. Watson, U.S. Ozkan, Mo Loading Effects over Mo/Si : Ti Catalysts in the Oxidative Dehydrogenation of Ethane, *J. Catal.* 208 (2002) 124–138. <https://doi.org/10.1006/jcat.2002.3548>.
- [40] E. Heracleous, A.F. Lee, I.A. Vasalos, A.A. Lemonidou, Surface Properties and Reactivity of Al₂O₃-Supported MoO₃ Catalysts in Ethane Oxidative Dehydrogenation, 88 (2003) 47–53. <https://doi.org/10.1023/A:1023534816277>.
- [41] X. Liu, C. Kunkel, P. Ramírez de la Piscina, N. Homs, F. Viñes, F. Illas, Effective and Highly Selective CO Generation from CO₂ Using a Polycrystalline α-Mo₂C Catalyst, *ACS Catal.* 7 (2017) 4323–4335. <https://doi.org/10.1021/acscatal.7b00735>.

- [42] M.D. Porosoff, X. Yang, J.A. Boscoboinik, J.G. Chen, Molybdenum Carbide as Alternative Catalysts to Precious Metals for Highly Selective Reduction of CO₂ to CO, *Angew. Chem. Int. Ed.* 53 (2014) 6705–6709. <https://doi.org/10.1002/anie.201404109>.
- [43] S. Zafarnak, A. Bakhtyari, H. Taghvaei, M.R. Rahimpour, A. Iulianelli, Conversion of ethane to ethylene and hydrogen by utilizing carbon dioxide: Screening catalysts, *Int. J. Hydrog. Energy.* 46 (2021) 19717–19730. <https://doi.org/10.1016/j.ijhydene.2020.09.150>.
- [44] V. Bikbaeva, O. Perez, N. Nesterenko, V. Valtchev, Ethane oxidative dehydrogenation with CO₂ on thiogallates, *Inorg. Chem. Front.* (2022) 10.1039/D2QI01630C. <https://doi.org/10.1039/D2QI01630C>.
- [45] F. Solymosi, R. Nemeth, The oxidative dehydrogenation of ethane with CO₂ over Mo₂C/SiO₂ catalyst, *Cat Lett.* 62 (1999) 197–200.
- [46] W. Marquart, M. Claeys, N. Fischer, Conversion of CO₂ and small alkanes to platform chemicals over Mo₂C-based catalysts, *Faraday Discuss.* 230 (2021) 68–86. <https://doi.org/10.1039/D0FD00138D>.
- [47] M. Akouche, J.-P. Gilson, N. Nesterenko, S. Moldovan, D. Chateigner, H.E. Siblani, D. Minoux, J.-P. Dath, V. Valtchev, Synthesis of Embryonic Zeolites with Controlled Physicochemical Properties, *Chem. Mater.* 32 (2020) 2123–2132. <https://doi.org/10.1021/acs.chemmater.9b05258>.
- [48] K.-G. Haw, J.-P. Gilson, N. Nesterenko, M. Akouche, H. El Siblani, J.-M. Goupil, B. Rigaud, D. Minoux, J.-P. Dath, V. Valtchev, Supported Embryonic Zeolites and their Use to Process Bulky Molecules, *ACS Catal.* 8 (2018) 8199–8212. <https://doi.org/10.1021/acscatal.8b01936>.
- [49] J. Hu, L. Yu, J. Deng, Y. Wang, K. Cheng, C. Ma, Q. Zhang, W. Wen, S. Yu, Y. Pan, J. Yang, H. Ma, F. Qi, Y. Wang, Y. Zheng, M. Chen, R. Huang, S. Zhang, Z. Zhao, J. Mao, X. Meng, Q. Ji, G. Hou, X. Han, X. Bao, Y. Wang, D. Deng, Sulfur vacancy-rich MoS₂ as a catalyst for the hydrogenation of CO₂ to methanol, *Nat. Catal.* 4 (2021) 242–250. <https://doi.org/10.1038/s41929-021-00584-3>.
- [50] E.D. Garcia, Effect of the support on the activity and morphology of hydrodesulfurization catalysts, phdthesis, Normandie Université, 2017. <https://tel.archives-ouvertes.fr/tel-01729093> (accessed August 23, 2022).
- [51] S.-H. Lee, M.J. Seong, C.E. Tracy, A. Mascarenhas, J.R. Pitts, S.K. Deb, Raman spectroscopic studies of electrochromic α-MoO₃ thin films, *Solid State Ion.* 147 (2002) 129–133. [https://doi.org/10.1016/S0167-2738\(01\)01035-9](https://doi.org/10.1016/S0167-2738(01)01035-9).
- [52] S.R. Stojkovic, B. Adnadjevic, Investigation of the NaA zeolite crystallization mechanism by i.r. spectroscopy, *Zeolites.* 8 (1988) 523–525. [https://doi.org/10.1016/S0144-2449\(88\)80230-6](https://doi.org/10.1016/S0144-2449(88)80230-6).
- [53] P.K. Dutta, D.C. Shieh, M. Puri, Correlation of framework Raman bands of zeolites with structure, *Zeolites.* 8 (1988) 306–309. [https://doi.org/10.1016/S0144-2449\(88\)80127-1](https://doi.org/10.1016/S0144-2449(88)80127-1).
- [54] A. Martinelli, S. Creci, S. Vavra, P.-A. Carlsson, M. Skoglundh, Local anisotropy in single crystals of zeotypes with the MFI framework structure evidenced by polarised Raman spectroscopy, *Phys. Chem. Chem. Phys.* 22 (2020) 1640–1654. <https://doi.org/10.1039/C9CP06199A>.

- [55] Y. Yao, K. Ao, P. Lv, Q. Wei, MoS₂ Coexisting in 1T and 2H Phases Synthesized by Common Hydrothermal Method for Hydrogen Evolution Reaction, *Nanomaterials*. 9 (2019). <https://doi.org/10.3390/nano9060844>.
- [56] N.H. Attanayake, A.C. Thenuwara, A. Patra, Y.V. Aulin, T.M. Tran, H. Chakraborty, E. Borguet, M.L. Klein, J.P. Perdew, D.R. Strongin, Effect of Intercalated Metals on the Electrocatalytic Activity of 1T-MoS₂ for the Hydrogen Evolution Reaction, *ACS Energy Lett.* 3 (2018) 7–13. <https://doi.org/10.1021/acscenergylett.7b00865>.
- [57] X. Li, J. Zhang, R. Wang, H. Huang, C. Xie, Z. Li, J. Li, C. Niu, In Situ Synthesis of Carbon Nanotube Hybrids with Alternate MoC and MoS₂ to Enhance the Electrochemical Activities of MoS₂, *Nano Lett.* 15 (2015) 5268–5272. <https://doi.org/10.1021/acs.nanolett.5b01579>.
- [58] Z. Zhao, F. Qin, S. Kasiraju, L. Xie, M.K. Alam, S. Chen, D. Wang, Z. Ren, Z. Wang, L.C. Grabow, J. Bao, Vertically Aligned MoS₂/Mo₂C hybrid Nanosheets Grown on Carbon Paper for Efficient Electrocatalytic Hydrogen Evolution. *ACS Catalysis*, 7 (2017). 7312–7318. <https://doi-org.inc.bib.cnrs.fr/10.1021/acscatal.7b02885>
- [59] J. Jeon, Y. Park, S. Choi, J. Lee, S.S. Lim, B.H. Lee, Y.J. Song, J.H. Cho, Y.H. Jang, S. Lee, Epitaxial Synthesis of Molybdenum Carbide and Formation of a Mo₂C/MoS₂ Hybrid Structure *via* Chemical Conversion of Molybdenum Disulfide, *ACS Nano*. 12 (2018) 338–346. <https://doi.org/10.1021/acsnano.7b06417>.
- [60] T. Xiao, A.P.E. York, K.S. Coleman, J.B. Claridge, J. Sloan, J. Chanrock, M.L.H. Green, Effect of carburising agent on the structure of molybdenum carbides, *J. Mater. Chem.* 11 (2001) 3094–3098. <https://doi.org/doi-org.inc.bib.cnrs.fr/10.1039/B104011C>.
- [61] J.-S. Choi, V. Schwartz, E. Santillan-Jimenez, M. Crocker, S. Lewis, M. Lance, H. Meyer, K. More, Structural Evolution of Molybdenum Carbides in Hot Aqueous Environments and Impact on Low-Temperature Hydroprocessing of Acetic Acid, *Catalysts*. 5 (2015) 406–423. <https://doi.org/10.3390/catal5010406>.
- [62] T. Xiao, A.P.E. York, V.C. Williams, H. Al-Megren, A. Hanif, X. Zhou, M.L.H. Green, Preparation of Molybdenum Carbides Using Butane and Their Catalytic Performance, *Chem. Mater.* 12 (2000) 3896–3905. <https://doi.org/10.1021/cm001157t>.
- [63] T. Mo, J. Xu, Y. Yang, Y. Li, Effect of carburization protocols on molybdenum carbide synthesis and study on its performance in CO hydrogenation, *Catal. Today*. 261 (2016) 101–115. <https://doi.org/10.1016/j.cattod.2015.07.014>.
- [64] M. Kakihana, M. Osada, Raman Spectroscopy as a Characterization Tool for Carbon Materials, in: *Carbon Alloys*, Elsevier, (2003) 285–298. <https://doi.org/10.1016/B978-008044163-4/50018-8>.
- [65] G.P. Froment, B.O. Van de Steene, P.S. Van Damme, S. Narayanan, A.G. Goossens, Thermal Cracking of Ethane and Ethane-Propane Mixtures, *Ind. Eng. Chem. Process Des. Dev.* 15 (1976) 495–504. <https://doi.org/10.1021/i260060a004>.
- [66] M.S. Shokrollahi Yancheshmeh, S. Seifzadeh Haghighi, M.R. Gholipour, O. Deghani, M.R. Rahimpour, S. Raeissi, Modeling of ethane pyrolysis process: A study on effects of steam and carbon dioxide on ethylene and hydrogen productions, *Chem. Eng. J.* 215–216 (2013) 550–560. <https://doi.org/10.1016/j.cej.2012.10.078>.

**Chapter 5. Optimization of the
Mo₂C-based catalytic systems for
co-processing of ethane with CO₂**

1. Introduction

Despite the constantly growing availability of renewable energy, the world will continue using fossil resources even after 2040 [1]. Amid the climate crisis: reaching net zero emissions of greenhouse gases by mid-century requires developing the solution for CO₂ circularity and developing the low carbon route for olefins production. Olefins (petrochemicals) are rapidly becoming the largest driver of global oil consumption. They are set to account for more than a third of the growth in oil demand by 2030 and nearly half by 2050 [2]. Therefore, the problem of modernizing the downstream industry becomes more and more acute. This also applies to processes associated with the processing of ethane, which is present in many streams often sending to a flare, sold out at its calorific value for energy generation, or used for olefins production in a conventional ethane steam cracker.

New trends are emerging to reduce GHG emissions of the downstream industry, for example, the oxidative ethane dehydrogenation in CO₂ presence (ODH-CO₂ [3]) and others related to the circularity of CO₂.

Depending on the conditions and nature of the catalysts, several side processes may occur, leading to the formation of undesirable products. The contribution of dry reforming of ethane (DRE), secondary processes of olefins conversion to heavies, or CO₂ methanation become the challenges for the commercialization of a new process. Therefore, it is important to master the factors allowing selective formation of the target products (either olefins or CO).

Regarding monometallic Mo₂C-based catalysts discussed in **Chapter 4**, reoxidation of the Mo-carbide phase with CO₂ to the corresponding metal oxide is another challenge to be understood and controlled. The focus of this chapter is to improve Mo₂C-based catalysts' stability and to understand better how to control the performance of this type of catalyst.

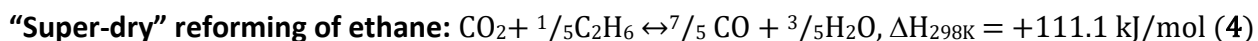
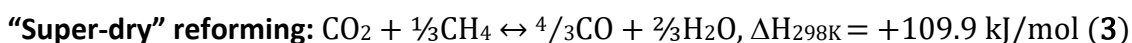
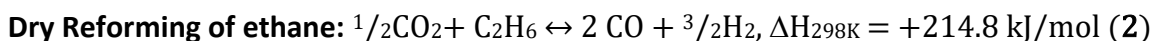
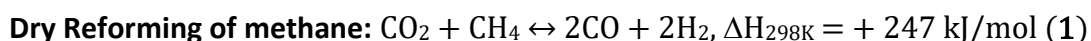
Based on the results reported in **Chapter 4**, one can see that the conversion of ethane on Mo₂C-based catalysts varies significantly depending on the recipe, WHSV, partial pressure, and the ratio CO₂/C₂H₆. The temperature increase leads to a higher conversion of both ethane and CO₂. In general, all the discussed reactions are endothermic and more favored at a higher temperature according to thermodynamic [4,5].

The selectivity in the reaction on molybdenum carbide-containing catalyst can be adjusted for both ODH-CO₂ of ethane and DRE routes. The ODH-CO₂ opens an opportunity for low-carbon olefins production (**Chapter 4**), while the DRE route is an efficient way for CO₂ circularity in a refinery. The orientation of the selectivity can be performed by doping [6] or variation of operating conditions: WHSV, partial pressure, ratio C₂/CO₂, and temperature [7].

The ambitions to reduce GHG emissions from the Liquefied Natural Gas (LNG) plants and the chemical industry require valorization of the off-gas streams, typically rich in ethane. Transformation of CO₂ via a reaction with those waste streams results in double benefits: avoiding CO₂ emissions from flaring and CO₂ utilization via re-circularity at the refinery.

Dry reforming of methane (DRM, **reaction 1**) [8] seems to be an attractive solution. Still, it is very challenging for commercial implementation due to the process's very high reaction temperature and high endothermicity. Currently, there are no commercial purely dry reforming units on stream worldwide. A part of the challenge is related to catalyst coking, and another issue is to process/reactor design. In the case of dry reforming of C₂-containing streams (**reaction 2**), the temperature would be much lower, and the problem with cooking is possible to mitigate. One should mention that in many cases, there is no opportunity to valorize ethylene produced from ethane [9]. So, the main interest of the co-processing of the CO₂ and C₂-rich streams in CO₂ transformation to CO in a reforming process.

Recently, a “super-dry” CH₄ reforming reaction for enhanced CO production from CH₄ and CO₂ was proposed [10] (**reaction 3**):



The idea of “super-dry” reforming is based on the utilization of the hydrogen produced by a dry reforming process *in situ* to perform the reverse water-gas-shift (RWGS) reaction. The catalysts comprise a combination of a classic reforming catalyst (*e.g.*, Ni/MgAl₂O₄), a solid oxygen carrier (Fe₂O₃/MgAl₂O₄), and a CO₂ sorbent (*e.g.*, CaO/Al₂O₃). The autothermal coupling of these three different processes resulted in higher CO₂ utilization per mol of converted methane

compared with conventional dry reforming. The advantage of the “super-dry” reforming process is the lower energy required to transform a mole of CO₂ to CO (2.5 times lower), simplifying the reactor design and decreasing the energy used for product purification. One can see also that 1 mole of ethane transforms stoichiometrically 5 moles of CO₂ (**reaction 4**). In different words, 1 ton of ethane may theoretically transform 7.3 tons of CO₂ to CO. The super-dry reforming of ethane occurs at a much lower temperature than the conversion of methane and is also very economically attractive because it allows economizing about 357 kg of green hydrogen per ton of ethane converted in addition to the avoidance of about 7.3 tons of CO₂. Assuming the current CO₂ costs 100 €/t, and the green hydrogen costs 6000 €/ton, the cumulative benefits from the valorization of a ton of ethane via DRE route would be about 2873 €. This is about three times higher than if one would transform ethane to ethylene. So, in the current economical environment, the dry reforming of ethane [11–13] is even more economically interesting than ethylene production.

This chapter reports the optimization of monometallic Mo-containing catalyst for ODH-CO₂ of ethane and the impact of molybdenum-based materials modification by doping with cobalt. The ultimate goal is to promote a dry reforming route and to get insights in the spent catalyst.

2. Results and discussion

2.2 Optimization of monometallic Mo₂C-based catalysts

2.2.1. Mo-species on the monometallic catalyst

The catalytic behavior of the Mo₂C supported over embryonic zeolite in ODH-CO₂ was discussed in detail in **Chapter 4**. We also studied the influence of the nature of the carbide's precursors (oxidic vs. sulfidic). It was shown that catalysts based on sulfide precursors demonstrated more stable performance and higher hydrogenation activity. Utilization of low acidic embryonic supports led to lower ethane and CO₂ conversion than on highly acidic zeolitic support at the same conditions. However, low acidic support prevented fast deactivation due to negligible coke deposition on the catalyst.

The hypothesis about a transformation of sulfide to carbide phase during the ODH-CO₂ was initially introduced based on the analogy with the conversion of molybdenum oxide to the carbide in the direct methane aromatization (MDA) and in the dry methane reforming (DRM). In general, the 'sulfidic precursors conversion to carbide' concept is based on several experimental proofs:

1. It was determined by ICP elemental analysis and by SEM-EDS that the S-content decreased on the spent samples. From SEM-EDS images, we could measure that the S/Mo ratio in the initial sulfide sample was about 2/1 and in carbide form - 0.42/1. Thus, it was clear that the sulfide phase changed (**Fig.1**). By ICP-MAS analysis of the same samples, that the decrease in sulfur was even higher, around 5.7 times vs. about 5 times by SEM-EDS.

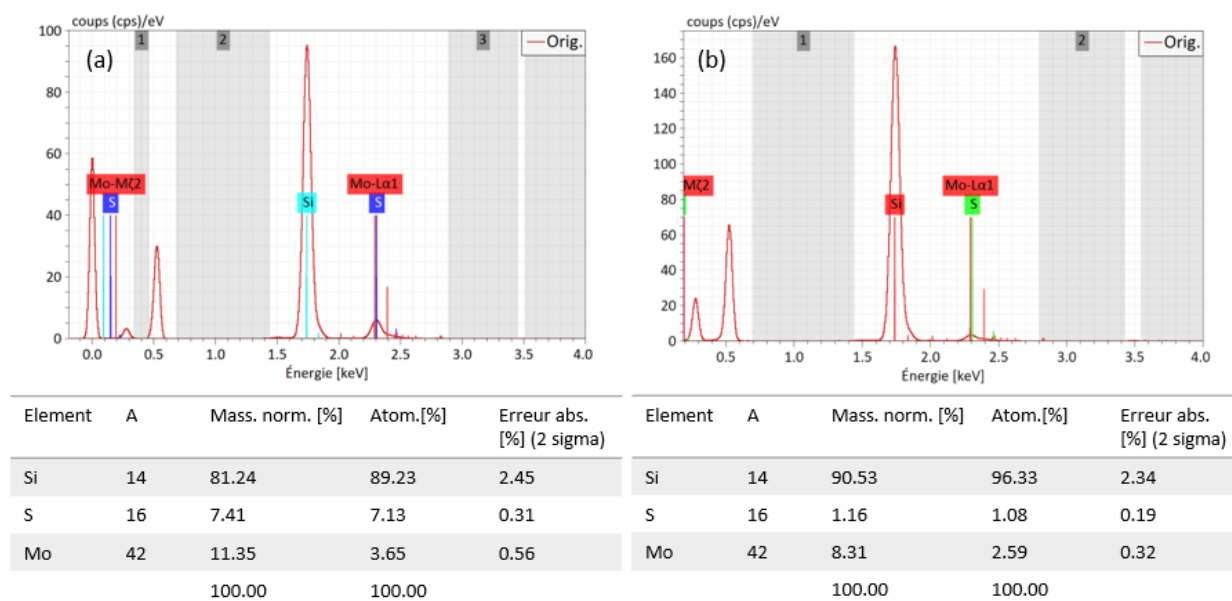


Fig.1- EDS MoS₂ and elemental quantitative data of the MoS₂ before and after catalytic ODH-CO₂ test.

2. As discussed previously, the transformation of Mo-sulfide to carbide was reported in the literature before [14]. MoS₂ interacts with methane at 780 °C forming Mo₂C layers. Mo oxides transformation to the corresponding carbides in the presence of ethane and butane was also reported [15]. So, one can assume that sulfide could also be transformed to the corresponding carbide by reaction with heavier alkanes in the same way.

3. The treatment at a temperature below 800 °C in an inert environment resulted in no changes in MoS₂ structure. More interestingly, the EZ_{Si}-5%MoS₂ used in a hydrocarbon-free environment in CO₂ hydrogenation (RWGS, reverse water-gas-shift) in the temperature range 700-750 °C, demonstrated not only a stable performance of the catalyst but also a conservation of the sulfidic phase (**Fig.2**).

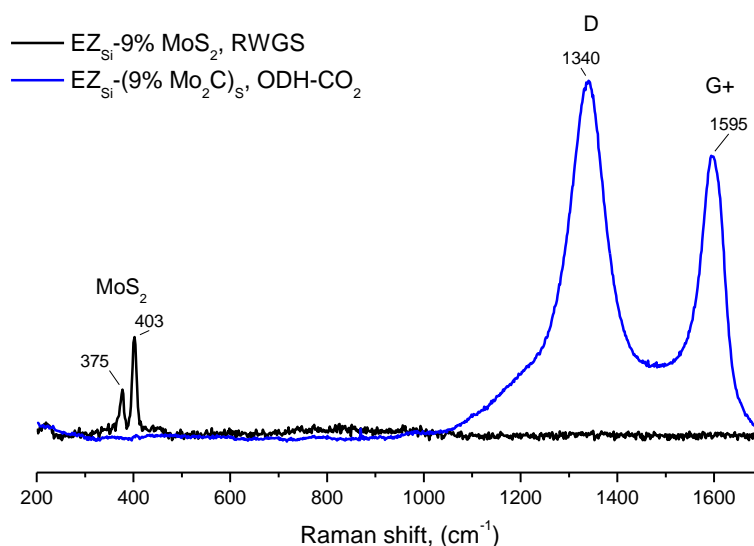


Fig.2- Raman spectrum of spent samples under CO₂ conversion conditions with and without the presence of ethane (ODH-CO₂ and RWGS).

4. The XRD technique confirmed the presence of some MoO₂ phase in the spent ODH-CO₂ catalyst (**Fig. 3**). It can be explained by the reoxidation of the formed Mo₂C-phase with CO₂. Nevertheless, for the sample tested in ODH-CO₂ of ethane at 800 °C, the Mo₂C peaks were still well observed. This result suggests that the kinetics of the Mo₂C formation from oxide is faster than the reoxidation with CO₂ at high temperatures. Thus, direct oxidation of MoS₂ to dioxide could be excluded based on its stability under CO₂ flow.

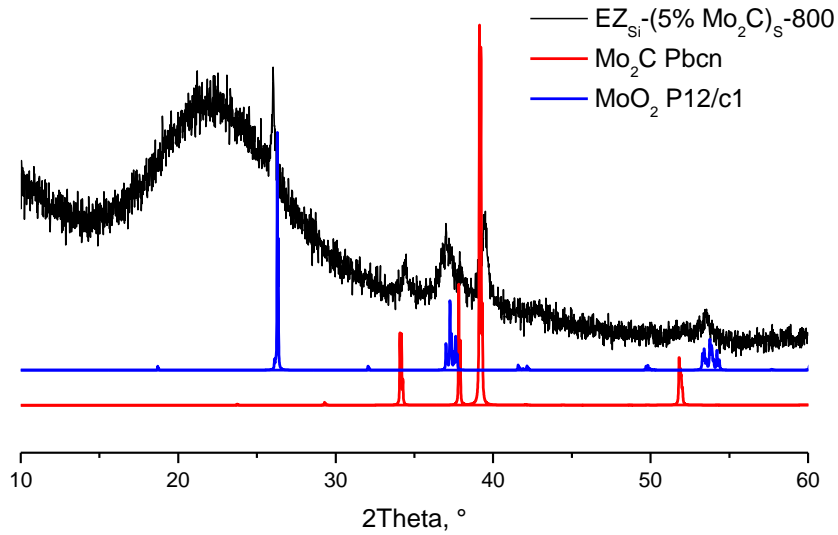


Fig.3- XRD patterns of spent sample produced from sulfidic precursor $\text{EZ}_{\text{Si}}\text{-5\%MoS}_2$.

5. The TGA analysis of the spent $\text{EZ}_{\text{Si}}\text{-5\%Mo}_2\text{C}$ (**Fig. 4**) exhibits a specific for Mo_2C -containing samples weight increasing (+0.3%), related to the carbide oxidation to oxide under air. This curve character was observed for all samples based on MoS_2 precursors.

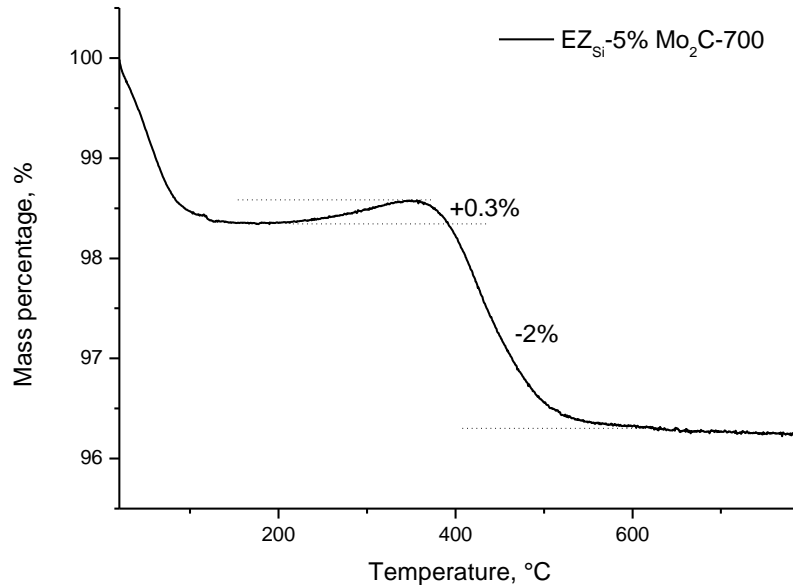


Fig.4- Thermogravimetric curve of the spent sample produced from a sulfidic precursor and subjected to reaction at 700 °C.

2.2.2. Characterization by X-Ray diffraction of Mo-carbide phases produced from different precursors

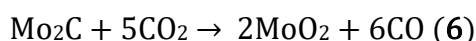
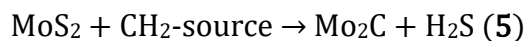
The effect of the nature of carbon source on the formation of Mo₂C structure was reported in the literature [15]. The authors concluded that the utilization of ethane or butane dramatically reduces the particle size of carbide species compared to the one produced with methane. This is also related to the low temperature required to form the carbide phase with ethane than with methane. With an ethane source, a full conversion of MoO₃ to Mo₂C already occurs at 630 °C [15]. Therefore, detection of the well-dispersed carbide by XRD in the sample prepared with a non-methane carbon source is difficult to achieve. The Mo₂C could only be detected on the spent samples in case of accumulations caused by several reduction/reoxidation cycles.

After studying different samples, carbide peaks were only observed for the spent samples on ODH-CO₂ of ethane at 800 °C (**Fig. 3**). The EZ_{Si}-(5%Mo₂C)_S-800 contained peaks at 26, 34.2, and multiplet around 37.5, 39.3, 53.7 °. The obtained patterns were compared with the literature data for MoO₂ (space group P12/c1, Inorganic Crystal Structure Database: ICSD collection code 244050) and Mo₂C (space group Pbcn, Inorganic Crystal Structure Database: ICSD collection code 1326). The observed results proved the presence of both MoO₂ and Mo₂C phases in the sample. It turned out that on the samples aged at low temperatures the size of Mo₂C is too small to be easily detected by XRD. The smaller particle is also easier to reoxidize to MoO₂. Therefore, the contribution of the reoxidation to MoO₂ is significant in the temperature range between 700-750 °C. It was reported that the transformation of MoO₂ to Mo₂C with methane [17] or with CO [18] is significant only at a temperature as high as 900 °C. For the studied nanoparticles in a reaction with ethane/ethylene, a lower carburization temperature of MoO₂ can be assumed. Thus, one can assume that there is a kind of reversible equilibrium for the oxidation and reduction process over the surface of the catalyst. It is known that the catalyst activity is defined by the number of accessible active (Mo₂C) species. Since these species have a strong affinity to agglomerate due to the reduction/reoxidation reaction, which in turn leads to an increase of the particle size, it is expected to be the main deactivation mechanism.

2.2.3. Optimization of the activity of Mo₂C-based samples in co-processing of CO₂ and ethane by different pretreatment

As shown in the previous **Chapter 4 (Fig. 9)**, an initial drop in CO₂ conversion is observed for all the sulfide-derived catalysts. To improve the performance, a deeper investigation of the role of sulfidic precursors was performed.

A carbon build typically characterizes the initial reaction step up on the samples up to 1-2 wt%. After the initial build-up, the carbon content remains the same until the end of the test. The key reason for the formation of carbon species is the transformation of the MoS₂ precursor to the Mo₂C phase. This step corresponds to the peak in activity. After the transformation, the Mo₂C (**reaction 5**) phase in an atmosphere of CO₂ was partially reoxidized to MoO₂-phase (**reaction 6**). MoS₂ and Mo₂C phases are highly active in CO₂ hydrogenation, while MoO₂ is not active at all. So, the partial reoxidation provoked a drop in activity till reaching the equilibrium between Mo₂C and MoO₂ phases. Eventually, a kind of equilibrium between Mo₂C and MoO₂ phases co-existing on the samples resulted in a stable catalyst activity. The equilibrium ratio between the oxide and carbide phases depends on operating conditions.



To identify the parameters regulating the activity of catalysts, a series of additional experiments was performed. The prepared samples differed in the preparation route of the oxidic precursor's phase and the wt.% of the active phase. Molybdenum oxides for sulfurizing were obtained by wet impregnation (WI) and hydrothermal treatment (HT). Between the samples with 5wt.% of the active phase, HT precursor in sulfidic form showed the highest average conversion for both C₂H₆ dehydrogenation and CO₂ hydrogenation (**Fig. 5a**). The average CO₂ and ethane conversion over EZ_{Si}-(5%Mo₂C)_S-HT and EZ_{Si}-(9%Mo₂C)_S-HT were very similar. CO₂ conversion over EZ_{Si}-(5%Mo₂C)_S-HT was 45.5%. Higher active phase content allowed further improving stability in CO₂ conversion (**Fig. 5b**). After 200 minutes-on-stream, a stabilized conversion at the level of 44-43% (EZ_{Si}-(9%Mo₂C)_S-HT) was observed.

The effect of WHSV on CO₂ conversion was studied on EZ_{Si}-(9%Mo₂C)_S-HT (**Fig. 5a, b**). The minimization of the initial CO₂ conversion was reached after decreasing the contact time. A comparison of the performances of EZ_{Si}-(9%Mo₂C)_S-HT catalyst at WHSV=5.9 and 11.8 h⁻¹ shows

2 times lower value of CO₂ conversion between the initial and the value at 250 min. The selectivity of the products for these four samples was very similar to each other. The main product remains ethylene, with a selectivity of 92-94%. Thus, the formation of a heavy fraction cannot affect the stability of the operation in any way.

All spent catalysts were studied by XRD to detect the formation of some crystalline phases (**Fig.6**). The formation of the MoO₂ phase correlates with the CO₂ conversion in all the cases: EZ_{Si}-(5%Mo₂C)_S-WI (WHSV=5.9 h⁻¹), EZ_{Si}-(5%Mo₂C)_S-HT (WHSV=5.9 h⁻¹) and EZ_{Si}-(9%Mo₂C)_S-HT (WHSV=5.9 h⁻¹). For the sample EZ_{Si}-(9%Mo₂C)_S-HT (WHSV=11.8 h⁻¹) with the most stable carbon dioxide conversion, low-resolved peaks of MoO₂ and some Mo₂C traces were indicated. Thus, increasing the WHSV is an option for improving the lifetime of the presented EZ-Mo₂C catalytic systems and to favor the presence of Mo₂C/MoS₂ species vs. MoO₂ on the catalyst.

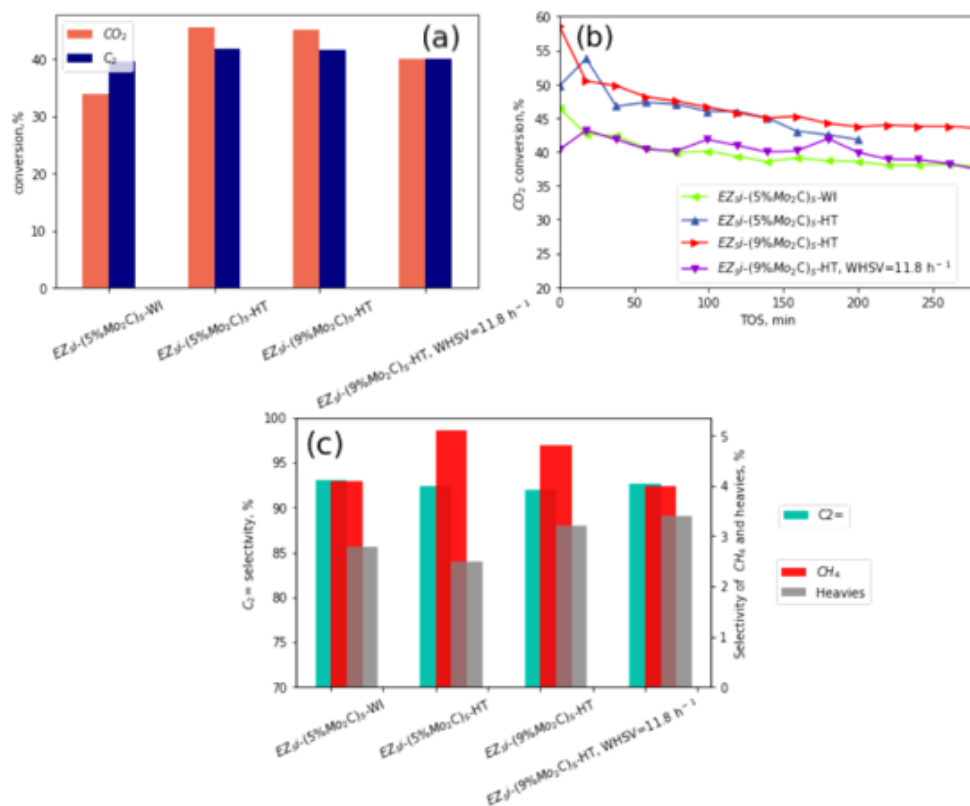


Fig. 5- ODH-CO₂ of ethane (C₂) on catalysts: a) average conversion of CO₂ and ethane; b) conversion of CO₂ and ethane as a function of time on stream (TOS); c) selectivities to the C₂ products (coke-free basis, T = 750 °C, P = 1 atm, C₂H₆/CO₂ = 1/0.74, by default WHSV = 5.9 h⁻¹).

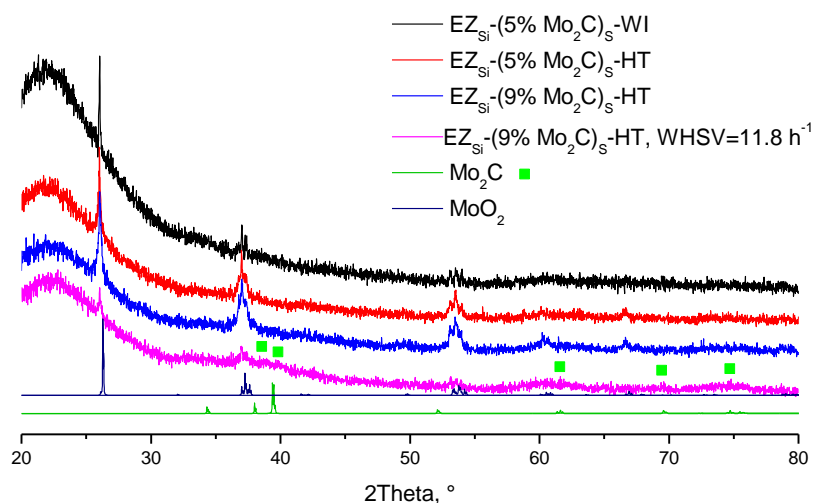


Fig. 6- XRD patterns of spent sample produced from sulfidic precursors (coke-free basis, T =750 °C, P = 1 atm, C₂H₆/CO₂ = 1/0.74, by default WHSV =5.9 h⁻¹).

Several conclusions may be drawn by comparing results on the EZSi-(x%Mo₂C)_S catalyst from the current work and the others Mo₂C-based systems from the literature (Table 1). In literature, the Mo-carbide-based systems were tested only at low temperatures in CO₂ + ethane co-processing. The catalyst obtained in the current work on the MoS₂-precursors is much more active in CO₂ hydrogenation than the reported in the literature samples while maintaining very high selectivity to ethylene (Table 1).

Table 1. Comparison of the catalyst performances in CO₂ and ethane coprocessing

P, bar	T, °C	CO ₂ conv., %	C ₂ H ₆ conv., %	C ₂ H ₄ selectivity, %	Reference
1	600	0-6	1-6	60-80	[4]
1	600		2-14	70-90	[6]
1	600	1-8	0-4	60	[19]
1	600		≈15	92	[7]
1	690		65.00*	≈9**	[7]
1	700	9.7	14.7	98	This work
1	750	34-45	39.6	95	This work

*- C₂H₆/CO₂=1/2.7, DRE-route

**-calculated data based on presented values

2.2.4. Conclusion for the monometallic Mo₂C-based catalyst characterization and tuning

For intermediate conclusions, it is summarized the phases' transformation properties and demonstrates catalytic behaviors for Mo₂C-based systems. Based on the literature and experimental data analysis, one can conclude:

- No MoS₂ reoxidation under CO₂ environment; MoS₂ shows a significant hydrogenation activity;
- The gradual transformation of MoS₂ to Mo₂C occurs under a hydrocarbon environment;
- Reoxidation of Mo₂C to MoO₂ takes place in CO₂ environment;
- Mo₂C shows a significant hydrogenation activity in CO₂ to CO;
- MoO₂ species are inactive in hydrogenation and show a strong tendency to agglomerate. MoO₂ agglomeration is the origin of catalyst deactivation;
- MoO₂ species are bulkier, and their content could be higher than carbides due to the catalyst oxidation;
- In the presence of both ethane and CO₂, both Mo-carbide and Mo-oxides species co-exist on the catalyst surface; its ratio is defined by operating conditions;
- The intensification and stabilization of the catalytic behavior are possible by precursors optimization;
- Precursors optimization is performed on the oxide preparation step;
- Hydrothermal precursors (HT) are more efficient than wet impregnated (WI); It provides an increase in the CO₂ conversion of about 10%;
- Precursors modifications do not prevent the catalyst's reoxidation;
- A complex approach based on a combination of higher content of the active phase and the hydrothermal treatment (9 wt.% Mo, HT) of the precursors lead to the most promising results. It results in higher activity and better stability of CO₂ conversion;
- Improving the activity of Mo₂C-based samples allows retain the ODH-CO₂ pathway without the intensification of co-processes.

2.3 Cobalt-doped molybdenum catalysts

The doping with cobalt was done in view of reducing the oxidation degree of the **Mo₂C** to **MoO₂**.

2.3.1. Characterization of the catalysts

Characterization of the cobalt-doped samples performed in contrast to monometallic samples.

X-ray diffraction (XRD) indicates that all supported samples in an embryonic zeolite (EZ) with Mo or Mo-Co conserved the original X-ray amorphous structure (**Fig. 7**). For earlier discussed monometallic samples (wet-impregnated (WI), and hydrothermally synthesized (HT)) no visible peaks appear in the diffractogram (**Fig.7**). The low intense peak around 26° for Mo-Co loaded samples could be attributed to the mixed oxidic phase (MoO₃ and CoO_x). The EDX mapping (**Fig.8**) indicates uniform metal distribution in the EZ samples regardless of their composition.

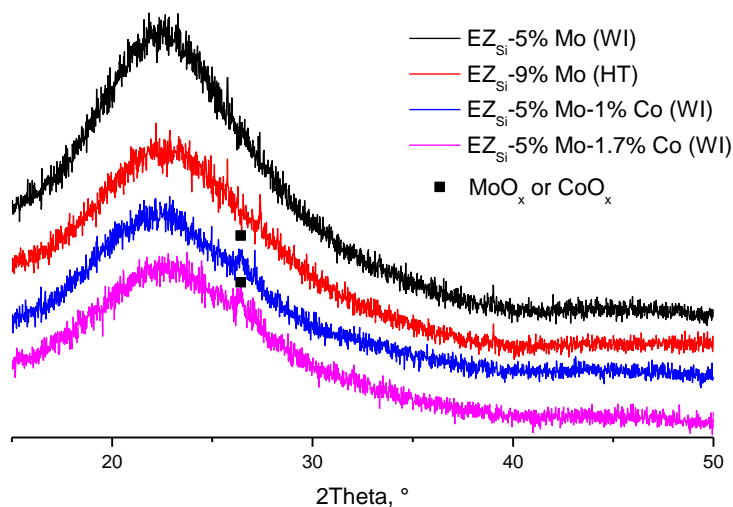


Fig.7- XRD patterns of EZ_{Si}-5%Mo (WI), EZ_{Si}-9%Mo (HT), EZ_{Si}-5%MoO₃-1%CoO_x and EZ_{Si}-5%MoO₃-1.7%CoO_x.

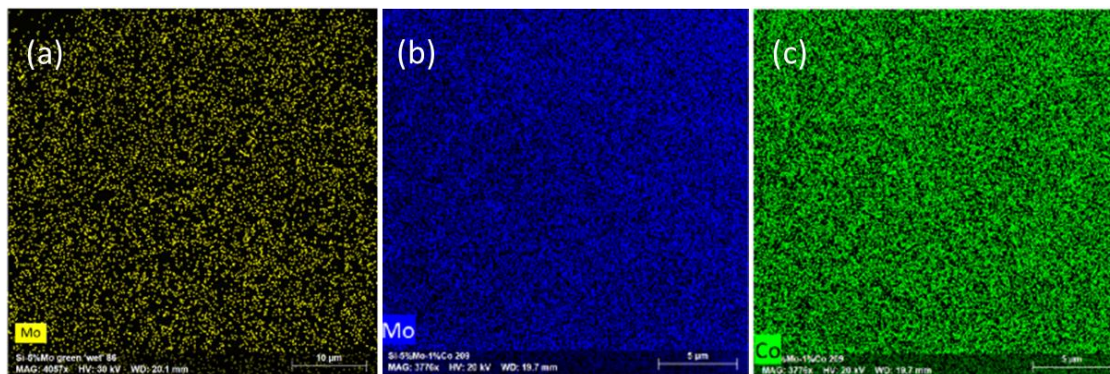


Fig. 8- EDX elemental mapping of Mo in EZ_{Si}-5%Mo (a) and Mo and Co inEZ_{Si}-5%MoO₃-1%CoO_x (b) and (c).

Raman spectroscopy was used to identify the nature of the metal phase in the monometallic and bimetallic EZ-supported catalysts (**Fig.9**). The Raman spectra of both samples EZ_{Si}-5%Mo-WI and EZ_{Si}-9%Mo-HT, show a presence of the similar oxidic species. The bands at

668, 821, and about 990 cm⁻¹ could be attributed to the α-MoO₃ phase, at 1001 cm⁻¹ to MoO_x. The bands in the range 950-960 cm⁻¹ indicated the presence of various polymolybdates.

For bimetallic samples, the bands at 485 and 692 cm⁻¹ correspond to Co(II, III)O_x species [20] (**Fig.9b**). Mo-oxidic species in these systems were characterized by the peaks at 811, 870, and 937 cm⁻¹. The band at 870 and 935 cm⁻¹ could be attributed to Mo–O–Mo and Mo–O_t functionalities of [Mo₇O₂₄]⁶⁻ polymolybdate species [21,22]. The band at 811 cm⁻¹ was obtained by shifting the main characteristic band of the MoO₃ phase. For the monometallic sample (EZ_{Si}-5%Mo-WI), the peaks in the Raman spectra show a co-existence of both α-MoO₃ and polymolybdate species (**Chapter 4**), while they are present in similar proportions.

The formation of 2H-MoS₂ [23,24] was already shown and discussed in **Chapter 4**. The conversion of both oxides to the sulfide phases was successfully monitored by Raman spectroscopy in the same way as for monometallic counterparts (**Fig.10**). Bands at 370 and 404 cm⁻¹ are attributed to 2H-MoS₂, a right shoulder of the double band with the highest point at 410 cm⁻¹ and the band at 441 cm⁻¹ is attributed to Co polysulfides[25].

2.3.2. Role of the cobalt doping

The catalytic performance of Co-doped bimetallic (EZ_{Si}-(5%Mo₂C-1%Co_xC)_S), monometallic Mo-based (EZ_{Si}-(5%Mo₂C)_S), and Co-based (EZ_{Si}-(5%Co_xC)_S) catalyst in the ethane and CO₂ co-processing was investigated (**Fig.11a**). On the Co-doped catalyst, CO₂ conversion exceeded 25% (26.4%), and ethane conversion was 19%. On the pure Mo-sample, the ethane conversion was higher than the conversion of CO₂. However, both conversions were relatively low: CO₂ conversion was 9.7%, and the ethane conversion was 14.7%. On the bimetallic samples, the ethane and CO₂ conversions were much higher (EZ_{Si}-(5%Mo₂C-1%Co_xC)_S), i.e., 72.7 and 31.9%, respectively.

The products' selectivity distribution was also evaluated for all C-contained products (**Fig.11b**). In contrast to EZ_{Si}-(5%Mo₂C-1%Co_xC)_S and to EZ_{Si}-(5%Mo₂C)_S, on EZ_{Si}-(5%Co_xC)_S was founded a strong tendency to CH₄ formation with the selectivity of around 7%. The ethylene formation as a major product was observed only on EZ_{Si}-(5%Mo₂C)_S (70.5%). It was equivalent 98.5% C₂-based product selectivity. On both Co-contained samples, it was noticed the formation

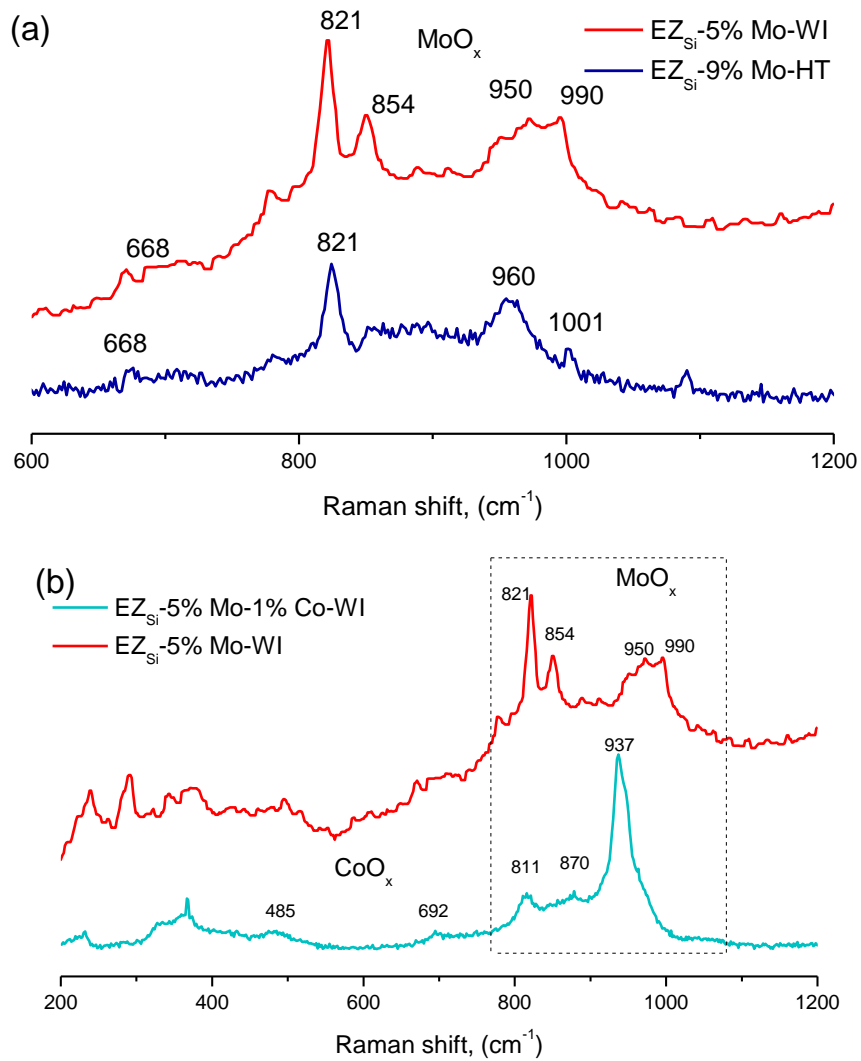


Fig.9- Raman spectrum of EZ decorated with a) Mo oxide prepared by wetness impregnation (WI) and hydrothermal treatment (HT); b) Mo and Co oxide prepared by wetness impregnation (WI) and compared with EZ decorated with a Mo oxide (WI).

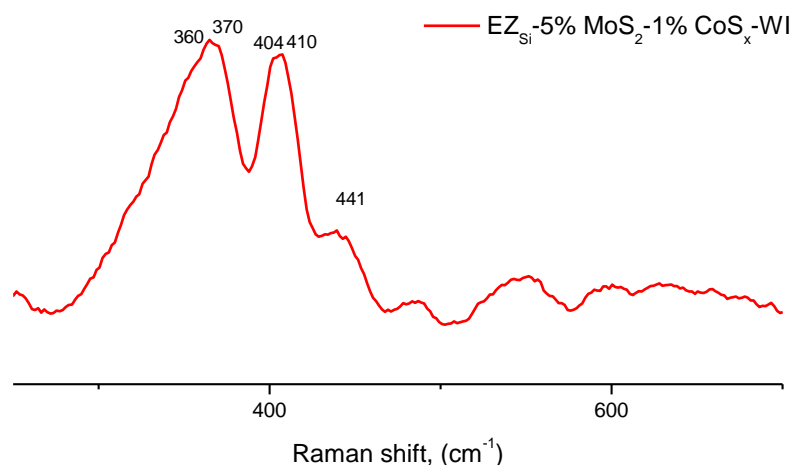


Fig.10- Raman spectrum of EZ decorated with a Mo and Co after sulfurizing

of a high amount of CO. CO selectivity on EZ_{Si}-(5%Mo₂C-1%Co_xC)_S was 86%, while ethylene selectivity was around 12%. The heavies content increases with C₂ conversion growth. The higher selectivity to CO suggests that the reaction proceeds according to the dry reforming mechanism.

Thanks to dry reforming the ethane could be converted to both ethylene and CO. We employed the terms “ODH-CO₂-route” for processes with high selectivity to ethylene and “DRE-route” for mostly CO production process. However, it should be taken into account that none of the routes achieves 100% selectivity. Thus, instead of displaying “ODH-CO₂ of ethane (C₂)” on catalysts, we discuss “ethane (C₂) co-processing with CO₂ on catalysts”. This is ethane processing with CO₂ with a tendency to be one of the mechanisms. Product selectivities henceforth are presented as all C-products selectivities (**Fig.11**).

2.3.3. WHSV impact on catalyst performance

The effect of the tuning weight hourly space velocity (WHSV) on C₂ dehydrogenation in CO₂ presence was studied at 700 and 750 °C.

At 700 °C the WHSV tuned from 5.9 to 11.8 h⁻¹ (**Fig. 12**). It resulted in a change of preferable reaction pathway (to ODH-CO₂). When CO₂ conversion at 700 °C and WHSV 5.9 h⁻¹ reached about 72%, at WHSV=11.8 h⁻¹ it was 22.3%. Ethane conversion had also changed, it decreased from 32 to 18.2%. Ethane and CO₂ conversion on EZ_{Si}-(5%Mo₂C-1%Co_xC)_S and WHSV=11.8 h⁻¹ were superior to analogous values at EZ_{Si}-(5%Mo₂C)_S at WHSV=5.9 h⁻¹ (**Fig.11**).

Ethylene C₂-based selectivity on EZ_{Si}-(5%Mo₂C-1%Co_xC)_S was 95% at WHSV=11.8 h⁻¹, which is similar to the performance of EZ_{Si}-(5%Mo₂C)_S (Chapter 4).

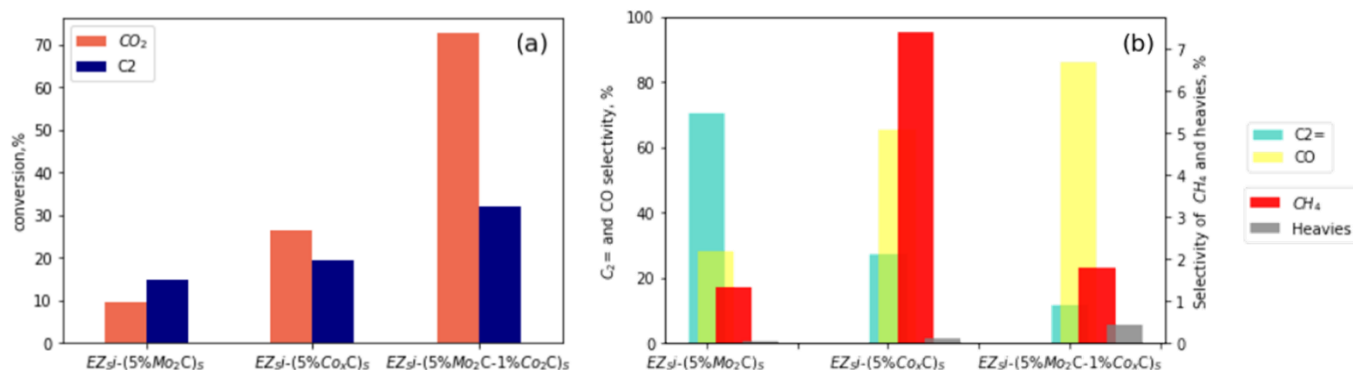


Fig. 11- Ethane (C₂) co-processing with CO₂ on catalysts: a) average conversion of CO₂ and ethane; b) all C-products selectivities (coke-free basis, T =700 °C, P = 1 atm, C₂H₆/CO₂ = 1/0.74, WHSV =5.9 h⁻¹. By default, all samples prepared by WI).

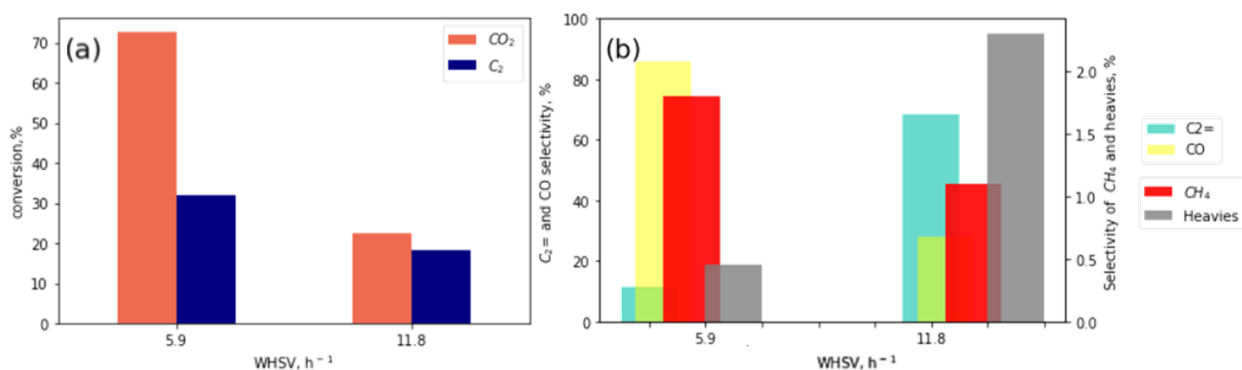


Fig.12-Ethane (C₂) co-processing with CO₂ on EZ_{Si}-(5%Mo₂C-1%Co_xC)_S a) average conversion of CO₂ and ethane; b) all C-products selectivities (coke-free basis) as a function of WHSV. (T =700 °C, P = 1 atm, C₂H₆/CO₂ = 1/0.74).

WHSV regulation on bimetallic samples allows tuning of the preferable ethane processing pathway. At higher WHSV and lower contact time, the process is set to ethylene production. Product selectivity distribution proves that an increase in WHSV prevents the dry reforming. At lower WHSV the process is more selective to CO production. At 700 °C, ODH-CO₂ performed on

EZ_{Si}-(5%Mo₂C-1%Co_xC)_S (WHSV=11.8 h⁻¹) allowed converting a higher amount both CO₂ and ethane reactants than on Mo monometallic samples.

The EZ_{Si}-(5%Mo₂C-1%Co_xC)_S sample at WHSV=11.8 h⁻¹ showed stable selectivity independently on the conversion level (**Fig. 13a,b**). Thus, Co-doping leads to a stable catalytic performance at 700 °C [26].

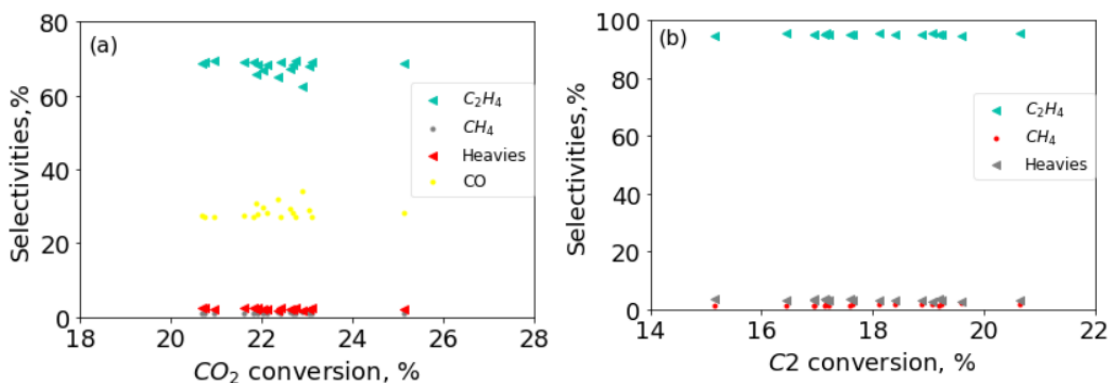


Fig. 13- a) All C-products selectivity versus CO₂ conversion, b) C₂-products selectivity ethane conversion (coke-free basis, T =700 °C, P = 1 atm, C₂H₆/CO₂ = 1/0.74, WHSV =11.8 h⁻¹, EZ_{Si}-(5%Mo₂C-1%Co_xC)_S).

It was founded a lower selectivity for heavies at WHSV=5.9 h⁻¹, despite the longer contact time (**Fig.12b**). If heavier condensed products were formed, they could be determined using TGA. The TG measurement for spent EZ_{Si}-(5%Mo₂C-1%Co_xC)_S showed a formation of 1.4% of coke at WHSV=5.9 h⁻¹. It indicates that dry reforming conditions lead to the condensation of heavy products. Compared with earlier results under ODH-CO₂ and monometallic catalyst, the carbon content lower than 2% is an improvement [26]. For the second sample (WHSV=11.8 h⁻¹), the formation of coke was almost not recorded (**Fig.14**). The formed olefins and aromatics did not pass into coke.

It was noticed that the ethane conversion level on EZ_{Si}-(5%Mo₂C-1%Co_xC)_S (WHSV=11.8 h⁻¹) was similar to results on monometallic EZ_{Si}-(5%Mo₂C)_S (WHSV=5.9 h⁻¹). In order to compare these results, the data for the MoS₂-derived sample was linearly extrapolated to the same level of conversion of ethane (18.2%) (**Fig.15**). It was equivalent to a temperature increase of 7 °C for a monometallic sample. After extrapolation, ethylene selectivity attained a similar level. The sum

of the methane and heavy fractions selectivity was the highest for EZ_{Si}-(5%Mo₂C-1%Co_xC)_s and equaled 5%. In contrast to EZ_{Si}-(5%Co_xC)_s, Co-doped samples showed higher selectivity to ethylene, to EZ_{Si}-(5%Mo₂C)_s improved dehydrogenation-hydrogenation properties. The additional advantage of EZ_{Si}-(5%Mo₂C-1%Co_xC)_s catalytic system was the close results were at the lower time contact (WHSV =11.8 h⁻¹).

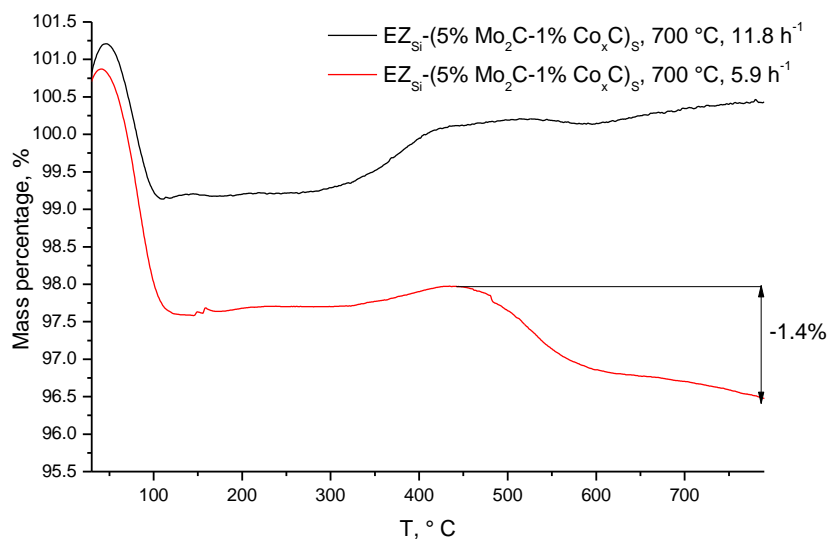


Fig. 14- Thermogravimetric analysis of spent EZ_{Si}-(5%Mo₂C-1%Co_xC)_s under DRE (WHSV=5.9 h⁻¹) and ODH-CO₂ (WHSV=11.8 h⁻¹) conditions.

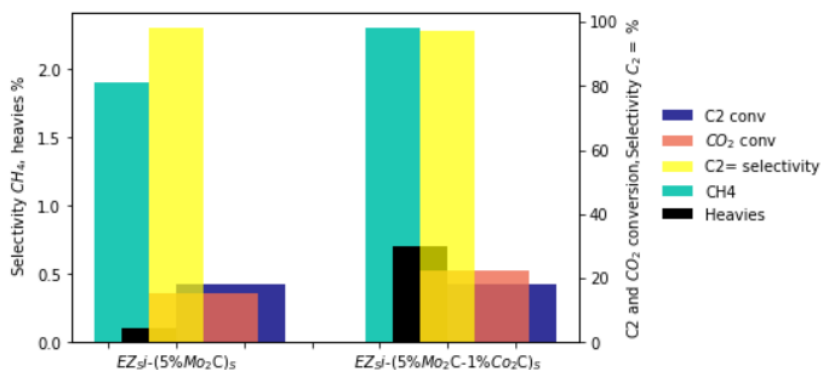


Fig. 15- Comparison of catalytic (EZ_{Si}-(5%Mo₂C)_s) and EZ_{Si}-(5%Mo₂C-1%Co_xC)_s in ODH-CO₂ of ethane at the same conversion level of ethane 18.2%. (coke-free basis, T =700 °C, P = 1 atm, C₂H₆/CO₂ = 1/0.74, WHSV =5.9 h⁻¹ for EZ_{Si}-(5%Mo₂C)_s, WHSV =11.8 h⁻¹ for EZ_{Si}-(5%Mo₂C-1%Co_xC)_s).

By the analogy with experiments at 700 °C, at 750 °C were performed, experiments with various WHSV. Similar to the experiments at 700 °C at WHSV=5.9 h⁻¹ the preferable pathway was DRE, and the minimal value at 750 °C was equal to 11.8 h⁻¹. The highest value was obtained by increasing this parameter by 50%: 17.7 h⁻¹. At WHSV=17.7 h⁻¹, CO₂ conversion was lower than for ethane (41.3%) and reached 33.6% (**Fig.16**). Products contained mostly ethylene and some methane and heavies. It indicates the occurrence of two routes in the system: ODH-CO₂ and DDE. Ethylene selectivity was 67.5% (**Fig.16b**). Whereas at WHSV=11.8 h⁻¹ DRE was preferred, and CO₂ conversion was 1.5 times higher than ethane conversion. CO selectivity was around 70%. Methane and heavies selectivities were slightly higher than for samples tested under DRE-route at 700 °C (**Fig.12b**).

Thus, the variation of WHSV is an efficient option to adjust the CO₂ and ethane conversions and the product distribution over the Co-doped Mo carbide catalytic system.

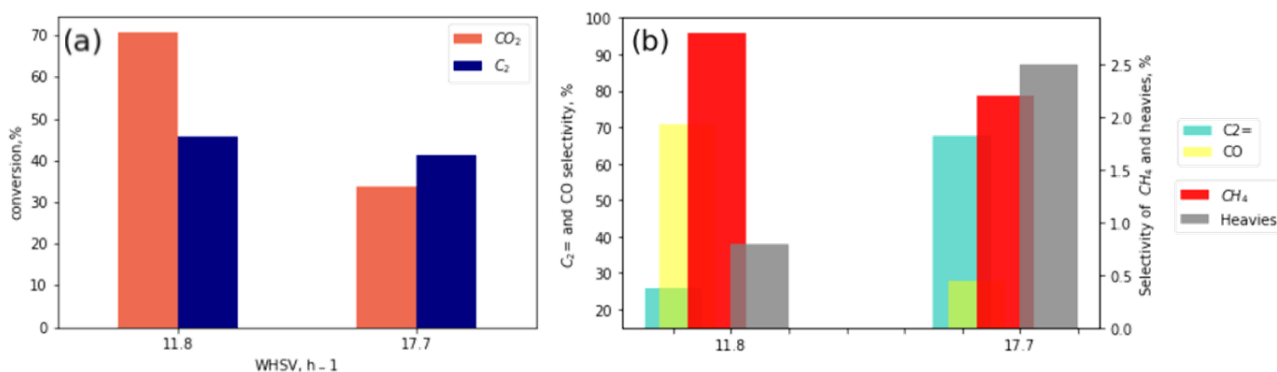


Fig.16- Ethane (C₂) co-processing with CO₂ on EZSi-(5%Mo₂C-1%Co_xC)₅: a) average conversion of CO₂ and ethane; b) all C-products selectivities (coke-free basis) as a function of WHSV, h⁻¹ (T =750 °C, P = 1 atm, C₂H₆/CO₂ = 1/0.74).

2.3.4. Impact of reaction temperature

In order to understand the impact of temperature on the selectivity of ODH-CO₂ or DRE pathways, the EZSi-(5%Mo₂C-1%Co_xC)₅ catalyst was tested at 700, 730, and 750 °C at WHSV=11.8 h⁻¹. The increase in the temperature from 700 °C to 750 °C resulted in a significant rise in ethane and the CO₂ conversion from 730 °C (**Fig.17a**).

One can see that the ratio CO/C₂= could be used as a simple descriptor of the reaction pathway. If the ODH-CO₂ pathway dominates, the ratio should be 1 or lower. A significantly higher

ratio leads to a strong contribution of the dry reforming reaction. Based on the stoichiometry, one can see that at 700 °C, a major part of ethane substantially transforms according to ODH-CO₂ route, while at 750 °C, about 55% of ethane reacted via the reforming pathway and 40% reacted via ODH-CO₂ (CO/C₂H₄ ratio ~5.6, **Fig.17b**).

Since there are competing processes in the system, it was important to include CO in the selectivity calculations (**Fig.17c**). The ethylene selectivity decreased from 69 to 26%, and the selectivity to CO increased from 28 to 70.7%. An increase in the selectivity to methane was also observed, and a decrease in the selectivity to heavies at higher temperatures (Fig.17c). The lower selectivities to heavies could also be explained by their participation in the reforming with the formation of methane.

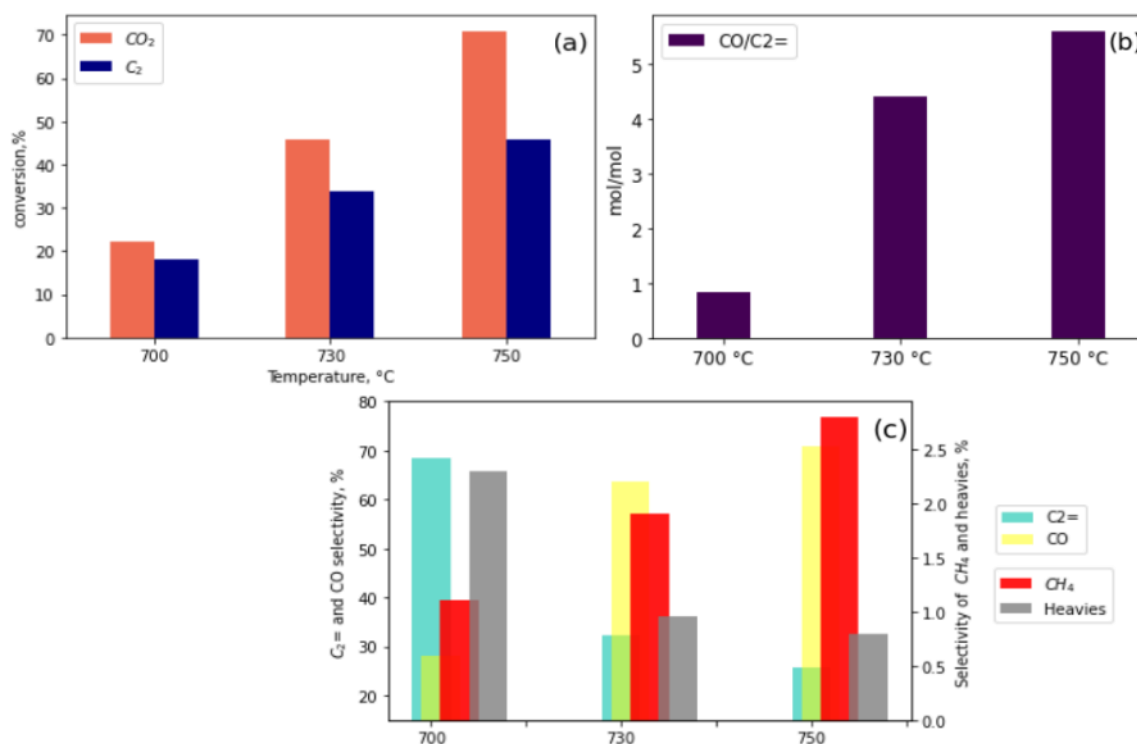


Fig. 17- Ethane (C₂) co-processing with CO₂ on EZSi-(5%Mo₂C-1%Co_xC)_s catalyst: a) average conversion of CO₂ and ethane; b) CO/C₂H₆ ratio as temperature function; c) all C-products selectivities (coke-free basis, T =750 °C, P = 1 atm, C₂H₆/CO₂ = 1/0.74, WHSV=11.8 h⁻¹ for; *1st day for 730 °C).

2.3.5. Impact of cobalt content on the catalyst

The following investigation was based on the conditions for ODH-CO₂-route at 700 °C. The increase of Co content from 1 wt% to 1.7 wt.% (EZ_{Si}-(5%Mo₂C-1.7%Co_xC)_s) significantly increased CO₂ conversion at the same temperature. At the same time, the conversion of ethane increased only by 4% (**Fig. 18a**). The CO/C₂H₄ ratio indicates that the higher Co content promotes the reforming reaction between C₂H₆ and CO₂ (DRE pathway, **Fig. 18b**). The contribution of DRE to ethane conversion consisted about 60%, around 30% was from ODH-CO₂. The products' selectivity on C-basis is compared in **Fig. 18c**. A dramatic change could be noted only for CO/C₂H₄ selectivity ratio. Thus, the contribution of the direct dehydrogenation of ethane, estimated by the content of methane and heavies, remained virtually unchanged for various Mo-Co content. The CO₂ conversion as a function of TOS decreased from 50% to 37% on EZ_{Si}-(5%Mo₂C-1.7%Co_xC)_s in 4 hours. For the sample with 1 wt.% cobalt content, no deactivation was observed (**Fig. 18d**).

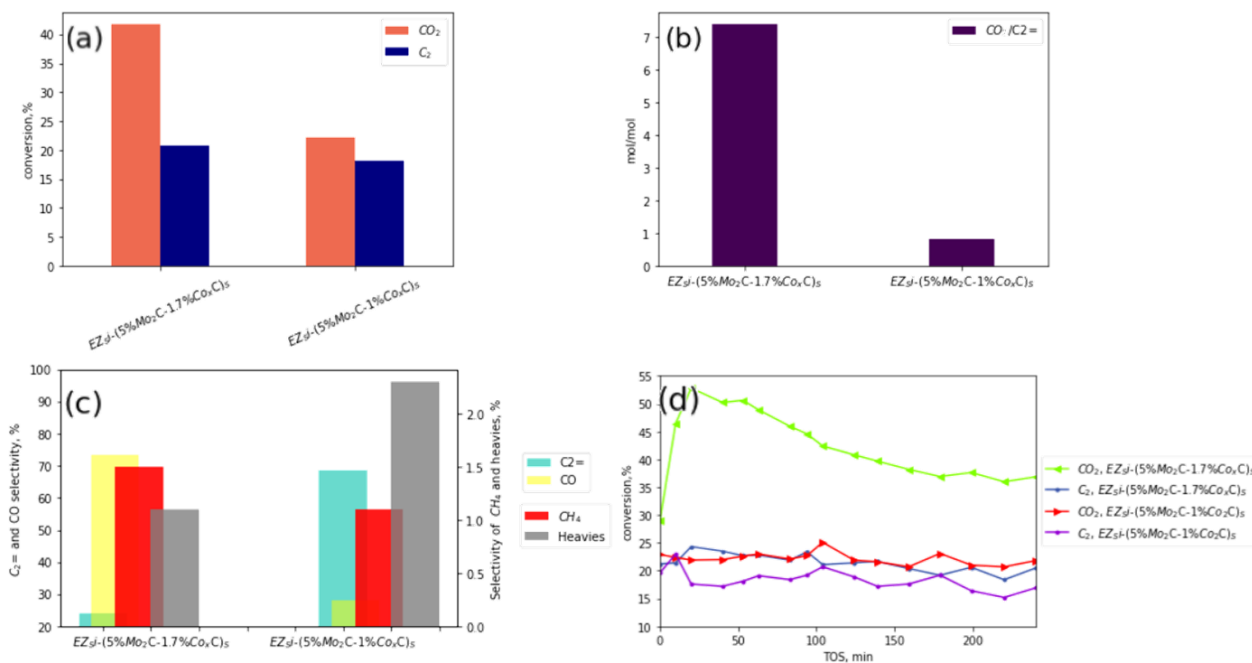


Fig.18- Ethane (C₂) co-processing with CO₂ on EZ_{Si}-(5%Mo₂C-1%Co_xC)_s and EZ_{Si}-(5%Mo₂C-1.7%Co_xC)_s catalysts: a) average conversion of CO₂ and ethane; b) CO/C₂H₄ products molar ratio; c) all C-products selectivities (coke-free basis, d) CO₂ and C₂ conversion as the function of time on stream (TOS) (T =700 °C, P = 1 atm, C₂H₆/CO₂ = 1/0.74, WHSV=11.8 h⁻¹).

Comparing all C-products selectivity on bimetallic catalysts with EZ_{Si}-(5%Mo₂C)_S and non-catalytic (thermal) process showed that the heavies' content was comparable to the results for the non-catalytic thermal process (**Fig.19**). At 700 °C, for monometallic all products selectivity was comparable with results on EZ_{Si}-(5%Mo₂C-1%Co_xC)_S. The most significant methane selectivity was detected via the thermal process. Its selectivity was about 4%.

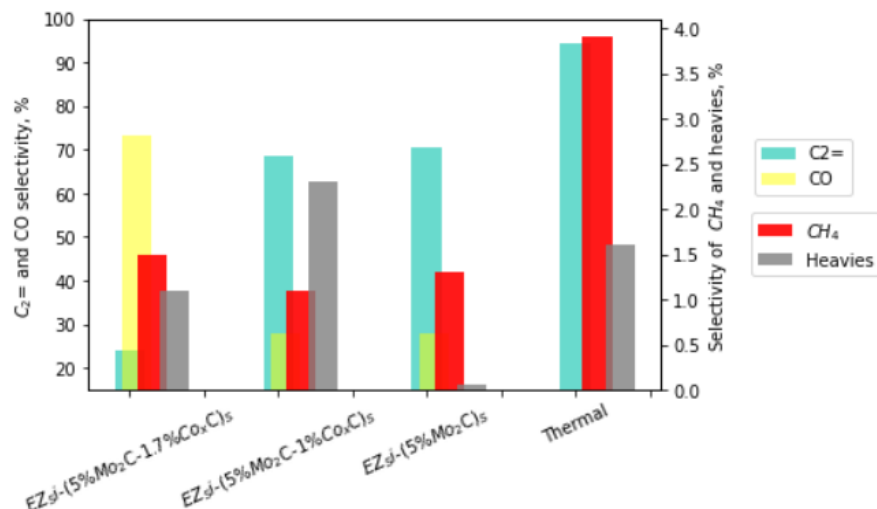


Fig.19- Ethane (C₂) co-processing with CO₂ on EZ_{Si}-(5%Mo₂C-1.7%Co_xC)_S, EZ_{Si}-(5%Mo₂C-1%Co_xC)_S and EZ_{Si}-(5%Mo₂C)_S catalysts and non-catalytic: all C-products selectivity (coke-free basis (T =700 °C, P = 1 atm, C₂H₆/CO₂ = 1/0.74, WHSV=11.8 h⁻¹ for EZ_{Si}-(5%Mo₂C-1%Co_xC)_S, WHSV=5.9 h⁻¹ for EZ_{Si}-(5%Mo₂C)_S).

2.3.6. Impact of the heating rate on the catalyst performances and tests reproducibility

In order to understand the influence of pretreatment, the preheating rate was varied. From 600 °C the heating rate was decreased from 10 °C/min to 3°C/min ('slow activation' mode). The resulting catalyst was tested in the co-processing of ethane and CO₂. The results showed no visible changes neither in the conversion nor in the deactivation. The results also confirmed the good reproducibility of the experiments (**Fig.20**).

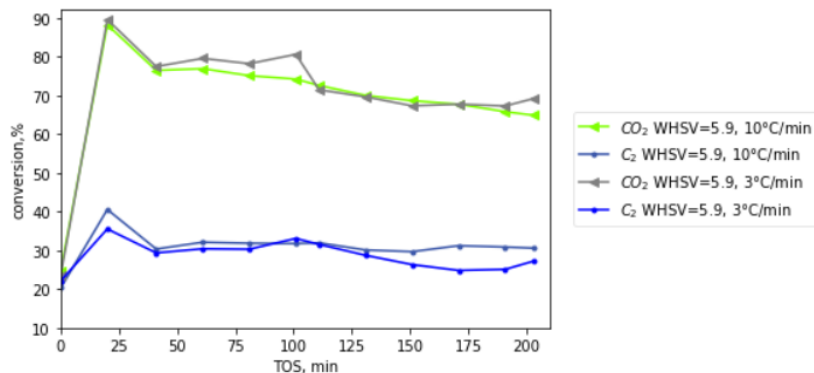


Fig.20- conversion of CO₂ and C₂ as function of time on stream (TOS) on EZ_{Si}-(5%Mo₂C-1%Co_xC)_S: (T =700 °C, P = 1 atm, C₂H₆/CO₂ = 1/0.74).

2.3.7. Oxidic vs. sulfidic bimetallic precursors

In the previous chapter, the behavior of the oxidic and sulfidic precursors for monometallic catalysts was compared. The same approach was applied to Co-Mo systems. At 700 °C the performance of oxide-derived samples was similar to EZ_{Si}-(5%Mo₂C-1%Co_xC)_S. The molar ratio reacted components corresponded ODH-CO₂ selectivity pattern (**Fig.21**). In contrast to the oxidic and sulfidic precursors of the monometallic samples, for the Co-containing system, the difference between various precursors was not significant at 700 °C (**Fig.21**). An exception was the EZ_{Si}-(5%Mo₂C-1.7%Co_xC)_S sample. For ODH-CO₂, the CO₂ conversion varied from 19% to 22% for the samples EZ_{Si}-(5%Mo₂C-1%Co_xC)_S, EZ_{Si}-(5%Mo₂C-1.7%Co_xC)_O, EZ_{Si}-(5%Mo₂C-1%Co_xC)_O.

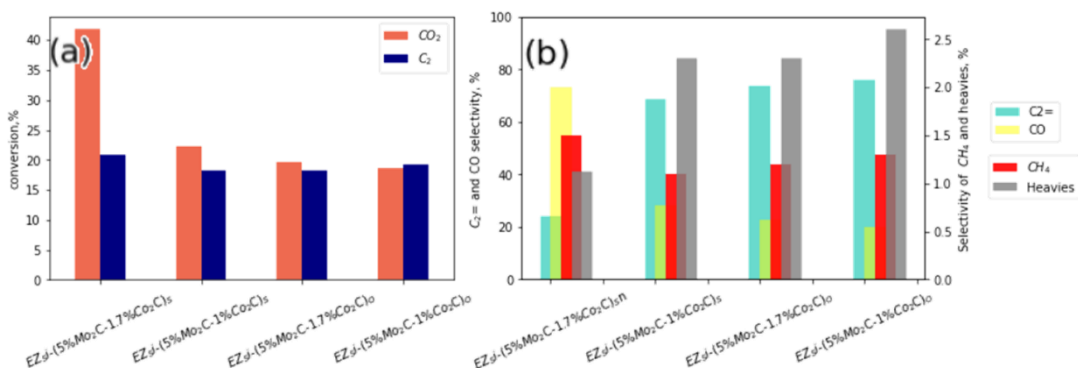


Fig. 21- Ethane (C₂) co-processing with CO₂ on EZ_{Si}-(5%Mo₂C-x%Co_xC)_S and EZ_{Si}-(5%Mo₂C-x%Co_xC)_O catalyst: a) average conversion of CO₂ and ethane; b) all C-products selectivity (coke-free basis, T =700 °C, P = 1 atm, C₂H₆/CO₂ = 1/0.74, WHSV=11.8 h⁻¹).

Ethane conversion differed by less than 1%. Ethylene C₂ products-based selectivity for these samples was at the same level of 95%. The comparison of total carbon products selectivity showed (Fig.21c) that sulfidic precursors improved hydrogenation function. CO selectivity was lower than on EZ_{Si}-(5%Mo₂C-1%Co_xC)_S at 6 and 8% for the EZ_{Si}-(5%Mo₂C-1.7%Co_xC)_S and EZ_{Si}-(5%Mo₂C-1%Co_xC)_S, respectively.

Regarding higher temperatures, one can see that cobalt doping significantly improved the performance of the oxide-derived carbide catalysts. At 750 °C the differences between oxidic and sulfidic-derived samples in CO₂ conversion became more noticeable (Fig.22). It seems that the utilization of the oxidic precursors for the bimetallic catalyst is more advantageous, in particular, if the DRE pathway is targeted (Fig.22). The DRE contribution on EZ_{Si}-(5%Mo₂C-1.7%Co_xC)_O was near 70%.

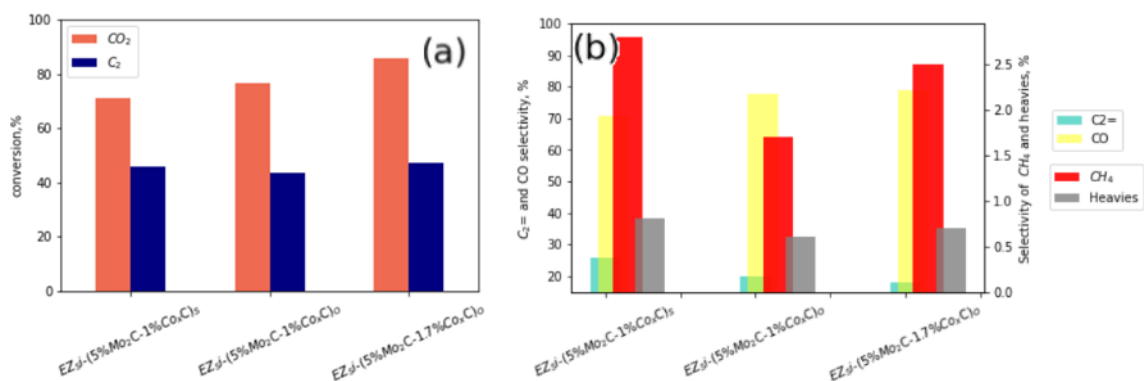


Fig. 22- Ethane (C₂) co-processing with CO₂ on EZ_{Si}-(5%Mo₂C-x%Co_xC)_S and EZ_{Si}-(5%Mo₂C-x%Co_xC)_O catalyst: a) average conversion of CO₂ and ethane; b) all C-products selectivities (coke-free basis, T =750 °C, P = 1 atm, C₂H₆/CO₂ = 1/0.74, WHSV=11.8 h⁻¹).

Co-doped Mo-containing bimetallic samples showed higher activity in comparison to monometallic. The pure Co-samples result in a significant coke formation and in methanation. The content of cobalt significantly impacts performance. The weight ratio Mo/Co of 1 (1.0 wt% of cobalt) showed an improvement in the performance. In contrast, the increase of the cobalt content to 1.7 wt.% for the sample with 5 wt.% of molybdenum resulted in much higher methanation and coking.

The Co-doped Mo-containing samples (Mo/Co weight ratio 1) allow achieving both maximum ethylene production (ODH-CO₂) or maximum CO production (DRE) cases by variation of time of contact.

The results obtained on the oxide- and sulfide-derived carbides strongly depend on the temperature. The oxidic form performs similarly for ODH-CO₂ and is even preferable for dry reforming of CO₂.

3. Study of the spent catalysts

3.1. XRD study

3.1.1. Sulfide-derived catalysts

The effect of cobalt doping on the resistance of catalysts to oxidation or other modification has been studied. Based on the XRD results (**Fig.23**), the stability of Mo₂C species to reoxidation on Co-doped materials in comparison with the results on monometallic systems significantly increased.

The analysis of the formed phases showed mostly the presence of carbon nanotubes (CNT) and Mo₂C. Although the presence of MoO₂ could not be completely excluded, one can neither confirm its presence based on the available diffractogram (**Fig.23**). Typically, peaks at 26, 37.4 characterize the MoO₂ presence, and 53.5°. Well-graphitized multi-wall CNT (MWCNT) show peaks at 26° (002) [27], 42-44° (100) [28,29], 53° (004) and 78° (110). High crystalline β-Mo₂C (Pbcn) shows peaks at 34.3, 38.2, 39.4, 52.2, and 61.7°. The peak at 39.4° is generally the most intensive in the XRD pattern of β-Mo₂C.

Thus, in **Fig.23** for the spent sample (EZ_{Si}-(5%Mo₂C-1%Co_xC)_S) at 700 °C (**Fig.24b**) 2 peaks (34.3 and 39.2 °) were displayed and attributed to β-Mo₂C phase. The peaks at 39, 53 and 62° were attributed to Mo₂C phase. The CNT presence was confirmed by SEM, thus, the peak at 26° could also be attributed to the presence of CNTs in coke depositions (**Fig.24c**).

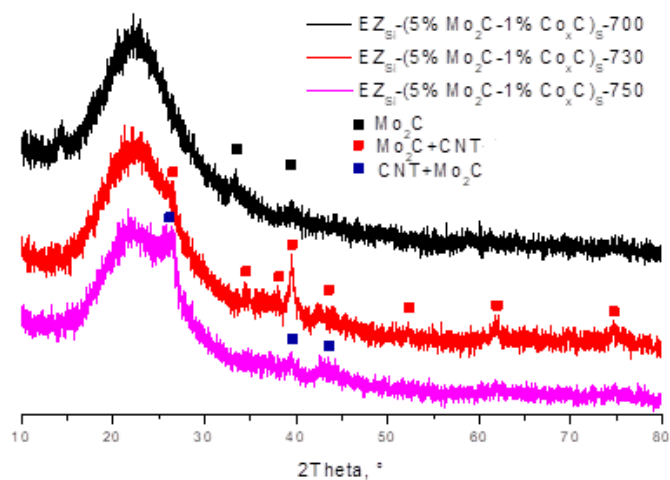


Fig. 23- XRD patterns of spent catalysts at 700-750 °C.

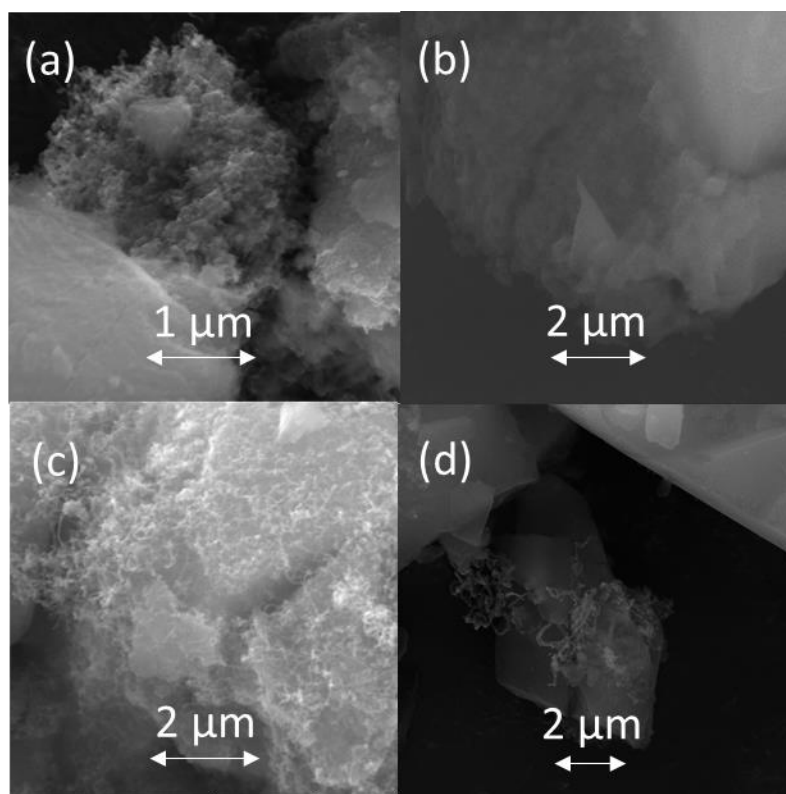


Fig.24- SEM images of the spent samples: (a) $\text{EZ}_{\text{Si}}-(5\%\text{Mo}_2\text{C}-1\% \text{Co}_x\text{C})_{\text{S}}-700$, $\text{WHSV}=5.9 \text{ h}^{-1}$, (b) $\text{EZ}_{\text{Si}}-(5\%\text{Mo}_2\text{C}-1\% \text{Co}_x\text{C})_{\text{S}}-700$, $\text{WHSV}=11.8 \text{ h}^{-1}$, (c) $\text{EZ}_{\text{Si}}-(5\%\text{Mo}_2\text{C}-1\% \text{Co}_x\text{C})_{\text{S}}-750$, $\text{WHSV}=11.8 \text{ h}^{-1}$, (d) $\text{EZ}_{\text{Si}}-(5\%\text{Mo}_2\text{C}-1\% \text{Co}_x\text{C})_{\text{S}}-750$, $\text{WHSV}=17.7 \text{ h}^{-1}$.

The comparing with the Mo-based structure (**Fig.5**), clear evidence of MoO₂ presence was not revealed. Thus, Co doping improved carbide catalyst oxidation resistance. This positive effect appears under both ODH-CO₂ and DRE conditions. The CNT presence at this stage does not lead to the activity decline. The role CNTs in catalysis under the studied conditions is still unclear. The agglomeration by reduction/reoxidation mechanism is much less pronounced for the bimetallic system (**Fig.23**).

In the co-processing of ethane with CO₂, the bimetallic with catalyst Co-doping showed significantly higher carbide phase stability (**Fig. 25**). For the spent (EZ_{Si}-(5%Mo₂C)-1%Co_xC)_S-700, WHSV=11.8 h⁻¹, and EZ_{Si}-(5%Mo₂C)-1%Co_xC)_S-750, WHSV=17.7 h⁻¹, the XRD pattern neither revealed MoO₂ presence, only the carbide phase was present. For the samples tested at lower WHSV with higher carbon deposition, XRD patterns indicated the presence of CNT in addition to the carbide phase (EZ_{Si}-(5%Mo₂C)-1%Co_xC)_S-700, WHSV=5.9 h⁻¹, EZ_{Si}-(5%Mo₂C)-1%Co_xC)_S-750, WHSV=11.8 h⁻¹).

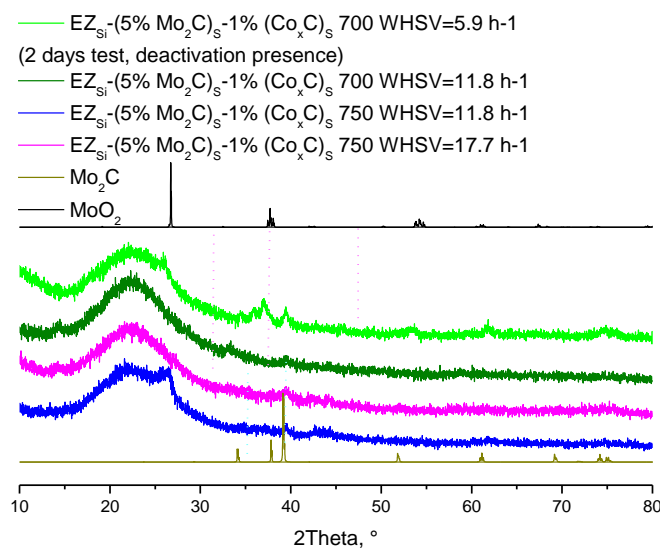


Fig. 25- XRD patterns of spent catalysts at 700-750 °C.

All the studied spent catalysts consisted of amorphous-like embryonic bulky aggregations with minor deposited CNT structures (**Fig.24a, c, d**) or without it (**b**). One can see on SEM images that CNT formation under conditions favoring the reforming pathway (DRE) occurs in higher extent (**Fig.24a, c**). For the tests performed on the bimetallic catalyst under conditions favoring ODH-CO₂, CNT formation was observed only at 750°C or higher (**Fig.24d**).

3.1.2. Oxide-derived catalysts

XRD patterns of the spent catalysts prepared from the oxidic precursors are given in **Fig.26**. For EZ_{Si}-(5%Mo₂C-1%Co_xC)_O tested at 700°C, the presence of a doublet at 35.8 and 37° two theta range were attributed to MoO₂ phase. The same sample treated at 750°C, exhibits broad peaks around 37, 39.7 62, and 74.4 indicating the presence of Mo₂C. A broad asymmetric peak around 43-45° two theta range for both samples tested at 750 °C could be attributed to a cobalt carbide. Mainly, the XRD patterns of all these samples are different from EZ_{Si}-(5%Mo₂C-X%Co_xC)_S due to the absence of an intense peak at 26°. At the same time, a comparison of SEM micrographs for samples tested at 750 °C showed an intensive formation of CNT on the surface of the oxide-derived samples (**Fig.27**).

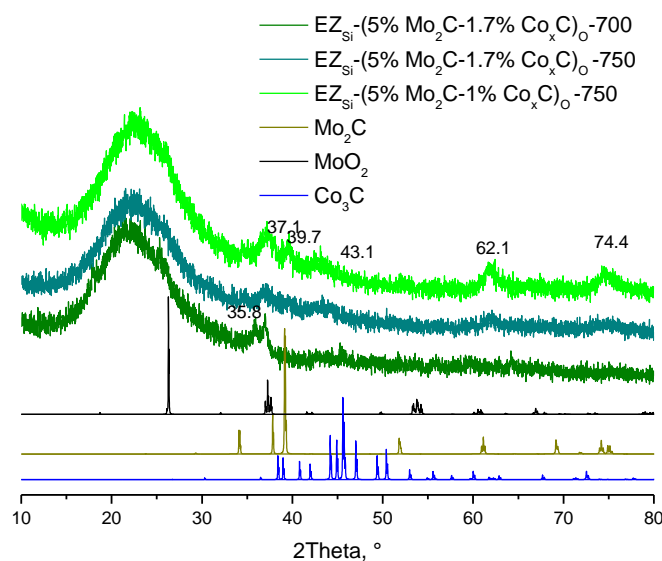


Fig. 26- XRD patterns of spent catalysts at 700-750 °C (oxidic precursors).

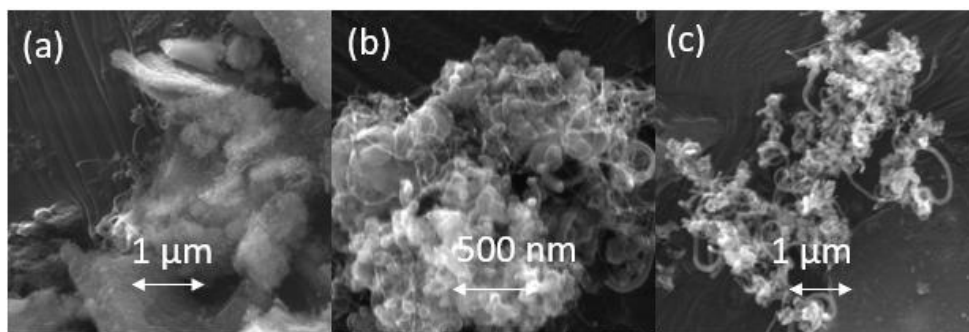


Fig.27- SEM images of the spent samples: (a) EZ_{Si}-(5%Mo₂C-1.7% Co_xC)_O-700, (b) EZ_{Si}-(5%Mo₂C-1.7% Co_xC)_O-750, (c) EZ_{Si}-(5%Mo₂C-1% Co_xC)_O-750, WHSV=11.8 h⁻¹.

3.2. Raman characterization

Raman spectroscopy could be useful for analyzing carbon-rich materials. Typically, the presence of RBM (Radial Breathing Mode), D, and G bands in the Raman spectrum allows confirming the presence of carbon nanotubes [30]. However, given the previous results for monometallic samples, the data may be distorted in the presence of coke. The difference between the D-G bands from carbon deposition on the catalyst and from CNT could not be made by the D-G bands' character. The bands may overlap and mask the information [30]. The spectrum of CNTs with some fillers may look similar to the coke deposition on the catalyst. [28,31]. Asymmetrical and overlapped G band for CNT structures may be due to defects [32]. Therefore, even an approximate estimate of the presence of coke in the presence of nanotubes is difficult. In the spectra of the spent samples, no RBM bands were observed, so it was not possible to confirm by Raman the presence of the nanotubes (**Fig. 28**).

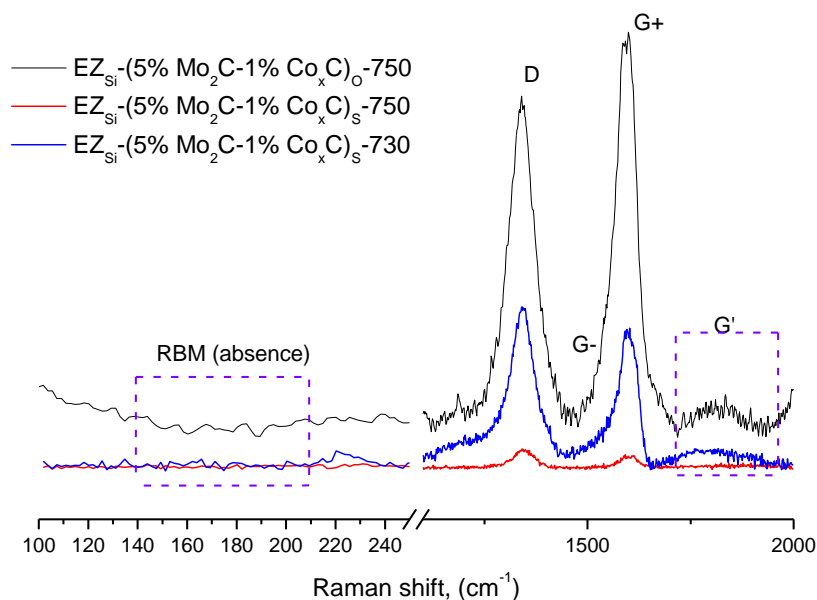


Fig. 28- Raman spectra of spent samples at 730-750 °C with the confirmed presence of the CNT by SEM.

3.3. Thermogravimetric characterization

The catalysts were tested at different temperatures, and at different reaction conditions to maximize ethylene or CO production, (ODH-CO₂ and DRE). All spent catalysts were characterized by thermogravimetric analysis.

The first weight loss in the TGA profiles (**Fig. 29**) from room temperature to 120 °C is due to the desorption of adsorbed moisture from the atmosphere. A following slight weight increase to 470 °C is specific for the oxidation reaction of Mo₂C to MoO₃. For samples tested at 700 °C, no high-temperature weight loss was detected. Based on that, one can conclude that almost no coke was formed at this temperature. The TG curves of the samples tested at 730 and 750 °C had the same shape as for EZ_{Si}-(5%Mo₂C)_S (**Fig. 29**). The final weight loss that started around 480 °C, could be attributed to the burning-off of the hard coke, which was deposited during the reaction and the formation of CNTs. The weight loss was increased with the increase of the temperature of the catalytic test.

A comparison of monometallic and bimetallic samples was performed (**Fig.30**). Moisture desorption, carbide oxidation, and coke combustion were detected (EZ_{Si}-(5%Mo₂C)_S). The weight losses for EZ_{Si}-(5%Mo₂C)_S-700 and EZ_{Si}-(5%Mo₂C)_S-750 were at the same level. However, for bimetallic samples tested at the same temperatures, the difference between them was about 14% (EZ_{Si}-(5%Mo₂C-1%Co_xC)_S-700 and EZ_{Si}-(5%Mo₂C-1%Co_xC)_S-750).

The TGA curves measured for EZ_{Si}-(5%Mo₂C-1%Co_xC)_S tested under conditions favorable for ethylene production (ODH-CO₂) and on the conditions maximizing CO yield (DRE) at various temperatures were compared (**Fig.31**). The total weight decreases for samples operated under DRE was much higher than for the one under ODH-CO₂. The difference is mainly due to a higher amount of hard coke formation.

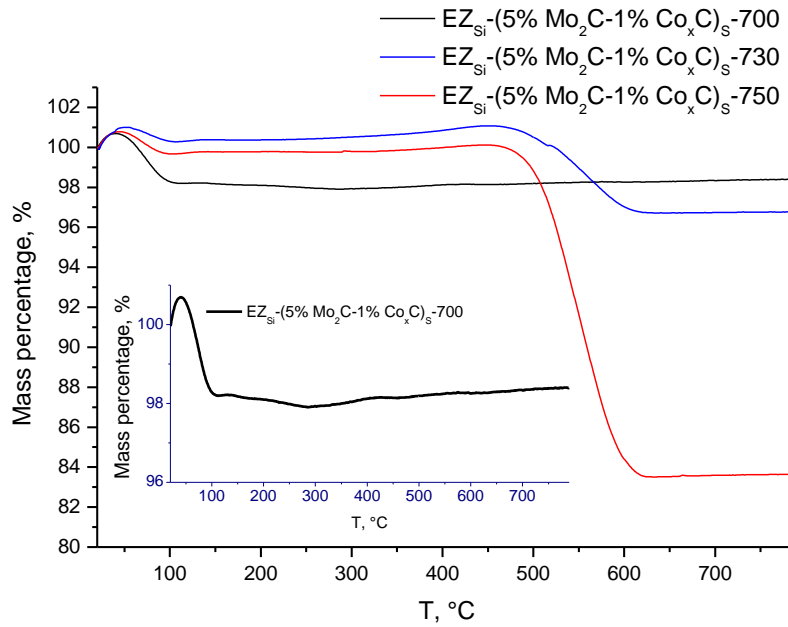


Fig. 29- Thermogravimetric analysis of spent EZ_{Si}-(5%Mo₂C-1%Co_xC)_S at 700, 730 and 750 °C with air.

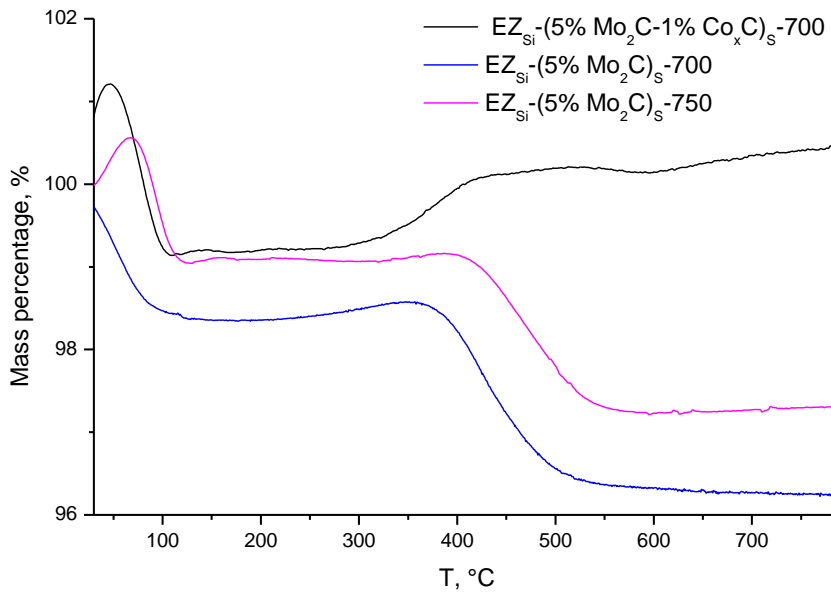


Fig. 30- Thermogravimetric analysis of spent EZ_{Si}-(5%Mo₂C-1%Co_xC)_S at 700 and EZ_{Si}-(5%Mo₂C)_S at 700 and 750 °C with air.

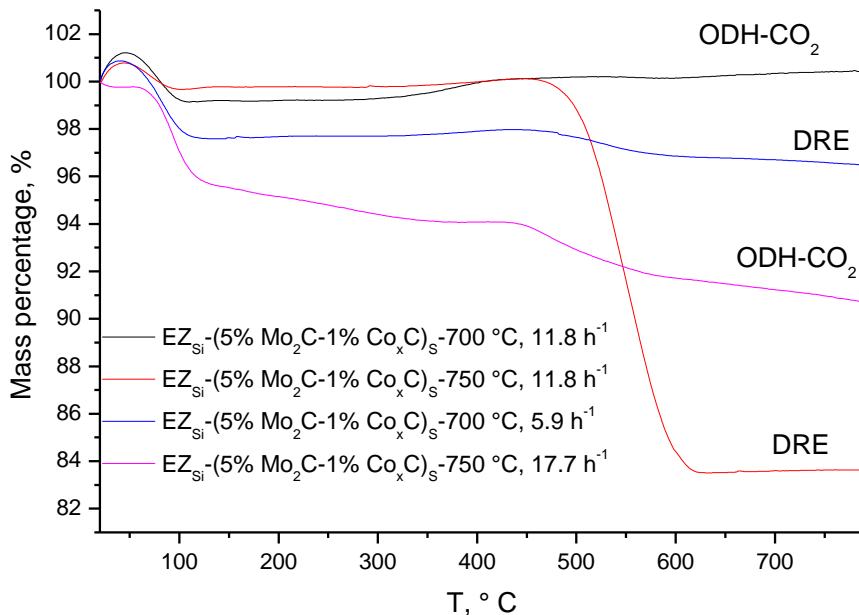


Fig. 31- Thermogravimetric analysis of spent EZ_{Si}-(5%Mo₂C-1%Co_xC)_S under DRE and ODH-CO₂ conditions.

4. Conclusions

We characterized and analyzed various types of Mo₂C-based catalytic systems which were further tested in RWGS, ODH-CO₂, DRE. Different structural changes occurred with the catalytic systems depending on the testing mode.

Monometallic Mo-sulfide precursors remain unchangeable in CO₂ hydrogenation (RWGS) up to 800 °C. No visible phase agglomeration occurs. In the presence of hydrocarbons, the sulfides are gradually transformed to the well-dispersed Mo-carbide phase. The Mo-carbide particles obtained from sulfide precursor are smaller than from the corresponding oxide, which explains the higher activity of the materials obtained from MoS₂ in the ODH-CO₂ of ethane.

The utilization of Mo-containing monometallic samples obtained from sulfide-precursor in the co-processing of CO₂ and ethane in the temperature range between 700 and 800 °C avoids the dry reforming of ethane and co-produce produce ethylene and CO via the ODH-CO₂ route. By optimization of the preparation procedure, a 10% gain in the conversion of CO₂ was achieved on EZ_{Si}-(5%Mo₂C)_S-HT sample. , the increase of activity is hampered by the reoxidation of the carbide phase to MoO₂, which is inactive in the hydrogenation of CO₂. The reoxidation to the MoO₂ phase,

followed by agglomeration, is the main reason for the irreversible deactivation of this catalyst. A fraction of molybdenum is present as MoO₂ and does not participate in the catalytic reaction. Therefore, the reoxidation process is very undesirable for this catalyst. Both, reoxidation to oxide and carburization to carbide routes are accelerated with the raise of the temperature. Moreover, at 800 °C, the Mo₂C phase largely dominates, which explains the catalyst's highest activity in CO₂ hydrogenation at this temperature. However, the catalyst stability is not high at this maximal tested temperature. On the other hand, a higher loading of the Mo-active phase further increases the catalyst activity. A significant optimization potential remains at higher Mo-loading for this system.

Co-doping dramatically changes the catalyst performance and boosts activity. The fundamental change is that Co-doping protects the Mo-carbide from reoxidation to the oxide phase. That makes the utilization of the Mo-phase much more efficient and boosts the activity of the catalyst. Even a small amount of cobalt on the catalyst is sufficient to achieve this effect.

In contrast to the monometallic materials, the use of sulfidic precursors does not show benefits for the Co-doped bimetallic catalyst. This means that the Co-species also play a facilitating role in forming the carbide phase while preventing agglomeration.

At the same time, the pure Co-containing catalyst leads to the methanation of CO₂ and fast coking of the catalyst. Hence, if the cobalt content is too high, there is a risk of formation of the individual non-bounded with molybdenum Co-species, which are highly undesirable for catalysis.

In conclusion, Co-doping has a dramatic impact on the catalyst performance in ethane and CO₂ conversion. At low Co-content (Mo/Co weight ratio ~ 5), the CO₂ conversion was two times higher on EZ_{Si}-(5%Mo₂C-1%Co_xC)_S in comparison with EZ_{Si}-(5%Mo₂C)_S at the similar conversion of ethane. Furthermore, the Co-doped material may drive selectivity to both routes: olefins maximization (ODH-CO₂) and dry reforming of ethane.

The regulation between DRE and ODH-CO₂ could be performed by adjustment of operating conditions on the same catalyst. Increasing the WHSV (decreasing the contact time) leads to a higher contribution of the ODH-route for ethylene production while reducing WHSV results in the ethane transformation mainly via the DRE-route for CO production. The obtained

experimental data are consistent with the literature on this aspect. The advantage of our catalysts is the expansion of the temperature range for the use of carbides.

The application of sulfidic precursors for Mo or Mo-Co carbide catalysts may result in a new type of catalyst for dry methane reforming, superdry methane reforming, ODH-CO₂, and dry ethane reforming.

References

- [1] WorldEnergyOutlook 2021, International Energy Agency report, (n.d.). <https://www.iea.org/reports/world-energy-outlook-2021>.
- [2] The Future of Petrochemicals 2021, International Energy Agency report, (n.d.). <https://www.iea.org/reports/the-future-of-petrochemicals>.
- [3] G. Li, C. Liu, X. Cui, Y. Yang, F. Shi, Oxidative dehydrogenation of light alkanes with carbon dioxide, *Green Chem.* 23 (2021) 689–707. <https://doi.org/10.1039/D0GC03705B>.
- [4] W. Marquart, M. Claeys, N. Fischer, Conversion of CO₂ and small alkanes to platform chemicals over Mo₂C-based catalysts, *Faraday Discuss.* 230 (2021) 68–86. <https://doi.org/10.1039/D0FD00138D>.
- [5] E. Gomez, B. Yan, S. Kattel, J.G. Chen, Carbon dioxide reduction in tandem with light-alkane dehydrogenation, *Nat Rev Chem.* 3 (2019) 638–649. <https://doi.org/10.1038/s41570-019-0128-9>.
- [6] S. Yao, B. Yan, Z. Jiang, Z. Liu, Q. Wu, J.H. Lee, J.G. Chen, Combining CO₂ Reduction with Ethane Oxidative Dehydrogenation by Oxygen-Modification of Molybdenum Carbide, *ACS Catal.* 8 (2018) 5374–5381. <https://doi.org/10.1021/acscatal.8b00541>.
- [7] F. Solymosi, R. Nemeth, The oxidative dehydrogenation of ethane with CO₂ over Mo₂C/SiO₂ catalyst, *Cat Lett.* 62 (1999) 197–200.
- [8] W.-J. Jang, J.-O. Shim, H.-M. Kim, S.-Y. Yoo, H.-S. Roh, A review on dry reforming of methane in aspect of catalytic properties, *Catalysis Today.* 324 (2019) 15–26. <https://doi.org/10.1016/j.cattod.2018.07.032>.
- [9] ECO STAR 36K Liquefied Ethylene Gas Carrier, (2017). <https://www.ship-technology.com/projects/eco-star-36k-liquefied-ethylene-gas-carrier/>.
- [10] L.C. Buelens, V.V. Galvita, H. Poelman, C. Detavernier, G.B. Marin, Super-dry reforming of methane intensifies CO₂ utilization via Le Chateliers principle, *Science.* 354 (2016) 449–452. <https://doi.org/10.1126/science.aah7161>.
- [11] J. Huang, T. Huang, L. Liu, W. Huang, R. Ma, Mo₂C/SBA-15 Modified by Ni for the Dry Reforming of Methane, *Energy Sources, Part A: Recovery, Utilization, and Environmental Effects.* 33 (2011) 2249–2256. <https://doi.org/10.1080/15567036.2010.543999>.
- [12] T. Zhang, Z.-C. Liu, Y.-C. Ye, Y. Wang, H.-Q. Yang, H.-X. Gao, W.-M. Yang, Dry reforming of ethane over FeNi/Al–Ce–O catalysts: Composition-induced strong metal-support interactions, *Engineering.* (2022) S2095809922003708. <https://doi.org/10.1016/j.eng.2021.11.027>.
- [13] S. Kattel, J.G. Chen, P. Liu, Mechanistic study of dry reforming of ethane by CO₂ on a bimetallic PtNi(111) model surface, *Catal. Sci. Technol.* 8 (2018) 3748–3758. <https://doi.org/10.1039/C8CY00880A>.
- [14] J. Jeon, Y. Park, S. Choi, J. Lee, S.S. Lim, B.H. Lee, Y.J. Song, J.H. Cho, Y.H. Jang, S. Lee, Epitaxial Synthesis of Molybdenum Carbide and Formation of a Mo₂C/MoS₂ Hybrid Structure via Chemical Conversion of Molybdenum Disulfide, *ACS Nano.* 12 (2018) 338–346. <https://doi.org/10.1021/acsnano.7b06417>.

- [15] T. Xiao, A.P.E. York, K.S. Coleman, J.B. Claridge, J. Sloan, J. Chanrock, M.L.H. Green, Effect of carburising agent on the structure of molybdenum carbides, *Journal of Materials Chemistry*. (2001) 3094–3098. <https://doi.org/doi-org.inc.bib.cnrs.fr/10.1039/B104011C>.
- [16] T. Mo, J. Xu, Y. Yang, Y. Li, Effect of carburization protocols on molybdenum carbide synthesis and study on its performance in CO hydrogenation, *Catalysis Today*. 261 (2016) 101–115. <https://doi.org/10.1016/j.cattod.2015.07.014>.
- [17] Q. Bkour, C.M. Cuba-Torres, O.G. Marin-Flores, S. Tripathi, N. Ravishankar, M.G. Norton, S. Ha, Mechanistic study of the reduction of MoO₂ to Mo₂C under methane pulse conditions, *J Mater Sci*. 53 (2018) 12816–12827. <https://doi.org/10.1007/s10853-018-2549-0>.
- [18] J. Dang, G. Zhang, L. Wang, K. Chou, P.C. Pistorius, Study on Reduction of MoO₂ Powders with CO to Produce Mo₂C, *J. Am. Ceram. Soc.* 99 (2016) 819–824. <https://doi.org/10.1111/jace.14042>.
- [19] M.D. Porosoff, M.N.Z. Myint, S. Kattel, Z. Xie, E. Gomez, P. Liu, J.G. Chen, Identifying Different Types of Catalysts for CO₂ Reduction by Ethane through Dry Reforming and Oxidative Dehydrogenation, *Angew. Chem. Int. Ed.* 54 (2015) 15501–15505. <https://doi.org/10.1002/anie.201508128>.
- [20] S. Hu, C. Melton, D. Mukherjee, A facile route for the synthesis of nanostructured oxides and hydroxides of cobalt using laser ablation synthesis in solution (LASIS), *Phys. Chem. Chem. Phys.* 16 (2014) 24034–24044. <https://doi.org/10.1039/C4CP03018D>.
- [21] A. Christodoulakis, E. Heracleous, A. Lemonidou, S. Boghosian, An operando Raman study of structure and reactivity of alumina-supported molybdenum oxide catalysts for the oxidative dehydrogenation of ethane, *Journal of Catalysis*. 242 (2006) 16–25. <https://doi.org/10.1016/j.jcat.2006.05.024>.
- [22] E. Dominguez Garcia, J. Chen, E. Oliviero, L. Oliviero, F. Maugé, New insight into the support effect on HDS catalysts: evidence for the role of Mo-support interaction on the MoS₂ slab morphology, *Applied Catalysis B: Environmental*. 260 (2020) 117975. <https://doi.org/10.1016/j.apcatb.2019.117975>.
- [23] Y. Yao, K. Ao, P. Lv, Q. Wei, MoS₂ Coexisting in 1T and 2H Phases Synthesized by Common Hydrothermal Method for Hydrogen Evolution Reaction, *Nanomaterials*. 9 (2019). <https://doi.org/10.3390/nano9060844>.
- [24] N.H. Attanayake, A.C. Thenuwara, A. Patra, Y.V. Aulin, T.M. Tran, H. Chakraborty, E. Borguet, M.L. Klein, J.P. Perdew, D.R. Strongin, Effect of Intercalated Metals on the Electrocatalytic Activity of 1T-MoS₂ for the Hydrogen Evolution Reaction, *ACS Energy Lett.* 3 (2018) 7–13. <https://doi.org/10.1021/acsenerylett.7b00865>.
- [25] L. Zhu, D. Susac, M. Teo, K. Wong, P. Wong, R. Parsons, D. Bizzotto, K. Mitchell, S. Campbell, Investigation of CoS₂-based thin films as model catalysts for the oxygen reduction reaction, *Journal of Catalysis*. 258 (2008) 235–242. <https://doi.org/10.1016/j.jcat.2008.06.016>.
- [26] V. Bikbaeva, N. Nesterenko, S. Konnov, T.-S. Nguyen, J.-P. Gilson, V. Valtchev, A low carbon route to ethylene: Ethane oxidative dehydrogenation with CO₂ on embryonic zeolite supported Mo-carbide catalyst, *Applied Catalysis B: Environmental*. 320 (2023) 122011. <https://doi.org/10.1016/j.apcatb.2022.122011>.
- [27] A. Saravanan, K. Prasad, N. Gokulakrishnan, R. Kalaivani, T. Somanathan, Efficiency of Transition Metals in Combustion Catalyst for High Yield Helical Multi-Walled Carbon

- Nanotubes, *Adv Sci Engng Med.* 6 (2014) 809–813. <https://doi.org/10.1166/ asem.2014.1569>.
- [28] R. Atchudan, A. Pandurangan, J. Joo, Effects of Nanofillers on the Thermo-Mechanical Properties and Chemical Resistivity of Epoxy Nanocomposites, *J Nanosci Nanotechnol.* 15 (2015) 4255–4267. <https://doi.org/10.1166/ jnn.2015.9706>.
- [29] R. Atchudan, A. Pandurangan, The use of bimetallic MCM-41 mesoporous catalysts for the synthesis of MWCNTs by chemical vapor deposition, *Journal of Molecular Catalysis A: Chemical.* 355 (2012) 75–84. <https://doi.org/10.1016/ j.molcata.2011.11.028>.
- [30] N. Souza, F. Lasserre, A. Blickley, M. Zeiger, S. Suárez, M. Duarte, V. Presser, F. Mücklich, Upcycling spent petroleum cracking catalyst: pulsed laser deposition of single-wall carbon nanotubes and silica nanowires, *RSC Adv.* 6 (2016) 72596–72606. <https://doi.org/10.1039/ C6RA15479D>.
- [31] N. Xu, S.H. Tsang, B.K. Tay, E.H.T. Teo, C.M. Ng, Growth of Carbon Nanotubes on Carbon/Cobalt Films with Different sp² /sp³ Ratios, *Journal of Nanomaterials.* 2013 (2013) 1–5. <https://doi.org/10.1155/2013/730952>.
- [32] A. Jorio, R. Saito, Raman spectroscopy for carbon nanotube applications, *Journal of Applied Physics.* 129 (2021) 021102. <https://doi.org/10.1063/5.0030809>.

**Chapter 6. Ethane Oxidative
Dehydrogenation with CO₂ on
thiogallates**

1. Introduction

Expansion in chemicals is one of the upcoming trends in the transformation of the petrochemical industry, and ethane transformation is an important part of the downstream evolution. A significant portion of the recent investments in olefins was in gas-based petrochemistry, either in ethane steam cracking (ethylene production) or in propane dehydrogenation (propylene production). The transition is a part of the efforts to transform “a fuel refinery” into the “refinery of the future [1]. However, the CO₂ emissions of a refinery of future per ton of olefins are significantly higher than traditional petrochemical production because the feedstock is produced on purpose via several hydrotreatment steps. Thus, an increase in the amount of chemicals production at a refinery from 10% to 25-40% may almost double the carbon footprint (CO₂/ton) from 1-1.5 to 2.4 -2.6 [2]. Consequently, high carbon footprint is not acceptable given the zero carbon emission target in the industry. In addition, the technologies to produce fossil products are less and less attractive for investors unless the production is low carbon. Thus, the downstream sector needs to rethink how olefins will be produced in the future. Among the options to decarbonize the production of chemicals, a combination of olefins production with CO₂ utilization is an important topic for the next decades in the quest for the downstream industry transformation. This approach may even lead to a carbon-negative technology for olefins production from the fossil feedstock.

The idea is to directly use the hydrogen produced as a by-product by the processes or benefit from the heat of the process with a low carbon/green H₂ co-feeding. This perspective requires the development of a new catalyst, which could selectively hydrogenate CO₂ in the presence of hydrocarbons. Metal sulfides are known for CO₂ hydrogenation to high-value products, such as methanol, dimethyl ether, CH₄, light alkenes, jet fuel, or CO. The MoS₂-based catalyst showed promising results in CO₂ methanation and methanol synthesis. For example, Hu et al [3]. investigated the ODH-CO₂ with MoS₂ at 50 atm, 300 °C; this system obtained MeOH with 94.3% selectivity. Primo et al [4]. applied oriented MoS₂ nanoplatelets at 10 atm at 300-600 °C for the CO₂ methanation with the 100% key product selectivity. ZnS was used for the direct non-oxidative dehydrogenation of ethane at 550 °C, showing about 10% of conversion [5]. However,

these materials are not sufficiently stable at high temperatures (above 700 °C), where ethane conversion per pass could reach a significant level. Thus, up to now, there is not any report on the utilization of metal sulfides for ODH-CO₂.

Catalytic behavior of sulfur-free gallium-containing systems in ethane dehydrogenation and CO₂-assisted oxidative ethane dehydrogenation was also studied [6-7]. A significant influence of the nature of the substrate on the deactivation of Ga-containing catalysts in the ODH-CO₂ has been reported [8]. The samples exhibited low tolerance to coke formation. Most of the studies of ethane dehydrogenation on Ga-containing materials demonstrated the selectivity to ethene >90% with the low amount of the aromatic fraction [9]. Zeolites (HZSM-5 [6], HSSZ-13 [9]) and oxides (TiO₂ [10], Al₂O₃ [11,12]) were used as carriers of the Ga-containing active phase. However, for CO₂-assisted reactions on these catalytic systems, only the results at low conversion were reported. The conversion was about 10% over Ga/TiO₂ [10] at 700 °C, and only 3.2% over FeGa@ZSM-5 [13] at 600 °C. The performance of unsupported Ga-containing materials is still seldom reported in the literature.

Alkali ternary thiogallates are one of the varieties of the unsupported Ga-containing materials. They exist in several structure types. The most known and the most well-studied is AGaS₂ (A=Na [14], Cs [15], Ag [16-18]) family of materials. Several novel members in this family, Na₆Ga₂S₆ [19] and A₅GaS₄ (A=Li, Na) [20], were recently discovered.

A standard protocol for synthesizing the various ternary A_xGaS_y materials involves heating to 650-800 °C for several hours in the sealed quartz ampoule [14,20]. A few studies report the low-temperature synthesis route to alkali-containing ternary thiogallates, which is more advantageous for industrialization. For instance, AgGaS₂ [18] was obtained at 300 °C under the N₂ atmosphere in the presence of oleates. The first solvothermal synthesis of AgGaS₂ was reported by J. Hu et al [17]. Tetragonal crystals (a = 5.7538 Å, c = 10.3026 Å) with the size of 5 – 12 nm were prepared using ethylenediamine as solvent and template at the same time at 180-230 °C for 10 h. Nanoflowers with similar composition (AgGaS₂) and the tetragonal unit cell (I-42d space group, a=5.76 Å and c=10.3 Å) were described by Yuan et al [21]. The nanocrystalline tetragonal phase (a = 5.523 Å, c = 11.141 Å) CuGaS₂ was also synthesized by a solvothermal approach by Lu et al. [22]. In contrast, the literature is silent about a solvothermal crystallization of AGaS₂ (A=K,

Na, Cs) in monoclinic configuration. Up to now, the monoclinic structure of KGaS₂ [23,24], NaGaS₂ [14], CsGaS₂ as well as Cs₂Ga₂S₅ [25] were obtained only by solid-state reaction at 600-900 °C.

The alkali thiogallates, e.g., AgGaS₂, are known for their photocatalytic activities [26,27]. For instance, Lee and al. studied the photocatalytic activity of AgGaS₂ nanoparticles in H₂S splitting reaction to produce hydrogen [26]. The same group also reported the utilization of AgGaS₂-type photocatalyst for H₂ production from water [28]. Besides the photocatalytic activity, a distinctive feature of the alkali thiogallates is their exceptional thermal stability (800-900 °C) which is not very common for Ga-containing materials. Another advantage of these compounds is their potentially high coking resistance thanks to the sulfur present in the structure and their moderate hydrogenation activity. Hence, we considered these materials as potentially a promising catalytic system for the ethane ODH-CO₂ reaction.

For many metals, such as Mo and Fe, a transformation to the carbide phase occurs over 700 °C under a hydrocarbon environment [29,30]. In contrast, gallium carbide would not be formed under these conditions, which is also one more reason to focus on the alkali thiogallates. The alkali ternary thiogallates will remain in their initial state while preventing the reduction of gallium to the individual metal. These systems as catalysts for ethane oxidative dehydrogenation with CO₂ have never been reported.

The present study reports the synthesis of monoclinic potassium ternary thiogallate (KGaS₂) and its application in ODH-CO₂ of ethane.

2. Results and discussion

2.1. Synthesis and characterization of the catalysts

In the presence of amines, the crystallization of gallium sulfides may occur in different pathways. The synthesis usually results in octahedral clusters, e.g., Na₅(Ga₄S)(GaS₄)₃·6H₂O [31], anionic layers, e.g. [Ga₄S₇(en)₂] [32] with gallium atoms trigonal-pyramidally coordinated by sulfur, or [GaS₂]⁻ layers, e.g., NaGaS₂ [14]. In this contribution, we focused on a solvothermal synthesis of thiogallates with ethylenediamine and 1-2-(aminoethyl)piperazine. In the absence of the potassium cation, the preparation resulted in the amorphous phase with AEP and the non-defined low crystalline phase of gallium sulfide with EDA (**Fig.1**). Representative SEM images of

obtained solids are shown in **Fig. 2**. The presence of inorganic cations, e.g., potassium, plays the role of a structural directing agent and drives the formation of a well-crystallized material (**Fig.1**). The resulted thiogallate, synthesized with potassium and EDA, was determined as KGaS₂.

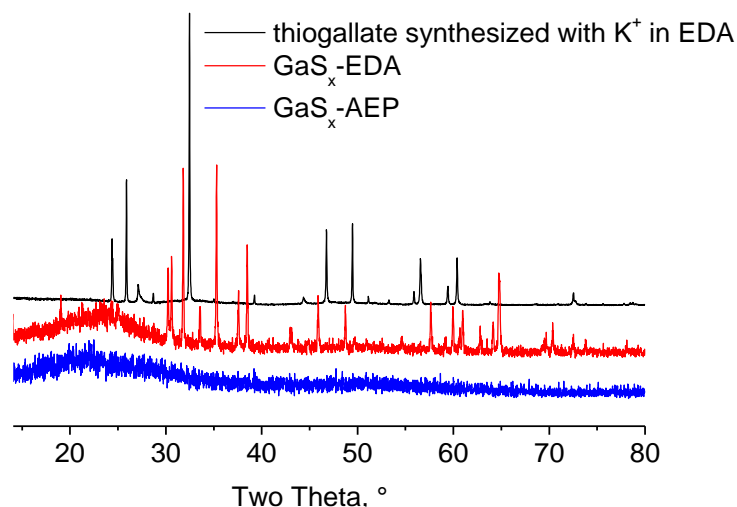


Fig. 1- PXRD patterns of the obtained phases in presence or absence of alkali cations with organic templates (EDA, AEP).

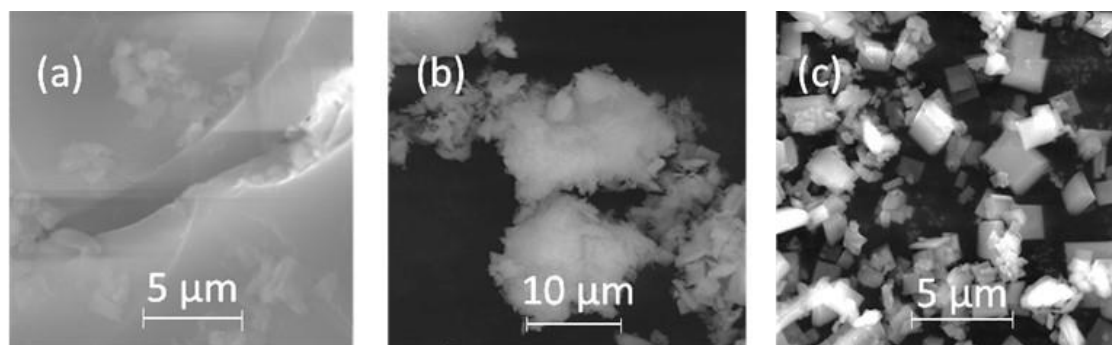


Fig. 2- SEM micrographs of the solids obtained at 190 °C for 7d from (a) Ga-S-AEP, (b) Ga-S-EDA systems, (c) Ga-S-EDA with K⁺.

The powder X-ray diffraction (PXRD) patterns of the obtained product powder showed patterns similar to NaGaS₂ and K_{0.56}Na_{0.44}GaS₂.¹⁴ The ICSD structure of KGaS₂ published in the Inorganic Crystal Structure Database (ICSD collection code 107928) is questionable; indeed, it refers to Delgado's study [33], the object of which is the analysis of the compound TlGaSe₂. To make a proper analysis of our PXRD patterns, the profile matching has been performed on the

basis of two previously reported structural analysis of KGaS₂. A first structure solution of KGaS₂ using single crystal data resulted in the non-centrosymmetric space group Aa [34] ($a=14.721(5)$ Å, $b=10.425(3)$ Å, $c=10.424(2)$ Å, $\gamma=100.16(2)^\circ$). By analogy with compounds TlGaSe₂ and NaGaS₂ compounds, a PXRD study proposes a new description in the centrosymmetric monoclinic space group C2/c ($a=10.4136(2)$ Å, $b=10.4143(2)$ Å, $c=14.7866(2)$ Å, $\beta = 100.165(2)^\circ$) [23]. The result of the pattern matching analyses performed using Jana2006[35], using these two references clearly indicates the purity and the quality of the different synthesized KGaS₂ samples (refined cell parameters: $a=10.417(3)$ Å, $b=10.399(3)$ Å, $c=14.788(4)$ Å, $\beta = 100.129(3)^\circ$) (**Fig. 3**).

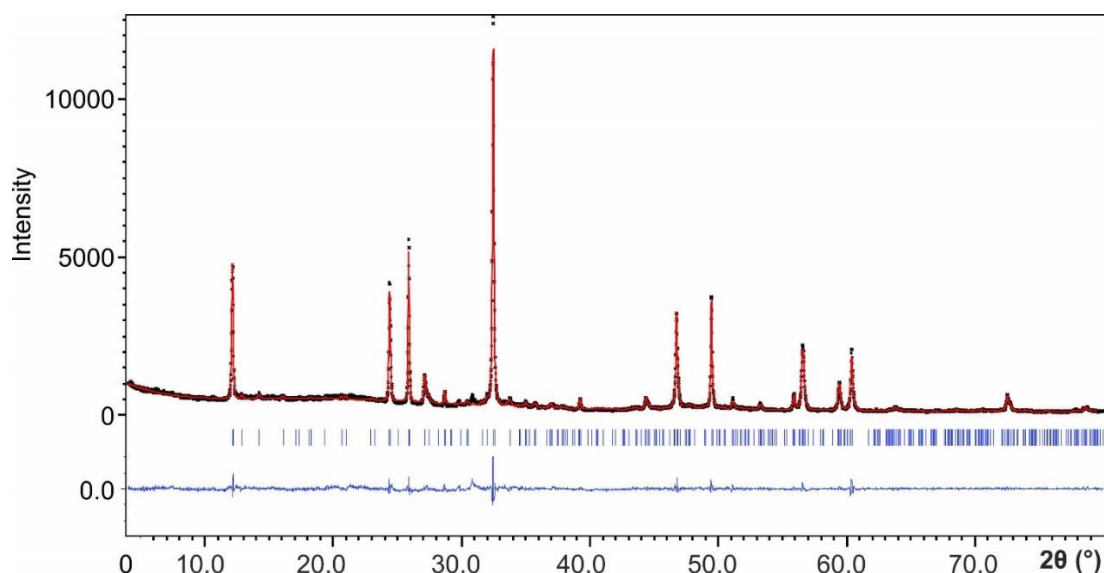


Fig. 3- PXRD patterns of as-prepared KGaS₂ with EDA attesting of the sample purity. Cross symbol is the observed signal, red line is the calculated signal, blue segments show the position of the expected reflections, blue line the differences between observed and calculated intensities.

The obtained KGaS₂ with EDA crystals are 1-2 μm large with a plate-like rectangular shape (**Fig.4a**). For AEP-templated thiogallates, the obtained crystallites were the same size and morphology, as the particles are highly agglomerated (**Fig.4b**).

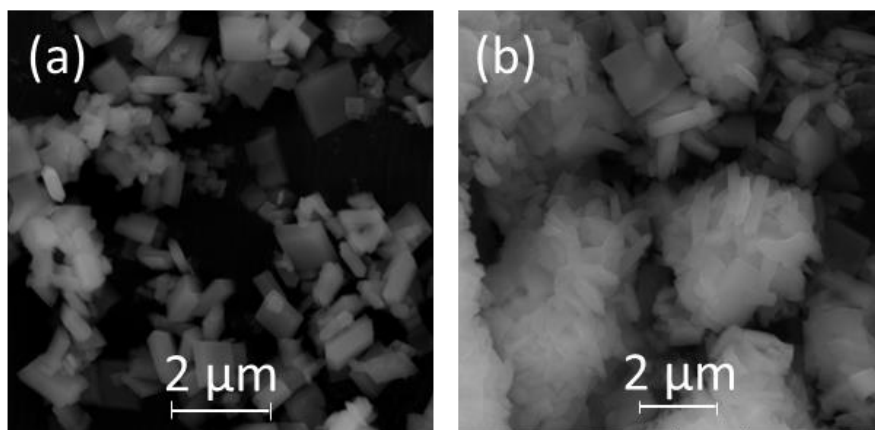


Fig.4- SEM images of KGaS₂ synthesized with EDA (a) and AEP (b).

The EDS mapping of EDA-synthesized KGaS₂ crystals showed a uniform distribution of all elements (**Fig.5**). According to the EDS analysis, the molar ratio K: Ga: S ratio is 1: 1: 1.9 (**Fig.6**). A similar S/Ga ratio (below 2) was reported in earlier studies for the alkali-containing thiogallates obtained by solid-state high-temperature synthesis [14,36].

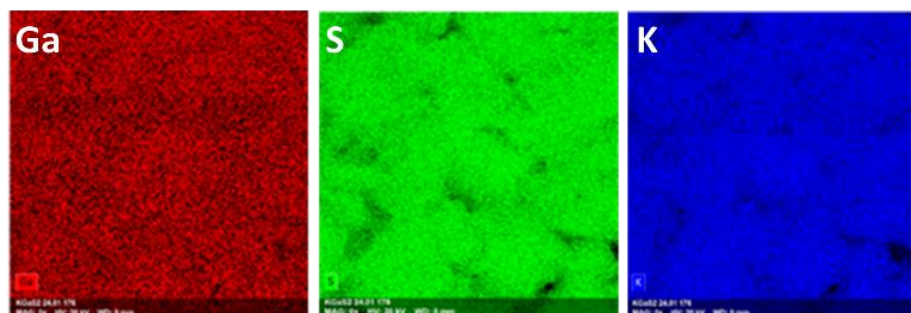


Fig.5- EDS elemental distribution in KGaS₂ (EDA, 4d, 190 °C).

The collected UV-Vis spectra of KGaS₂ were identical to the NaGaS₂ spectra reported by V. Klepov et al. [14] (**Fig. 7**). The accumulated spectrum showed a curve with the characteristic intense peak at 280 nm and the two weak peaks between 330-470 nm. The specific surface area of the EDA-synthesized KGaS₂ determined by N₂ physisorption was 12 cm²g⁻¹, which is a typical value for the non-porous material with a size of about 1 μm.

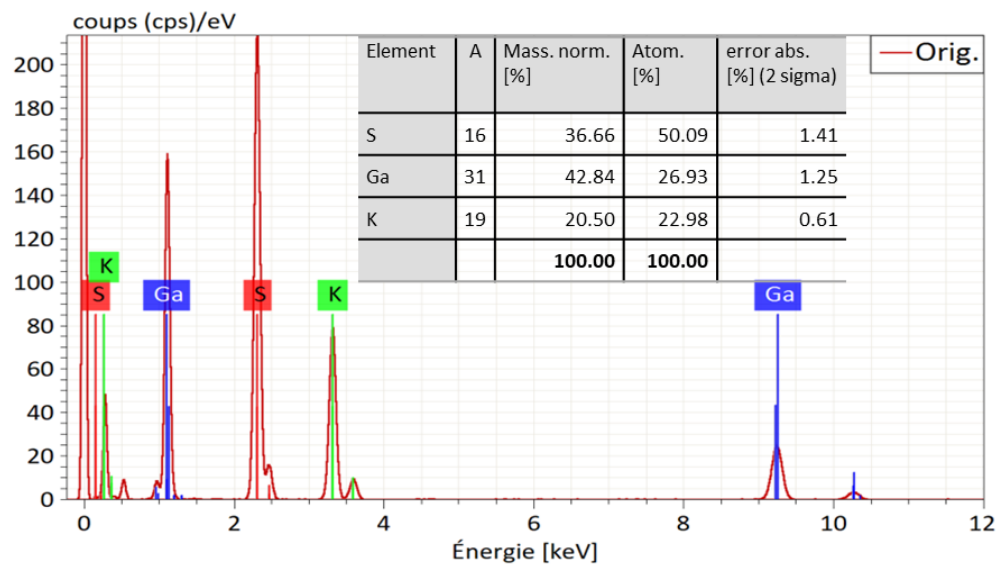


Fig. 6- EDS KGaS₂ and elemental quantitative data of the KGaS₂.

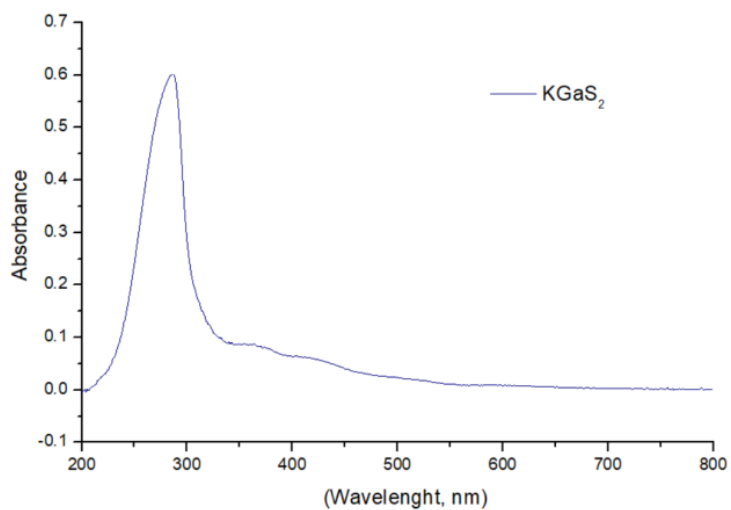


Fig. 7- UV-Vis absorption spectra of the EDA synthesized.

The physicochemical analysis of solvothermally synthesized K-thiogallate showed that it is structurally identical to the KGaS₂ obtained by solid-state high-temperature synthesis.

2.2. Synthesis optimization

The influence of the molar ratio of Ga/S/K on the crystallization results was studied. The products obtained with the molar ratio (Ga/S/K=1/5.7/2.3) showed the presence of some

amorphous parts. At the same time, the sulfur excess in the mixture (molar ratio Ga/S/K=1/25.5/2.3) led to a solid of higher crystallinity (**Fig.8**).

The crystallization time was varied from 1 to 7 days. After 1 day (**Fig. 9**), the product already contained a crystalline phase. The SEM inspection showed a mixture of crystallites 200-300 nm and 1-3 μm (**Fig. 10**). With further prolongation of the reaction time to 4 days, the nanosized crystals disappeared, and the particle size distribution became uniform. The changes in the crystal size were coupled with an increase in X-ray crystallinity.

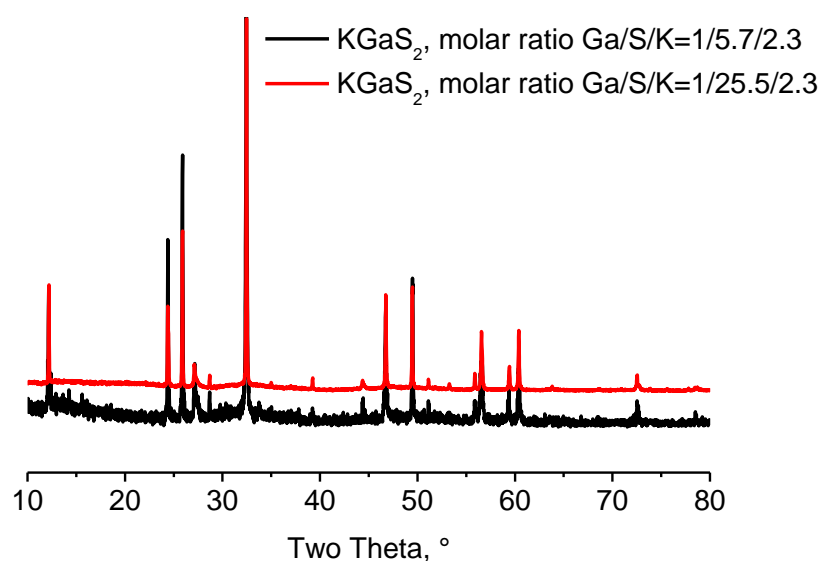


Fig.8- Powder XRD patterns of as-prepared KGaS₂ with two different Ga/S/K ratios (EDA, 7d, 190 °C).

Further extension of the synthesis time to 7 days did not result in changes in morphology and crystallinity.

The impact of ethanol and water on the formation of KGaS₂ was also studied. Ethanol or ethanol-water mixture was used as co-solvents of EDA, which led to a decrease in crystallinity (**Fig. 11** and **12**). The SEM images revealed a significant presence of small nanoparticles with random morphology that are most probably amorphous (**Fig.13**). The obtained patterns were similar to the simulated structure Shim et al. [23] (**Fig. 12**).

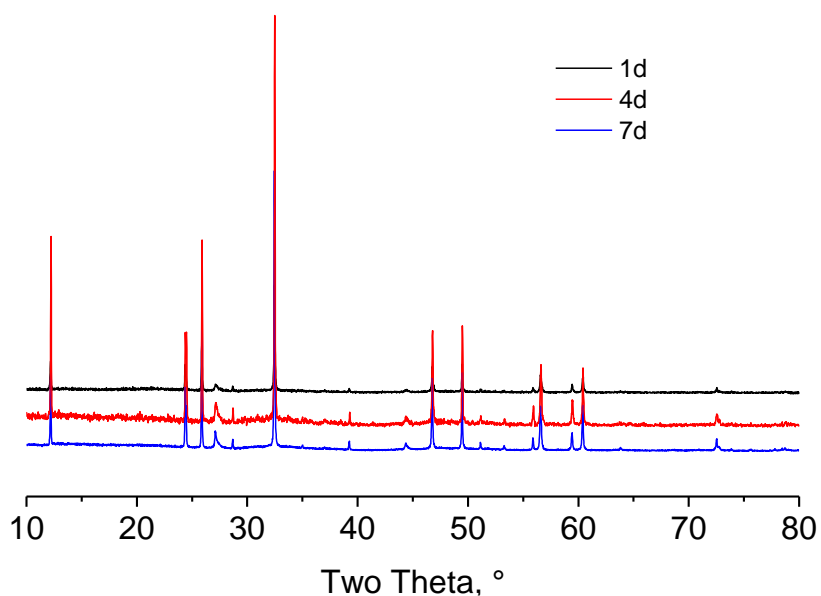


Fig. 9- PXRD patterns of as-prepared KGaS₂ with various crystallization time (1-7 days).

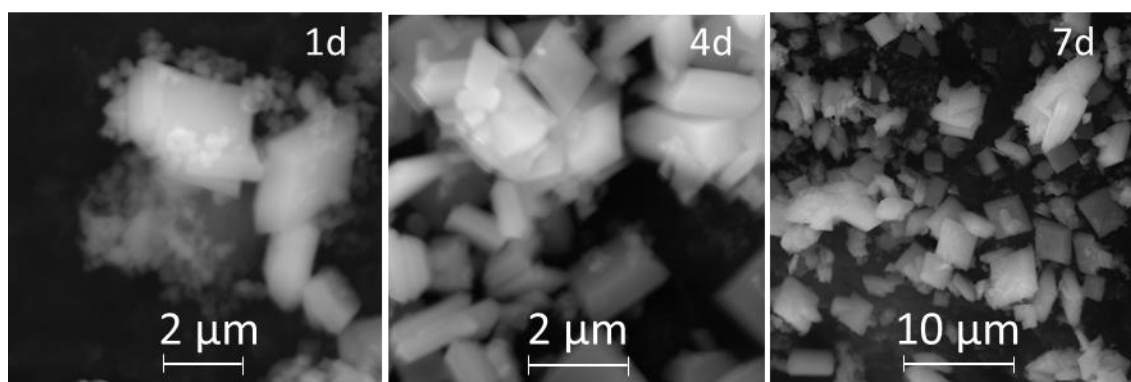


Fig. 10- SEM micrographs of KGaS₂ with ethylenediamine at 190 °C were prepared in the period of 1-7d.

2.3. Catalytic performances

2.3.1. KGaS₂ thermal stability

At 600 °C, the activity of thiogallate-based materials in CO₂ hydrogenation and ethane conversion is very limited, in the range of 1-2% of conversion. A noticeable increase in catalytic activity is observed with the temperature rise to 700 °C or higher. Thus, the ODH-CO₂ tests of ethane require elevated temperatures. In order to confirm the thermal stability of the novel material, KGaS₂, in that temperature range, the synthesized solid was subjected to 800 °C for 1 hour in N₂ flow, which was the highest temperature set point used in the catalytic experiments.

The XRD analysis confirmed the retention of crystallinity (**Fig. 14**) and that heating at 800 °C did not result in morphological changes (**Fig. 15**).

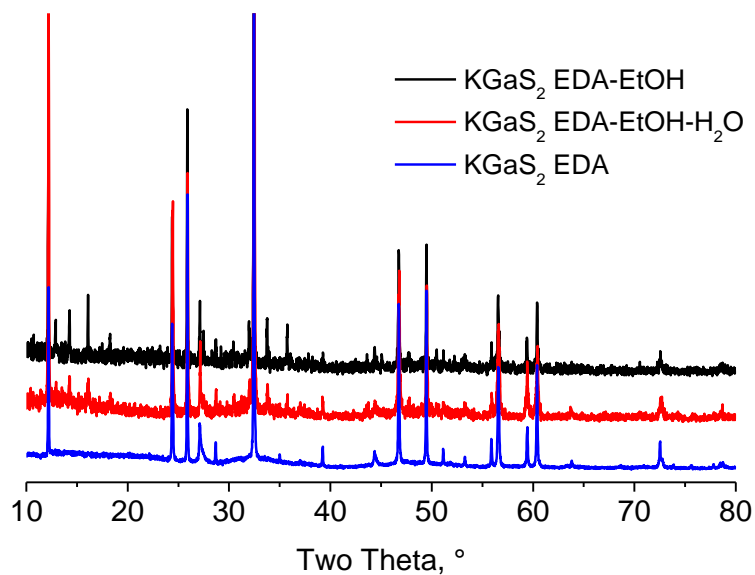


Fig. 11- PXR D patterns of KGaS₂ prepared with different solvents at 190°C for 7 days.

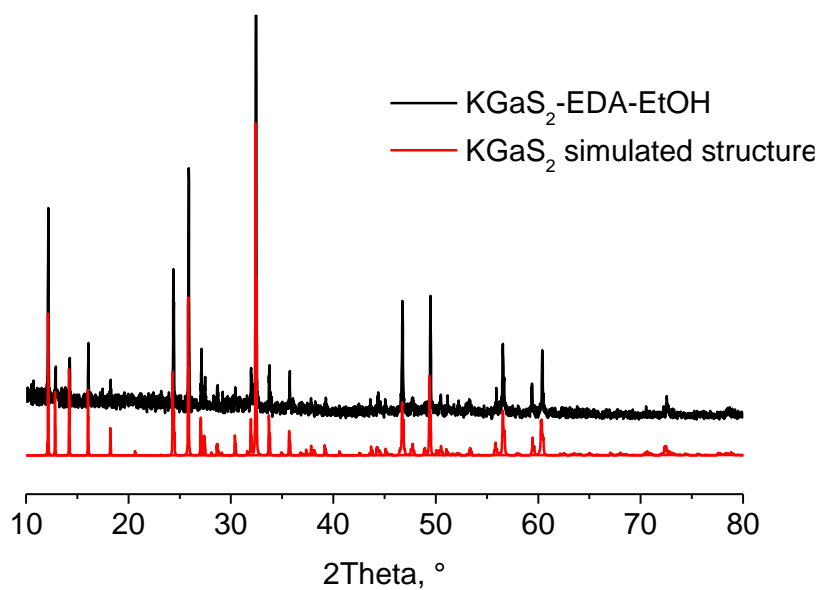


Fig. 12- PXR D patterns of as-prepared KGaS₂ with EDA-EtOH and simulated structure.

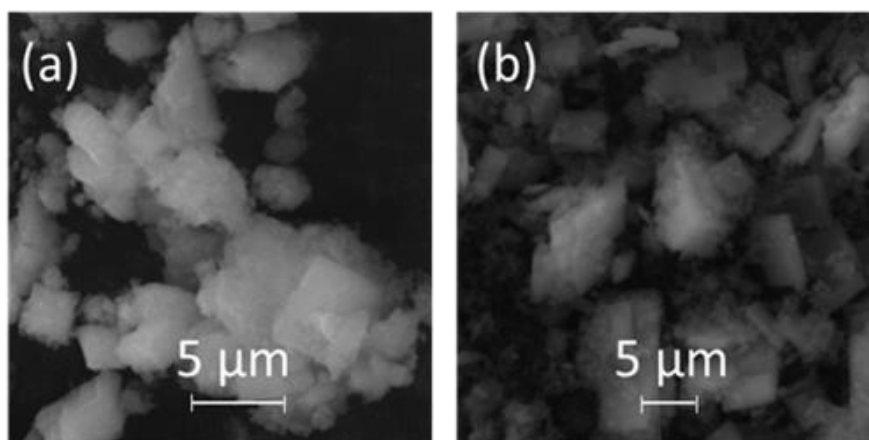


Fig.13- SEM micrographs of KGaS₂ prepared in (a) solvent system EDA-EtOH (2:1, volume ratio), and (b) EDA-EtOH-H₂O (2:1:1, volume ratio).

Blank test

In order to reveal the catalytic impact of the thiogallate-based materials on the reaction yield, a blank test without any catalyst was performed under the same operating conditions (same linear velocity, same temperature, same total and partial pressure of the reagents). In the blank test C₂ (ethane), N₂, and CO₂ were co-fed in the same ratio as in the catalytic reaction (C₂H₆/CO₂/N₂=49.5/36.5/14 v/v/v). The blank test without a catalyst is referred to in the text as a thermal process (“C₂ thermal”).

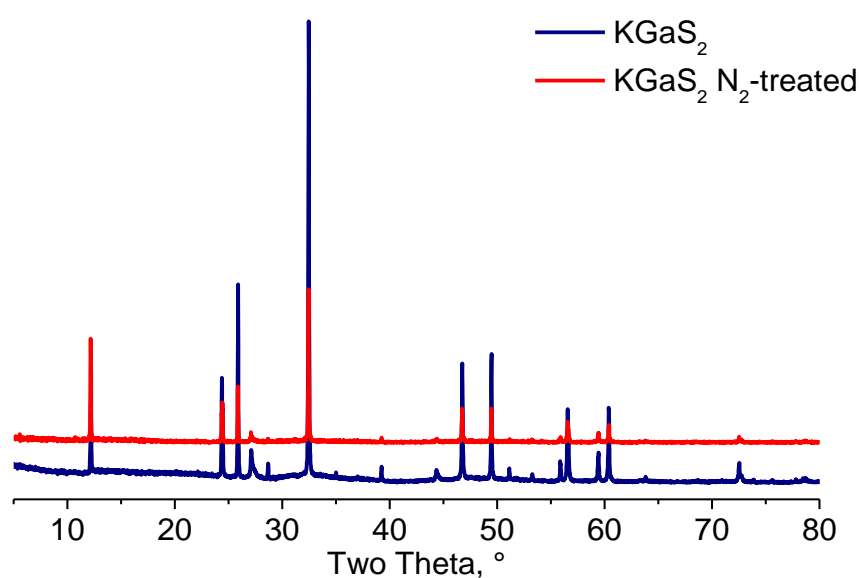


Fig. 14- PXRD patterns of KGaS₂ as-prepared and N₂-treated sample at 800 °C.

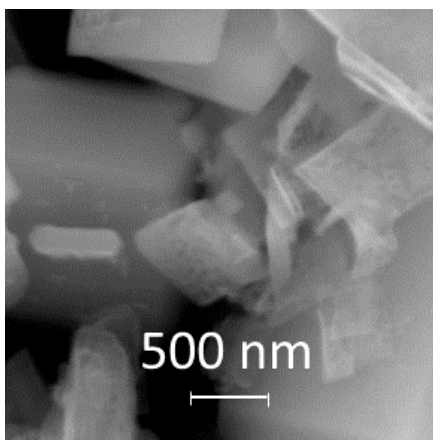


Fig. 15- SEM images of KGaS₂ N₂-treated at 800 °C.

2.3.2. Performance in ODH-CO₂ of ethane

The presence of the thiogallate-based material in the reactor showed substantial difference in performances already at 700 °C (the lowest reaction temperature); the conversions of CO₂ increased from 2% to 22% (**Fig. 16**). Interestingly, the ethane conversion on thiogallate even exceeded the thermal value at 700 °C (**Fig. 16**). So, the material not only showed a substantial hydrogenation activity for CO₂, but also were able to hydrogenate CO₂ without destroying ethylene yield from ethane. The activity of the catalyst was stable for the tested time-on-stream of 225 min (**Fig.17**).

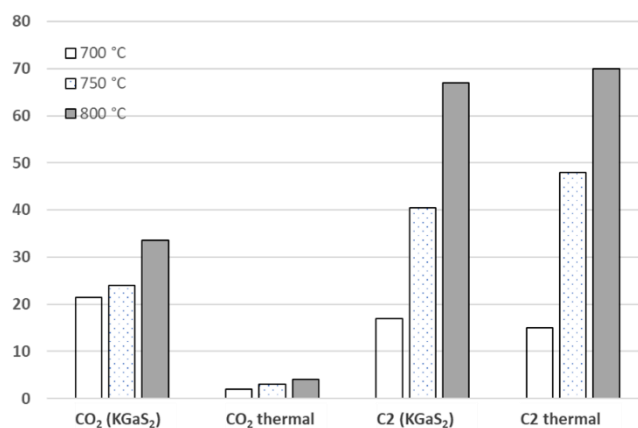


Fig.16- Comparison of C₂H₆ and CO₂ conversions on KGaS₂ -based catalysts with the thermal one (P = 1 atm, C₂H₆/CO₂ = 1/0.74, WHSV =5.9 h⁻¹).

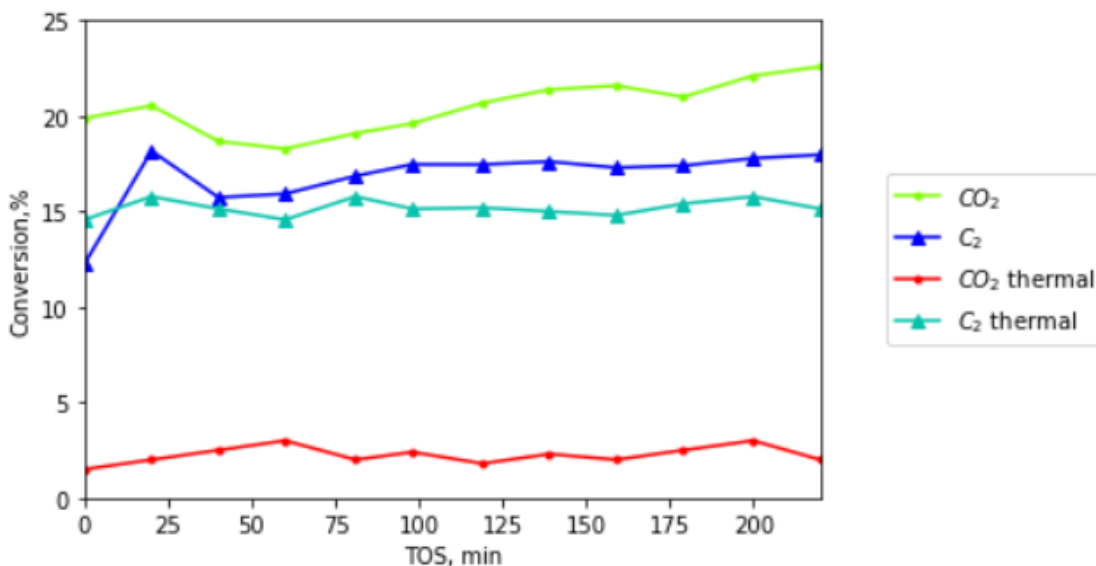


Fig. 17- C₂H₆ and CO₂ conversion on KGaS₂ based catalysts (P = 1 atm, C₂H₆/CO₂ = 1/0.74, WHSV = 5.9 h⁻¹, 700 °C).

However, upon further increase of the temperature to 750 °C, the thiogallate-based materials also started partially hydrogenate ethylene. The CO₂ conversion increased but the rise was relatively modest. Thus, due to the hydrogenation back of ethylene to ethane, the apparent ethane conversion decreased by 8% compared to the thermal one (**Fig. 16**).

Further temperature increases to 800 °C, resulted in a significant growth of both CO₂ and ethane conversions in the presence of the catalyst (**Fig. 16**). Although the catalyst still showed some ethylene hydrogenation, the difference with the thermal process decreased in comparison the one observed at 750 °C. In contrast, the CO₂ conversion reached the level of 36% at 800 °C, which was 12% higher relative to the one at 750 °C and roughly 13% lower than the thermodynamic equilibrium conversion (**Fig. 18**). The ethane conversion at 800 °C reached almost 70% what was relatively close to the thermodynamic value (**Fig. 18**).

Thus, the thiogallate-based material shows about 36% of CO₂ hydrogenation at 800 °C with only a minor impact on the ethylene yield and selectivity relatively to the thermal process (**Fig. 19**).

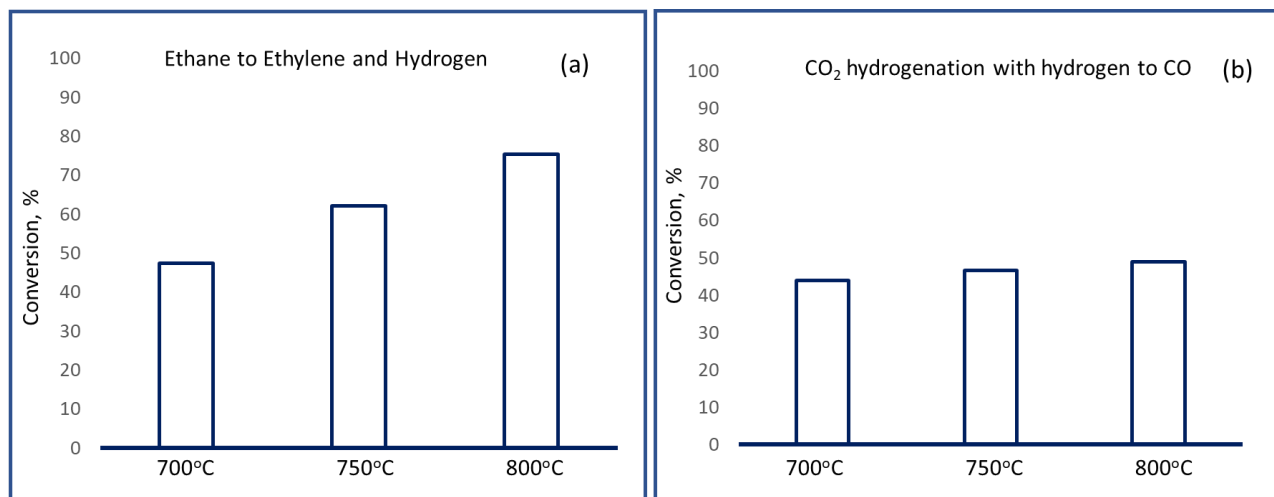


Fig. 18- Thermodynamic equilibrium conversions at different temperatures, assuming isothermal temperature profile for a) ethane conversion to ethylene and hydrogen at atmospheric pressure b) CO₂ hydrogenation with hydrogen (CO₂/H₂ -1) to CO at atmospheric pressure (calculated with AspenHysys v12).

One can also see that at 700 °C, the ODH-CO₂ of ethane on the thiogallate-based material results in the almost equivalent conversion of ethane and CO₂. That means that the produced hydrogen in ethane transformation to ethylene is fully utilized for CO₂ hydrogenating. Thus, the highest hydrogen utilization efficiency for CO₂ conversion was reached at 700 °C. (**Fig. 16**). In contrast, at 750 and 800 °C the conversion of CO₂ is roughly two times lower in comparison with the ethane conversion. This means that only half of the produced hydrogen was consumed for CO₂ hydrogenation.

One can see that the presented thiogallate-based materials have demonstrated a promising CO₂ hydrogenation activity that is comparable with the reported in literature for gallium oxide-based samples [10,37].

The selectivity to the by-products (to heavies) on the alkali thiogallate catalyst is slightly higher than in the transformation without catalyst. The absolute values vary with the increase of the temperature due to a change in the predominant transformation pathways of ethylene but the impact on selectivity remains minor (**Fig. 19**).

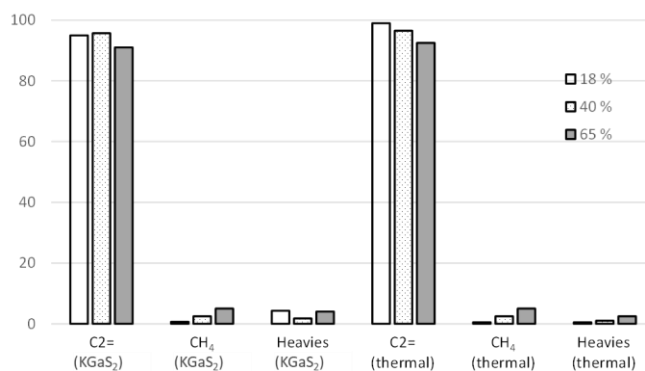


Fig.19- Comparison of carbon molar selectivities on coke-free basis at the same conversion level of ethane (18%, 40%, 65%) for the thermal and the catalytic (over KGS₂) routes (T =700-800 °C, P = 1 atm, C₂H₆/CO₂ = 1/0.74, WHSV =5.9 h⁻¹).

Logically, the rise of the temperature from 700 to 800 °C resulted in higher methane production with the selectivity increase from 1 to 7%. However, the selectivities to methane remained comparable between the catalytic and the thermal processes.

One can see that the experimentally observed conversion level of ethane at 700 °C and 750 °C in both catalytic and non-catalytic tests remain at about 50% relative to the thermodynamic equilibrium conversion (**Fig. 18**). The latter shows only a limited impact of the catalyst on the ethane activation in the studied temperature range. The value becomes much closer, almost reaching the thermodynamic level only at 800 °C.

In contrast, one can see that in the thermal non-catalytic process, the level of CO₂ conversion remains negligible, below 5% even at 800°C. This value is more than order of magnitude lower relative to the equilibrium level of conversion. However, the introduction of the catalyst in the reactor allows achieving significantly higher conversion of CO₂, as high as 36 % at 800 °C. This value is not that far from the thermolytic equilibrium conversion of CO₂ of about 49% at 800 °C (**Fig. 18**). So, the catalyst clearly contributes to CO₂ activation and in the utilization of the formed hydrogen from the thermal ethane transformation for CO₂ transformation to CO.

Interestingly, an estimation of the thermodynamic equilibrium in the system containing CO₂ and ethane, H₂, CO, H₂O, and ethylene showed that the preferred reaction should be the dry reforming of CO₂ with ethane to CO and hydrogen with only a very limited selectivity to ethylene

(**Fig. 20**). This reaction is undesirable for the ethylene synthesis from ethane and is not taking place without a specific catalyst. In contrast, the current KGaS₂ material preferentially catalyzes CO₂ hydrogenation in presence of ethylene with the hydrogen produced in-situ from the thermal conversion of ethane and substantially without making any significant production of heavy hydrocarbons and of methane.

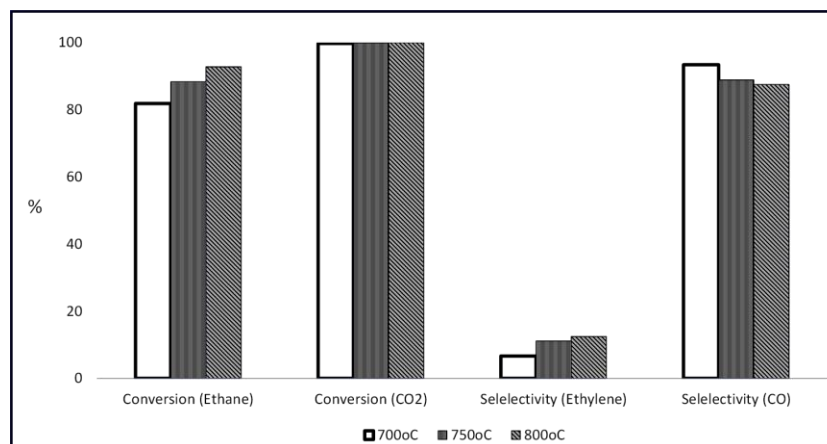


Fig. 20- Equilibrium product distribution at different temperatures, assuming isothermal temperature profile in the system (CO, CO₂, ethane, ethylene, hydrogen) containing initially the equal molar composition of CO₂ and ethane at atmospheric pressure (calculated with AspenHysys v12).

The analysis of the spent catalysts from ODH-CO₂ of ethane showed neither visible structure nor morphological changes (**Fig. 21**).

3. Conclusions

Crystalline alkali thiogallates were synthesized under solvothermal conditions, which represents a novel alternative route to obtain these materials. The physicochemical properties, including the thermal stability, of thiogallates were studied and revealed that they are sufficiently stable to be used as high-temperature heterogeneous catalysts. The KGaS₂-based material showed promising performance in CO₂-assisted oxidative ethane

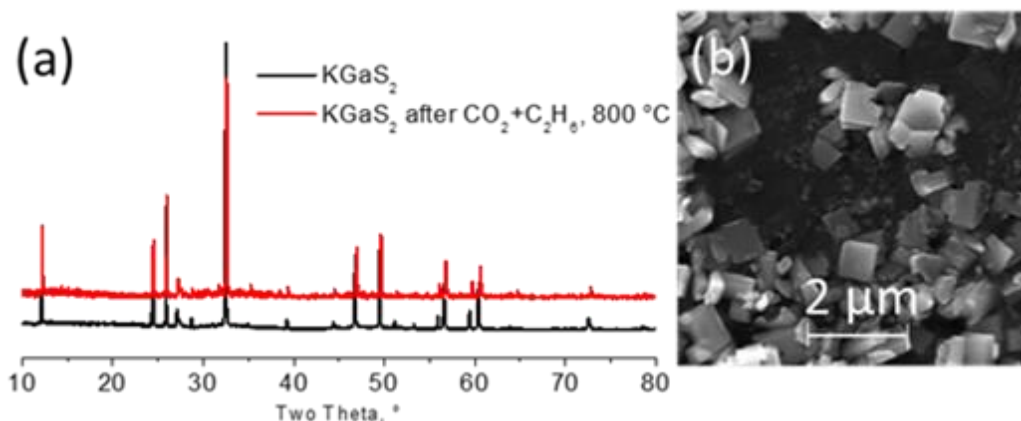


Fig.21- (a) PXRD patterns of as-prepared KGaS₂ and after ODH-CO₂ test (800 °C, P = 1 atm, C₂H₆/CO₂ = 1/0.74, WHSV =5.9 h⁻¹); (b) SEM images of KGaS₂ N₂-treated after ODH-CO₂ test (700 °C).

dehydrogenation process at 700-800 °C temperature range. The process showed close to thermodynamic conversion of ethane at 800 °C with a significant utilization of the produced hydrogen for CO₂ transformation to CO. The conversion of CO₂ to CO was at the level of 22-36%. The catalyst showed insignificant coke formation and allowed obtaining similar levels of the ethane conversion as for the thermal decomposition substantially without making any additional production of by-products (heavy hydrocarbons, CH₄). The set of experimental results proves that the thiogallate catalysts could be of interest for the processes where a moderate hydrogenation function is required in the presence of CO and highly reactive hydrocarbons.

References

- [1] Keith A. Couch, presented in part at the ME-TECH-2021, EPC MENA, virtual, February, 2021.
- [2] Br. Huovie, presented in part at the ME-TECH-2021, EPC MENA, virtual, February, 2021.
- [3] J. Hu, L. Yu, J. Deng, Y. Wang, K. Cheng, C. Ma, Q. Zhang, W. Wen, S. Yu, Y. Pan, J. Yang, H. Ma, F. Qi, Y. Wang, Y. Zheng, M. Chen, R. Huang, S. Zhang, Z. Zhao, J. Mao, X. Meng, Q. Ji, G. Hou, X. Han, X. Bao, Y. Wang and D. Deng, Sulfur vacancy-rich MoS₂ as a catalyst for the hydrogenation of CO₂ to methanol, *Nat. Catal.*, 2021, 4, 242–250.
- [4] A. Primo, J. He, B. Jurca, B. Cojocaru, C. Bucur, V. I. Parvulescu and H. Garcia, CO₂ methanation catalyzed by oriented MoS₂ nanoplatelets supported on few layers graphene, *Appl. Catal. B Environ.*, 2019, 245, 351–359.
- [5] F. Goodarzi, L. P. Hansen, S. Helveg, J. Mielby, T. T. M. Nguyen, F. Joensen and S. Kegnæs, The catalytic effects of sulfur in ethane dehydroaromatization, *Chem. Commun.*, 2020, 56, 5378–5381.
- [6] Z. Shen, J. Liu, H. Xu, Y. Yue, W. Hua and W. Shen, Dehydrogenation of ethane to ethylene over a highly efficient Ga₂O₃/HZSM-5 catalyst in the presence of CO₂, *Appl. Catal. Gen.*, 2009, 356, 148–153.
- [7] E. V. Lazareva, V. M. Bondareva, D. A. Svintsitskiy, A. V. Ishchenko, A. S. Marchuk, E. P. Kovalev and T. Yu. Kardash, Oxidative dehydrogenation of ethane over M1 MoVNbTeO catalysts modified by the addition of Nd, Mn, Ga or Ge, *Catal. Today*, 2021, 361, 50–56.
- [8] E. Gomez, B. Yan, S. Kattel and J. G. Chen, Carbon dioxide reduction in tandem with light-alkane dehydrogenation, *Nat. Rev. Chem.*, 2019, 3, 638–649.
- [9] Y. Cheng, H. Gong, C. Miao, W. Hua, Y. Yue and Z. Gao, Ga₂O₃/HSSZ-13 for dehydrogenation of ethane: Effect of pore geometry of support, *Catal. Commun.*, 2015, 71, 42–45.
- [10] R. Koirala, R. Buechel, F. Krumeich, S. E. Pratsinis and A. Baiker, Oxidative Dehydrogenation of Ethane with CO₂ over Flame-Made Ga-Loaded TiO₂, *ACS Catal.*, 2015, 5, 690–702.
- [11] S. P. Batchu, H.-L. Wang, W. Chen, W. Zheng, S. Caratzoulas, R. F. Lobo and D. G. Vlachos, Ethane Dehydrogenation on Single and Dual Centers of Ga-modified γ -Al₂O₃, *ACS Catal.*, 2021, 11, 1380–1391.
- [12] W. Chen, M. Cohen, K. Yu, H.-L. Wang, W. Zheng and D. G. Vlachos, Experimental data-driven reaction network identification and uncertainty quantification of CO₂-assisted ethane dehydrogenation over Ga₂O₃/Al₂O₃, *Chem. Eng. Sci.*, 2021, 237, 116534.
- [13] M. H. Jeong, K. S. Park, D. M. Shen, J. W. Moon and J. W. Bae, Dehydrogenation of ethane and subsequent activation of CO₂ on hierarchically-structured bimetallic FeM@ZSM-5 (M=Ce, Ga, and Sn), *Korean J. Chem. Eng.*, 2021, 38, 1129–1138.
- [14] V. V. Klepov, A. A. Berseneva, K. A. Pace, V. Kocevski, M. Sun, P. Qiu, H. Wang, F. Chen, T. M. Besmann and H. Løye, NaGaS₂: An Elusive Layered Compound with Dynamic Water Absorption and Wide-Ranging Ion-Exchange Properties, *Angew. Chem. Int. Ed.*, 2020, 59, 10836–10841.
- [15] D. Friedrich, M. Schlosser, R. Wehrich and A. Pfitzner, Polymorphism of CsGaS₂ – structural characterization of a new two-dimensional polymorph and study of the phase-transition kinetics, *Inorg. Chem. Front.*, 2017, 4, 393–400.

- [16] J. Zhang, S. Zhu, B. Zhao, B. Chen and Z. He, A new method of synthesis on high-quality AgGaS₂ polycrystalline, *Curr. Appl. Phys.*, 2010, 10, 544–547.
- [17] J. Hu, Q. Lu, K. Tang, Y. Qian, J. Hu, Q. Lu, K. Tang, Y. Qian, G. Zhou and X. Liu, Solvothermal reaction route to nanocrystalline semiconductors AgMS₂ (M=Ga, In), *Chem. Commun.*, 1999, 1093–1094.
- [18] H. Wu, X. Li, Y. Cheng, Y. Xiao, Q. Wu, H. Lin, J. Xu and Y. Wang, The synergistic role of double vacancies within AgGaS₂ nanocrystals in carrier separation and transfer for efficient photocatalytic hydrogen evolution, *Catal. Sci. Technol.*, 2019, 9, 5838–5844.
- [19] B. Eisenmann and A. Hofmann, Crystal structure of hexasodium di- μ -thiobis(dithiogallate) – II, Na₆Ga₂S₆, *Z. Für Krist. - Cryst. Mater.*, 1991, 197, 143–144.
- [20] S. Balijapelly, P. Sandineni, A. Adhikary, N. N. Gerasimchuk, A. V. Chernatynskiy and A. Choudhury, Ternary alkali ion thiogallates, A₅GaS₄ (A = Li and Na), with isolated tetrahedral building units and their ionic conductivities, *Dalton Trans.*, 2021, 50, 7372–7379.
- [21] Y. Yuan, J. Zai, Y. Su and X. Qian, Controlled synthesis of monodispersed AgGaS₂ 3D nanoflowers and the shape evolution from nanoflowers to colloids, *J. Solid State Chem.*, 2011, 184, 1227–1235.
- [22] Q. Lu, J. Hu, K. Tang, Y. Qian, G. Zhou and X. Liu, Synthesis of Nanocrystalline CuMS₂ (M = In or Ga) through a Solvothermal Process, *Inorg. Chem.*, 2000, 39, 1606–1607.
- [23] S. Shim, W. B. Park, M. Kim, J. Lee, S. P. Singh and K.-S. Sohn, Cyan-Light-Emitting Chalcogenometallate Phosphor, KGaS₂:Eu²⁺, for Phosphor-Converted White Light-Emitting Diodes, *Inorg. Chem.*, 2021, 60, 6047–6056.
- [24] D. Friedrich, M. Schlosser, M. Etter and A. Pfitzner, Influence of Alkali Metal Substitution on the Phase Transition Behavior of CsGaQ₂ (Q = S, Se), *Crystals*, 2017, 7, 379.
- [25] D. Friedrich, F. Pielhofer, M. Schlosser, R. Weihrich and A. Pfitzner, Synthesis, Structural Characterization, and Physical Properties of Cs₂Ga₂S₅, and Redetermination of the Crystal Structure of Cs₂S₆, *Chem. - Eur. J.*, 2015, 21, 1811–1817.
- [26] J. S. Jang, S. H. Choi, N. Shin, C. Yu and J. S. Lee, *J. Solid State Chem.*, 2007, 180, 1110–1118.
- [27] K. Yamato, A. Iwase and A. Kudo, AgGaS₂-type photocatalysts for hydrogen production under visible light: Effects of post-synthetic H₂S treatment, *ChemSusChem*, 2015, 8, 2902–2906.
- [28] S. H. Choi, J. S. Jang, N. Shin and J. S. Lee, Characterization of AgGaS₂-type Photocatalysts for Hydrogen Production from Water Under Visible Light, in *AIP Conference Proceedings*, AIP, Stanford, California (USA), 2007, 882, 628–630.
- [29] Z. Zhao, F. Qin, S. Kasiraju, L. Xie, Md K. Alam, S. Chen, D. Wang, Z. Ren, Z. Wang, L. C. Grabow and J. Bao, Vertically Aligned MoS₂/Mo₂C hybrid Nanosheets Grown on Carbon Paper for Efficient Electrocatalytic Hydrogen Evolution, *ACS Catal.*, 2017, 7, 7312–7318.
- [30] Y. Luo, L. Tang, U. Khan, Q. Yu, H.-M. Cheng, X. Zou and B. Liu, Morphology and surface chemistry engineering toward pH-universal catalysts for hydrogen evolution at high current density, *Nat. Commun.*, 2019, 10, 269.
- [31] J. Rumble and P. Vaqueiro, Na₅(Ga₄S)(Ga₄S)₃·6H₂O: A three-dimensional thiogallate containing a novel octahedral building block, *Solid State Sci.*, 2011, 13, 1137–1142.
- [32] P. Vaqueiro, From One-Dimensional Chains to Three-Dimensional Networks: Solvothermal Synthesis of Thiogallates in Ethylenediamine, *Inorg. Chem.*, 2006, 45, 4150–4156.

- [33] G. E. Delgado, A. J. Mora, F. V. Pérez and J. González, Growth and crystal structure of the layered compound TlGaSe₂, *Cryst. Res. Technol.*, 2007, 42, 663–666.
- [34] P. Lemoine, D. Carré and M. Guittard, Structure du sulfure de gallium et de potassium, KGaS₂, *Acta Crystallogr. C*, 1984, 40, 910–912.
- [35] V. Petříček, M. Dušek and L. Palatinus, Crystallographic Computing System JANA2006: General features, *Z. Für Krist. - Cryst. Mater.*, 2014, 229, 345–352.
- [36] S. Paderick, M. Kessler, T. J. Hurlburt and S. M. Hughes, Synthesis and characterization of AgGaS₂ nanoparticles: a study of growth and fluorescence, *Chem. Commun.*, 2017, 54, 62–65.
- [37] B. Zhao, Y. Pan and C. Liu, The promotion effect of CeO₂ on CO₂ adsorption and hydrogenation over Ga₂O₃, *Catal. Today*, 2012, 194, 60–64.

Chapter 7. Conclusions and prospects

1. Conclusions

This research was focused on the catalyst design for ethane conversion with CO₂ presence as an alternative to ethane steam cracking. The fundamental characteristics of the catalysts that provide hydrogenation and dehydrogenation properties and stability under harsh conditions were studied.

The developed catalytic systems can be divided into two categories: sulfide-derived carbide-like Mo (EZ_{Si}-(x%Mo₂C)_S) and Co-Mo (EZ_{Si}-(x%Mo₂C-y%Co_xC)_S) embryonic zeolite supported catalysts and potassium thiogallate (KGaS₂). Both catalytic systems demonstrated promising catalytic properties under harsh conditions. Despite ethane excess, ethylene selectivity was comparable to or higher than the steam ethane cracking.

In general, the thiogallate catalyst showed promising results at lower temperatures, while the carbide catalysts performed better at higher temperatures, especially for CO₂ hydrogenation.

The most important results can be summarized as follows:

Chapter 4: The supported Mo sulfide-derived catalyst displays moderate activity in ODH-CO₂. Changes in the active phase composition were observed. The alteration of the catalyst is a consequence of the interaction of ethane with MoS₂ leading to the formation of a carbide. Thus, the MoS₂ was successfully employed as a carbide precursor. Sulfide-derived carbides hydrogenate CO₂ without negatively impacting the thermal C₂ conversion to ethylene, as the yield was 66%, while the ethane converts to ethylene with 98-89% selectivity in the temperature range 700-800 °C. Concerning all total C-products selectivity, the CO selectivity was 28-39%, and the ethylene selectivity was 70.5-55%.

Chapter 5: This part of the study deals with catalyst deactivation and CO₂ conversion intensification. The deactivation mechanism was revealed. It was found that the interaction of the active phase with carbon dioxide led to the formation of bulkier particles of MoO₂. The catalyst deactivation led to a noticeable decrease in CO₂ conversion, as MoO₂ species are inactive in hydrogenation. The control of catalytic behavior was achieved by oxidic precursors optimization. Besides the impact synthesis mode, the catalyst's activation, and oxidation resistance were studied. It was found that the hydrothermal synthesis for precursor, the increase

in the wt.% of the active phase, and slower activation resulted in a more stable catalyst with enhanced activity. However, the conversion was limited to 45% CO₂ at 750 °C.

Further, a new system, i.e., a bimetallic Co-Mo catalyst was explored. The Co doping showed a direct positive impact on the CO₂ conversion, which raised two times at 700 °C compared to EZ_{Si}-(5%Mo₂C)₅. Also, the Co doping changed the mechanism of the CO₂ interaction with ethane. Thus, the Co-Mo catalysts were found to be suitable for dry ethane reforming. Subsequently, catalyst's working conditions were optimized for each process. Under dry reforming conditions, CO₂ conversion could reach 70-80% at 700-750 °C. Thus, the Co doping resulted in higher conversions and catalyst stability under both ODH-CO₂ and DRE-routes. Noteworthy, the formation of the oxide phase on the catalyst surface has noticeably decreased.

Chapter 6: The KGaS₂ thiogallate was synthesized according to a new method and for the first time tested in a high-temperature catalytic process. To boost the catalytic activity the KGaS₂ crystallites size was decreased to 1-3 μm. Thiogallates were sufficiently stable under CO₂ and C₂H₆ flows at 700-800 °C. The conversion of CO₂ to CO was at the level of 22-36%, while the ethane conversion ranged between 18 and 65%. This type of catalyst demonstrated promising performance in the ODH-CO₂ process.

2. Prospects

This work opens new perspectives for ODH-CO₂ catalysts. The application of sulfidic precursors as for Mo or Mo-Co carbide catalysts may result in a new type of catalyst for dry methane reforming, super dry methane reforming, and dry ethane reforming.

Research related to the EZ-(x%Mo₂C)₅ catalysts opens up a new field of application for metal-modified embryonic zeolites. The findings of the alkanes nature and the conversion of sulfide to carbide are also extremely little explored and open new opportunities for tuning catalyst properties.

The development of the Co-Mo catalytic system provides high flexibility in the process. It could result in a new concept where only by adjusting the feed rate a C₂H₄-rich gas or a CO-rich product can be obtained.

The pioneering research on thiogallates for ODH-CO₂ offers promises for a new catalyst branch for oxidative processes with CO₂. Also, the applied synthetic approach could be interesting for the nanothiogallates design.

Summing up, this study can be useful for both, developing sulfide and carbide catalytic systems and in synthesizing materials with new properties.

Scientific production

Posters

V. Bikbaeva, N. Nesterenko, Jean-Pierre Gilson, V. Valtchev (Vogüé, France), Catalyst design for ethane oxidative dehydrogenation in presence of CO₂. Poster session presented at a *37^{ème Réunion Annuelle du Groupe Français des Zéolithes}*, March 2022.

V. Bikbaeva, N. Nesterenko, Jean-Pierre Gilson, V. Valtchev (Cabourg, France), Catalyst design for ethane oxidative dehydrogenation in presence of CO₂. Poster session presented at *8th Workshop – Zeolites*, June 2022.

Ethane oxidative dehydrogenation in the presence of CO₂ over molybdenum carbide catalyst grafted on embryonic zeolites. Poster session presented at *20th International Zeolite Conference, IZC-2022*, July 2022 (Valencia, Spain).

Publications related to this work

1. V. Bikbaeva, O. Perez, N. Nesterenko, V. Valtchev, Ethane oxidative dehydrogenation with CO₂ on thiogallates, **Inorg. Chem. Front.** (2022). <https://doi.org/10.1039/D2QI01630C>.
2. V. Bikbaeva, N. Nesterenko, S. Konnov, T.-S. Nguyen, J.-P. Gilson, V. Valtchev, A low carbon route to ethylene: Ethane oxidative dehydrogenation with CO₂ on embryonic zeolite supported Mo-carbide catalyst, **Applied Catalysis B: Environmental** 320 (2023) 122011. <https://doi.org/10.1016/j.apcatb.2022.122011>.

Acknowledgments

This section is dedicated to all people who in one or another way have been part of this long journey. I was happy to find so welcoming and friendly collective. I enjoy work in Laboratoire Catalyse et Spectrochimie (LCS). These 3 years were unique and important experience for me: new country, new research, new slice of life. It was challenging and engrossing.

First of all, I would like to thank Pr. Valentin Valtchev and Dr. Nikolay Nesterenko. They have given me a great opportunity to do Ph.D. project in LCS. This project and wise supervision made me more professional and high-skilled. I am very grateful for this chance to work with you!

I would like to thank the members of the jury for agreeing to be participants of this moment.

Thanks to the Industrial Chair ANR-TOTAL “NanoClean Energy” (ANR-17-CHIN-0005-01), and project NanoCleanEnergy⁺ (Region Normandy) for funding.

Also, a lot of thanks all LCS members 2019-2022. Your support, presence, friendship does these three years great. Dear LCS team: Louwanda Lakiss, Valerie Ruaux, Marie Desmurs-Lozier, Benjamin Foucault, Pascal Roland, Jaafar El Fallah, Alexandre Vimont, Philippe Bazin thank you for training and all help with analysis, equipment. Thank you to all the administrative staff: Sophie Greard, Blandine Rabelle, and Robenson Saint-Louis, for your administrative support.

I want to thank Dr. Olivier Perez for his contribution to the crystallography study of thiogallates.

I would like to thank all LCS students, postdocs whom I met here. I would like to say special thanks to people in LCS and ENSICAEN, whom help me with their knowledge, support and friendship Aigerim Baimyrza, Ana Palčić, Florent Dubray, Ahmed Omran, Haonuan Zhao, Luz Zavala Sanchez, Luis Aguilera, Edwin Clatworthy, Hugo Cruchade, Aymeric Magisson, Sajjad Ghojavand, Mariame-Juliette Akouche. Thanks two best ladies (Vika and Julia) for moral support!

And finally, but not less extent, I would like to tell a million thanks to my mother Pr. Nellya Grigor’eva for her support and unconditional love during these three years and throughout our lives. I must say that her example did not discourage me from at least linking my life with science.

Metal-sulfide materials for ethane conversion in presence of CO₂

Ethane processing is a large industrial branch for high-valuable chemicals production. Steam cracking of oil fractions is the major process currently used to produce ethylene. An alternative ethane conversion strategy is the oxidative dehydrogenation of ethane with CO₂. Thus, the present study is devoted to oxidative ethane dehydrogenation (ODH-CO₂) and ethane dry reforming (DRE). The ethane conversion with CO₂ is performed on the principally new types of catalysts - metal sulfides (KGaS₂) and metal sulfide-derived carbides, the latter being grafted on embryonic zeolites. Carbides are found to be flexible catalytic systems with tunable properties for ODH-CO₂ and DRE. The set of experimental data proves a carbon-negative process with ethylene selectivity (89-98%) and reactants conversion comparable with steam cracking parameters. The PhD thesis also reports the first application of thiogallates for thermal catalysis. The obtained results open new perspectives for thiogallates application as hydrogenation catalysts (ethylene selectivity 87-96%).

Key words: embryonic zeolite, ODH-CO₂, catalysis, CO₂ utilization, ethylene production, sulfide catalysis, carbide catalysis.

Matériaux métal-sulfure pour la conversion de l'éthane en présence de CO₂

Le traitement de l'éthane est une grande branche industrielle pour la production de produits chimiques de grande valeur. Le vapocraquage des fractions pétrolières est le principal procédé actuellement utilisé pour produire de l'éthylène. Une autre stratégie de conversion de l'éthane est la déshydrogénation oxydative de l'éthane avec du CO₂. Ainsi, la présente étude est consacrée à la déshydrogénation oxydative de l'éthane (ODH-CO₂) et au reformage à sec de l'éthane (DRE). La conversion de l'éthane avec le CO₂ est effectuée sur les principaux types de catalyseurs nouveaux - les sulfures métalliques (KGaS₂) et les carbures dérivés de sulfures métalliques, ces derniers étant greffés sur des zéolithes embryonnaires. Les carbures se révèlent être des systèmes catalytiques flexibles avec des propriétés accordables pour ODH-CO₂ et DRE. L'ensemble des données expérimentales prouve un procédé carbone négatif avec une sélectivité en éthylène (89-98%) et une conversion des réactifs comparables aux paramètres de vapocraquage. La thèse de doctorat rapporte également la première application des thiogallates pour la catalyse thermique. Les résultats obtenus ouvrent de nouvelles perspectives pour l'application des thiogallates comme catalyseurs d'hydrogénation (sélectivité éthylène 87-96%).

Mots clés: zéolithe embryonnaire, ODH-CO₂, catalyse, utilisation du CO₂, production d'éthylène, catalyse sulfure, catalyse carbure.